TECHNO-ECONOMIC ANLYSIS OF SMART GRID BASED RENEWABLE COMMITMENT OF DEMAND RESPONSE

A Thesis Submitted in Partial Fulfilment of the Requirements for the Award of the Degree of

DOCTOR OF PHILOSOPHY

Submitted by

Aniruddha B Bhattacharya
(Enrolment No.2K12/PHDEE/06)

Under the Supervision of

Prof Madhusudan Singh, EED, DTU

DEPARTMENT OF ELECTRICAL ENGINEERING
DELHI TECHNOLOGICAL UNIVERSITY
(Formerly Delhi College of Engineering)
Shahabad Daulatpur, Main Bawana Road Delhi: 110042 India

December, 2023

DECLARATION

I hereby certify that the work presented in this thesis entitled **"TECHNO-ECONOMIC ANLYSIS OF SMART GRID BASED RENEWABLE COMMITMENTOF DEMAND RESPONSE"** which is submitted in partial fulfilment of the requirements for the award of the degree of Doctor of Philosophy in the Department of Electrical Engineering Delhi Technological University Delhi is authenticate record of my own work carried out under the supervision of Prof Madhusudan Singh. The matter presented in this thesis has not been submitted elsewhere for the award of a degree

Aniruddha B Bhattacharya
2K12/PHDEE/06

Place: Delhi
Date: 12/11/2023

CERTIFICATE

Based on the candidates declaration , I hereby certify that the work which is presented in this thesis entitled “TECHNO-ECONOMIC ANLYSIS OF SMART GRID BASED RENEWABLE COMMITMENT OF DEMAND RESPONSE” submitted to the Department of Electrical Engineering Delhi Technological University Delhi in partial fulfilment of the requirement for the award of the degree of Doctor of Philosophy , is an original contribution with the existing knowledge and faithful record of the research work carried out by him under our guidance and supervision. To the best of my knowledge this work has not been submitted in part or full for the award of any degree elsewhere

Prof. Madhusudan Singh
Department of Electrical Engineering
DTU Delhi

The PhD Viva Voce of Mr**. Aniruddha B Bhattacharya** research scholar has been held on _____

Signature of

Supervisors

Signature of

Head, Dept. of Electrical Engg.

Acknowledgements

I would like to express my thanks to my advisor and friend **Professor Madhusudan Singh**. Thank you for encouraging my research and helping me to grow as a professional and human being.

Special thanks to **Professor Suman Bhowmick** who mentored me at the beginning of this journey and **Professor R S Saha** who always helped supporting this endeavour.

Additionally, thanks to my committee members, **Professor Dr. Alka Singh, Professor Dr. Rachna Garg,** for serving as my committee and for reviewing my work.

Special thanks and Professor Dr. Pedro Vásquez at Department of Ecology and Environment Utrecht University Netherlands, for reviewing my work.

I would like to thank all my friends and professors, without whom nothing of this would be possible finally; I would like to express my gratitude to my mother Smt Namita Bhattacharya who became a motivation during good or bad moments.

ABSTRACT

The authors of this study developed a LQR-ORT-based power sharing control scheme for three-phase inverter-based generators that use LCL filters in either grid-connected or islanding modes. While responding to transients, a LQR-ORT controller improved resilience margins and decreased control input and power error quadratic values. In order to prevent frequency and voltage fluctuations in the AC bus that do not have communications, additional loops were also used. Future system (effective) inertia, particularly during low demand conditions, might be significantly reduced with an increase in the penetration of non-synchronous generators, like as wind.

In addition, the grid frequency and its rate-of-change (RoCoF) are likely to experience unacceptable big changes due to the probability of higher and more frequent in-feed losses. To prevent RoCoF-based mains protection relays from firing, which might cause cascading outages and compromise system security, it is vital to restrict RoCoF within acceptable levels. In such cases, a quick reaction from loads could be vital for the system's safe functioning. Furthermore, in order to accomplish proportionate power sharing among generators based on their rated power capacity, additional loops were used. Additionally, a synchronous reference frame model was created, which included power sharing dynamics and voltage-current (V-I) control loops.

The model's stability and resilience to alterations in the LCL filter components were proved by the study of the LQR-ORT controller. By using the flexibility of certain kinds of loads, it is possible to adjust the supply voltage and frequency using either current power electronic interfaces (such as motor drives) or new ones, such as the newly proposed "Electric Spring" (ES), which might result in a quick and controllable power reserve. The usefulness of these controlled loads in contributing to inertial and/or primary frequency control as a demand response metric is shown in this thesis, which also explores the availability of quick short-term power reserve from them.

A physical experiment was used to implement the suggested controller in both grid-connected and island modes.

A microgrid tested equipped with four inverter-based generators and MATLAB-based OPAL-ART real-time simulators were created for the purpose of conducting this experiment. Current findings show that the suggested model is accurate and that the LQR-ORT based demand response controller improves the islanded micro grid's transient response, power sharing, voltage and frequency recovery, and overall effectiveness.

Table of Contents

List of Tables

List of Figures

List of Abbreviations and Acronyms

ARE	Algebraic Ricatti Equation
DOE	Department of Energy
DARE	Discrete Algebraic Ricatti Equation
DG	Distributed Generators
ECU	Energy Conversion Unit
ESU	Energy Storage Unit
HIL	Hardware-in-the-loop
LFT	Linear Fractional Transformation
LMI	Linear Matrix Inequality
LQG	Linear Quadratic Gaussian
LQR	Linear-Quadratic Regulator
MIMO	Multiple Input Multiple Output
NRMSE	Normalized Root Mean Squared Error
ORT	Optimal Reference Tracking
PSO	Particle Swarm Optimization
PI	Proportional-Integral
PID	Proportional-Integral-Derivative
PLL	Phase-Locked Loop
PR	Proportional-Resonant
RES	Renewable Energy Sources
SOGI	Second-order Generalized Integrator
THD	Total Harmonic Distortion
UPS	Uninterruptible Power Supply
V-I	Voltage-Current

Chapter 1

Introduction

Problems with sustainability, dependability, and market share are plaguing traditional energy sources including hydropower, gas, coal, and petroleum. the usage of energy from renewable sources is quickly becoming a viable option for meeting these demands. As seen in Figure 1.1, RES is usually linked to a load along with the main grid via an ECU (Energy Conversion Unit) and an ESU (Energy-Storage Unit). After the load consumes all of the produced energy, the ESU (Excess Storage Unit) is used for storing the remaining amount. Because of the intermittent nature of RES (Renewable Energy Sources) like solar & wind, an ESU is utilized to augment the energy supply. The ECU's job is to convert the input voltage, which may be either AC or DC, into an appropriate voltage level that corresponds to the load's AC or DC characteristics. To supplement the produced electricity or even inject power into the grid, the ECU may also be linked to the main grid.

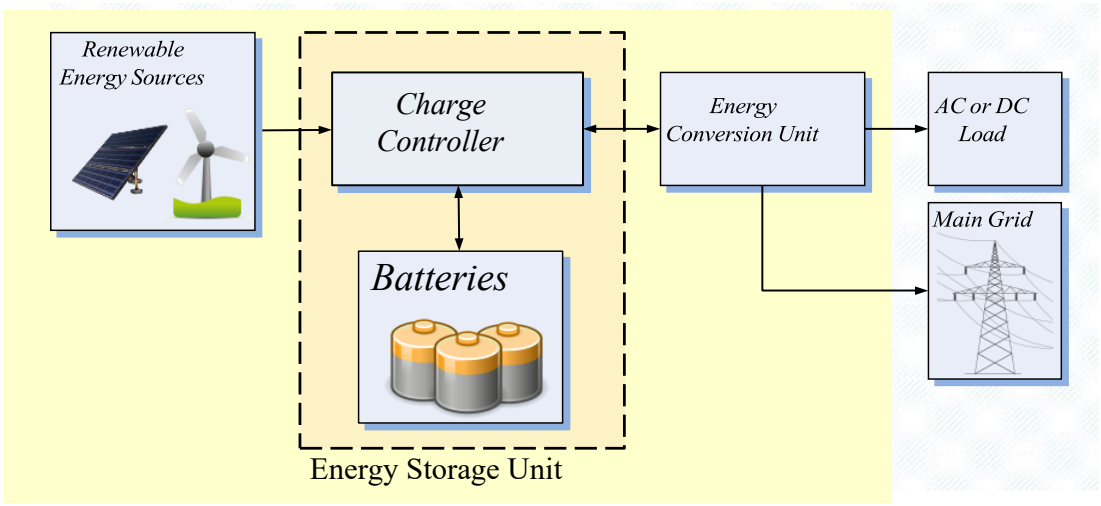

Fig. 1.1. Typical Structure of a RES Generator

As a method for systematically integrating RES in neighborhood or business clusters, microgrids have recently emerged worldwide, 2,134 microgrid projects with a combined capacity of 24.981 GW are now operational [1]. A growing number of companies are expanding their offerings in the field of microgrid technologies, allowing users to model electrical systems in real-time using modules provided by companies like DSPACE systems[4], national measurements labview[3],

and opal RT technologies [2]. Power electronics, control theory, and distribution system advancements recently,

Microgrids are an appropriate decentralized method for power generation due to government rules and regulations. However, engineers face a plethora of issues with microgrid penetration, formalization, and implementation because of RES's changeable nature. Problems with power quality, stability and robustness in control, and a lack of standardization regulations are only a few of the obstacles. Among these obstacles, control problems stand out as a major roadblock to wider use and standardization of microgrids. Stability, efficiency, and efficiency are three technical aspects of microgrids that may be improved with the help of control theory. In order to combine v-i and main control level for 3-phase inverter-based microgrids, this study introduces an optimum LQ control approach with optimal reference tracking(LQR-ORT). Here is the structure of the document: microgrids are introduced in chapter 1 along with their primary features and difficulties. The chapter also lays out the research's issue statement and primary aims. Recent publications on micro shared power and v-i control are reviewed in chapter 2. Chapter 3 presents the technique that has been suggested. In chapter 4, the findings and analyses are detailed. Lastly, chapter 5 presents the final observations and implications.

1.1 General

Microgrids are an appropriate decentralized method for power generation due to government rules and regulations. However, engineers face a plethora of issues with microgrid penetration, formalization, and implementation because of RES's changeable nature. Problems with power quality, stability and robustness in control, and a lack of standardization regulations are only a few of the obstacles. Among these obstacles, control problems stand out as a major roadblock to wider use and standardization of microgrids. Stability, efficiency, and efficiency are three technical aspects of microgrids that may be improved with the help of control theory.

Microgrids are gaining popularity as a result of the growing usage of renewable energy sources to generate electricity. A microgrid is ‘a collection of interdependent loads that distribute power sources within clearly established electrical boundaries that operate as one controllable unit when compared to the grid,’ as per us DOE (department of energy). Operating in either grid-connected or island-mode is possible for a microgrid because of its ability to connect and disengage from the grid [5]. In a nutshell, this idea depicts the key features of a microgrid. It goes on to detail the majority of the technical obstacles to microgrid integration. To begin, a

microgrid can't function without linked, dispersed generators. Secondly, a microgrid needs to function as an independent unit. This necessitates perfect synchronization between all generators to provide both active and reactive power. In accordance with the needs of the microgrid and its operating mode. Lastly, a microgrid may function either in line with the main grid or independently of it. This means that the voltage of the reference, frequency, and phase must be ensured regardless of the presence or absence of a main network with high inertia.

A standard microgrid's framework is detailed in the section that follows. Additionally, every level of control in a microgrid is defined, and the idea of microgrid control structures is established. We conclude by outlining the key benefits and obstacles of microgrid control.

1.1.1 General Structure of a Microgrid

The microgrid is shown in Fig. 1.2, which shows the connection of several DG (Distributed Generators) and loads to a common bus. DG systems or a direct main grid connection may power the loads linked to the microgrid. To further improve system stability and power availability, more esus may be linked to the microgrid [6].

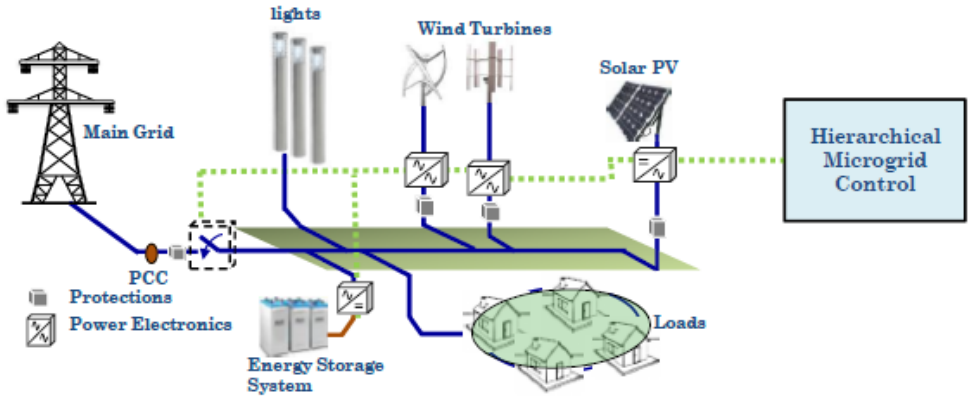

Fig. 1.2 Microgrid General Scheme

To convert energy from a certain voltage to another, power electronics equipment are used in a microgrid. An example of an ESU in action would be a bidirectional AC-DC converter, which controls the charging and discharging processes in an ac microgrid in response to the available energy. For microgrid voltage standards, wind turbine generators must be subjected to amplitude and frequency transformation using ac-ac converters. A dc-ac converter is necessary for solar photovoltaic (PV) generators to inject the greatest amount of usable microgrid with energy. The microgrid's common bus is connected to loads like residential dwellings and streetlights. Either the primary grid or islanded mode operation may be enabled for the common bus. To maximize energy production, assure acceptable power quality, and increase stability and resilience in the

microgrid, any numbers of controllers handle each one of the interconnections indicated above. Because of their inherent compatibility with legacy energy distribution systems, three-phase alternating current microgrids were the focus of this investigation.

1.1.2 Microgrid Hierarchical Control

Various hierarchical layers are usually used for microgrid control. When looking for a standardized control structure for microgrids, one of the best options is offered in [7], which is accessible elsewhere in the literature. As seen in figure 1.3, the authors established a standard for all microgrid control levels.

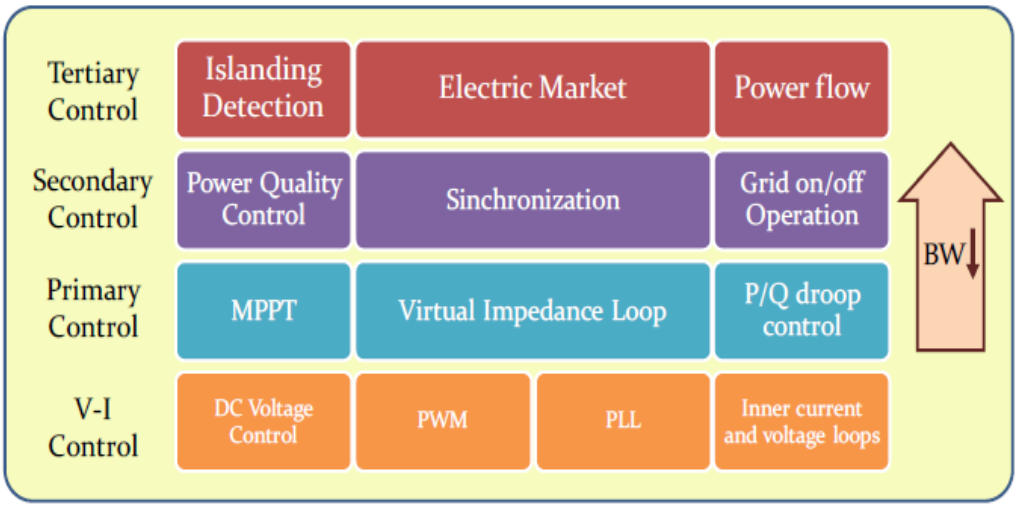

Fig. 1.3. Hierarchical Control Levels in Microgrids [7]

There are four tiers of control: V-I, primary, secondary, & tertiary. To achieve power quality standards for frequency, amplitude, and harmonic distortion, the inverter's v-i control level controls the waveform of the output signal. Generators' ability to feed electricity into the grid is controlled by primary control. Managing the quality of microgrid electricity is done via secondary control. Lastly, concerns pertaining to energy markets are handled by tertiary control, which includes power sharing between microgrids and the main grid, managing battery consumption, estimating energy production values, responding to unexpected changes in generator output, etc. as more control levels are implemented, microgrid control bandwidth drops. Specifically, the bandwidth is greatest for v-i control and lowest for tertiary control. With a broad bandwidth, you may expect minimal noise attenuation, quick dynamics, and very negative poles. Conversely, the microgrid closed-loop poles are closer to the imaginary axis,

dynamics are slower, and noise attenuation is strong when the bandwidth is limited. Because their dynamics are obviously different, these control levels are usually developed independently. What follows is an explanation of the four distinct degrees of control.

1.1.2.1 Voltage and Current Control (V-I Control)

Inverters are controlled by the v-i control level, which controls the output voltages and current. An inverter generator's typical v-i control system is shown in Fig. 1.4.

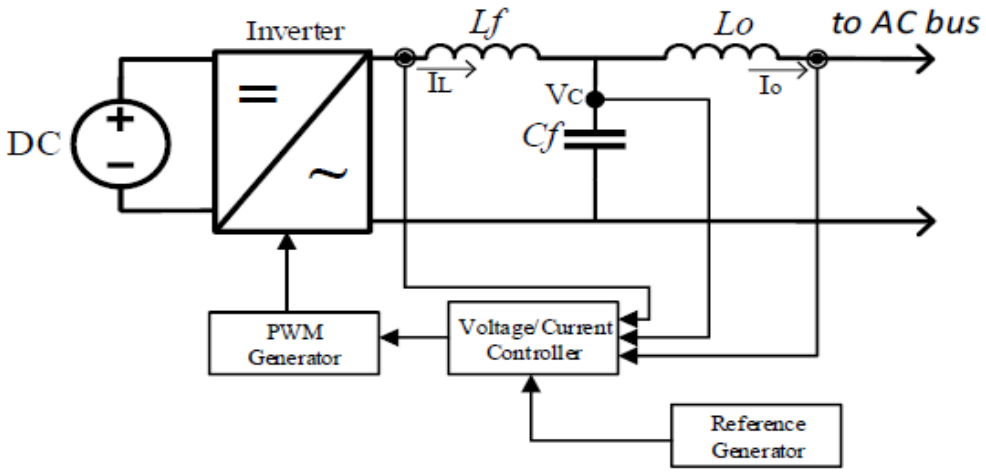

Fig. 1.4. A Typical V-I Control Scheme

A common component of inverters is an h-bridge design with IGBT transistors [8]. In response to a signal from the pulse-wide modulation (PWM) generator, these transistors are turned on and off at high frequencies. The inverter produces a square signal with a high frequency and varied duty cycle as a result of the transistors' switching activity. A peak at the base frequency (50 cycles per second or 60hz) and harmonic at the PWM switching frequency characterize the inverter's output signal in the frequency domain. Using an output filter, these harmonics may be reduced. To lessen power consumption, this output filter uses reactive components. The output of a filter may usually be an l-type, LLCL, LC, or LCL filter. All of these filters have their own set of pros and cons [9]. Direct current injection into the main grid, for instance, is a good fit for an l filter. In comparison to the LC, LCL, and LLCL filters, this one performs a poor job of dampening harmonics. A v-i controller takes signals from filter elements, computes them, and then uses the resulting control output to follow the signal from a reference generator, thereby closing the control loop. One or three phases may be used in inverter devices. The majority of uninterruptible electrical power supply (ups) systems employ single-phase inverters. Microgrid

systems often make use of three-phase inverters due to their simplicity of deployment inside conventional distribution networks. Both synchronous reference frames (DQ) and stationary reference frames (ABC or) may be used to analyze three-phase inverters without sacrificing generalizability [10]. In the ABC coordinate system, where a, b, & c represent the voltage or current in every phase, the stationary three-phase reference frame is often represented. There is a two-and-a-half-degree change between neighboring phases in the ABC frame. In an ABC frame, a unitary output vector is defined as:

$$v_{abc} = [v_a v_b v_c]^T = \left[\cos(\omega t) \quad \cos\left(\omega t - \frac{2\pi}{3}\right) \quad \cos\left(\omega t + \frac{2\pi}{3}\right)\right]^T \tag{1.1}$$

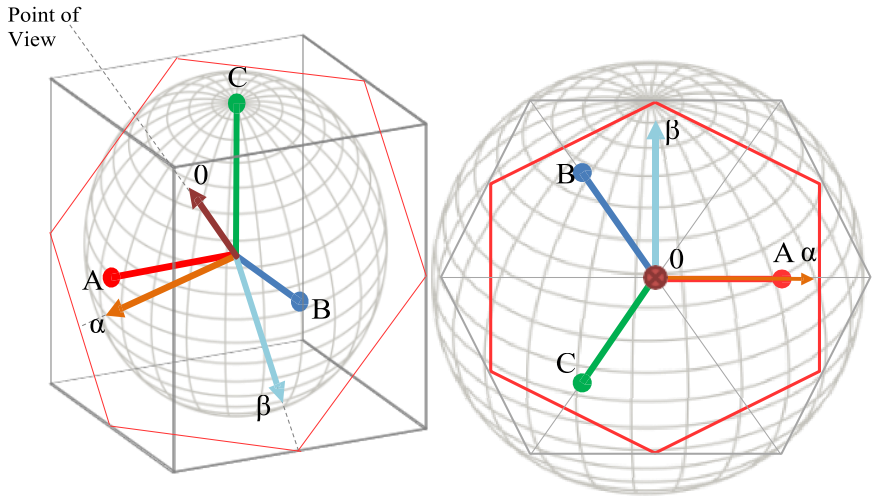

Fig. 1.5 Abc to $\alpha\beta 0$ Clarke transformation. (a) ABC and $\alpha\beta 0$ from a perspective point of view. (b) ABC and $\alpha\beta 0$ from an isometric point of view

Figure 1.5(a) shows another possible representation of the ABC frame in cartesian coordinates, where three orthogonal vectors stand for each phase. Rotating in the 0-plane, shown by the red hexagon, is the balanced three-phase operating vector. Figure 1.5(b) shows the conventional two-dimensional ABC diagram, whereas figure 1.5(a) shows the identical three-dimensional system viewed from an isometric perspective. It is possible to rotate the abc frame in such a way that both of the vectors are in the zero-plane and vector c becomes perpendicular to it. This is how the 0 frame, which is a two-vector reference, is created from a three-vector reference. The Clarke transformation, which is famous, is this

$$v_{\alpha\beta 0} = [T_{\alpha\beta 0}] v_{abc} \tag{1.2}$$

$$\begin{bmatrix} v_\alpha \\ v_\beta \\ v_0 \end{bmatrix} = \sqrt{\frac{2}{3}} \begin{bmatrix} 1 & -\frac{1}{2} & -\frac{1}{2} \\ 0 & \frac{\sqrt{3}}{2} & -\frac{\sqrt{3}}{2} \\ \frac{1}{\sqrt{2}} & \frac{1}{\sqrt{2}} & \frac{1}{\sqrt{2}} \end{bmatrix} \begin{bmatrix} v_a \\ v_b \\ v_c \end{bmatrix} \quad (1.3)$$

Because it stands for nothing in a balanced system, the vector with the value 0 is usually left out of the statement. The primary goal of applying the Clarke transform is to simplify and decrease computations by removing a component that is common among all 3 reference vectors within the ABC frame. In figure 1.6, the three-phase operational vector ✏ is seen rotating on the two-dimensional cartesian plane inside the frame. In other words, and stand for the sine and cosine functions, respectively.

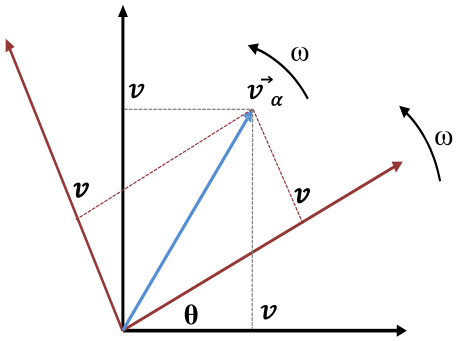

Fig. 1.6.To *dq* Frame Transformation

By projecting onto an auxiliary cartesian frame that rotates at its nominal angular frequency, the cosine and sine functions will take on constant values. Figure 6 shows a transformation that is the same as the famous park transformation. A three-phase vector in motion from one reference frame to another must undergo the following transformation in order to become a static vector in dq coordinates, which is a synchronous reference frame

$$\begin{bmatrix} v_d \\ v_q \\ v_0 \end{bmatrix} = \begin{bmatrix} \text{COS}(\theta) & \text{SIN}(\theta) & 0 \\ -\text{SIN}(\theta) & \text{COS}(\theta) & 0 \\ 0 & 0 & 1 \end{bmatrix} \begin{bmatrix} v_a \\ v_\beta \\ v_0 \end{bmatrix} = \sqrt{\frac{2}{3}} \begin{bmatrix} \text{COS}(\theta) & \text{COS}\left(\theta - \frac{2\pi}{3}\right) & \text{COS}\left(\theta + \frac{2\pi}{3}\right) \\ -\text{SIN}(\theta) & -\text{SIN}\left(\theta - \frac{2\pi}{3}\right) & -\text{SIN}\left(\theta + \frac{2\pi}{3}\right) \\ \frac{1}{\sqrt{2}} & \frac{1}{\sqrt{2}} & \frac{1}{\sqrt{2}} \end{bmatrix} \begin{bmatrix} v_a \\ v_b \\ v_c \end{bmatrix} \quad (1.4)$$

it is significant to remember that the norm of the three-phase vectors is preserved by the normalized transformations in (3) and (5), so:

$$v_d^2 + v_q^2 + v_0^2 = v_a^2 + v_\beta^2 + v_0^2 = v_a^2 + v_b^2 + v_c^2 \quad (1.5)$$

Figure 1.7 displays the final result of the transition from the ABC frame to the DQ frame and back again. To maintain the transformation norm, observe that the amplitude is multiplied by a factor of √2⁄3. At this stage, PLL techniques in a DQ frame are usually used to synchronize the grid. The pulse-width-modulation (PLL) circuit raises the angular frequency of the three-phase signal until its q component goes to zero. To prevent current spikes during connections, the produced signal is synchronized with the main electrical grid in this manner [11].

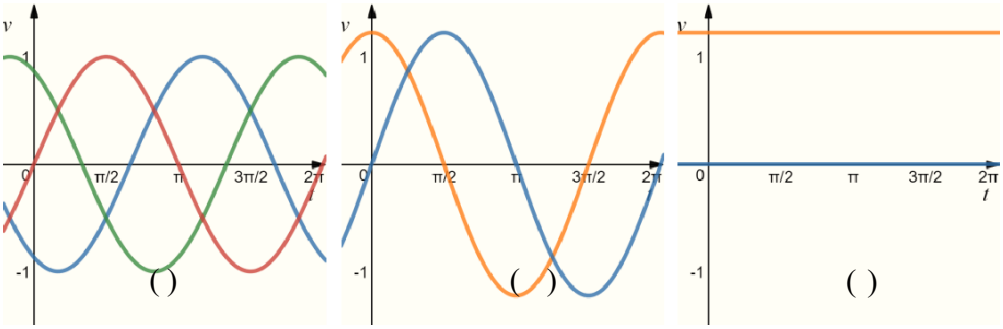

fig. 1.7. Complete transformation process from *abc* frame to *dq* frames.
(a) *abc* frame. (b) frame. (c) *dq* frame

The v-i control loop's control objectives are mentioned below [9]:

- Faultless tracking of the sinusoidal reference signal for voltage or current.
- Harmonic rejection to maintain the percentage below 5 percent, as required by IEEE standard 1547[12].
- High resilience to changes in the microgrid or abrupt loads.
- Grid synchronization with PLL methods applied.

A great deal of research proposes various control mechanisms to accomplish these goals [9]. There are a few ways to classify these control strategies: classical, optimum, and robust.

Classical Controllers: when we talk about classical controllers, we're usually referring to Laplace-domain controllers with common structures like P, PI, or PID. Another traditional controller that is covered in this article is the proportional-resonant (pr) controller, which is a variation of the pi controller. The ‘tuning’ aspect of the p, pi, PID, and pr controllers makes their implementation fairly easy, which is why they are commonly employed in industry. Equation (7) depicts a typical PID controller to demonstrate this idea:

$$K_{PID}(s) = k_P + \frac{k_I}{s} + sk_D \tag{1.6}$$

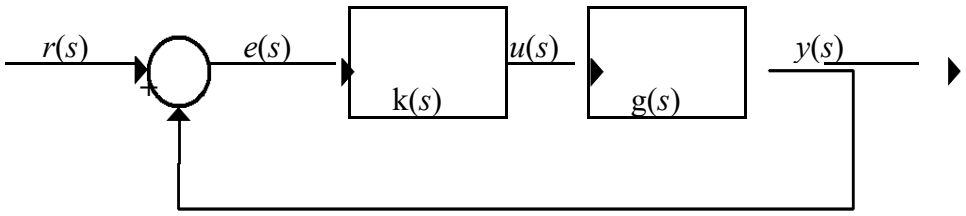

Fig. 1.8. Typical Closed-Loop Control Diagram

The block diagram structure of classical controllers resembles that of figure 1.8. In this case, the plant is represented by (), and the classical controller (), which could be p, pi, pid, or pr, is "denoted by. The block diagram in figure 8's closed-loop transfer function is provided by:

$$T(s) = \frac{Y(s)}{R(s)} = \frac{K(s)G(s)}{1+K(s)G(s)} \tag{1.7}$$

Sents a pole at = 0. This suggests an open-loop gain that is infinite at a frequency of 0 Hz. Put otherwise, there is no steady-state error when the open-loop transfer function of a pid closed-loop transfer function () tends to 1 at a frequency of 0hz.

When controlling a microgrid v-i, a pi controller is frequently utilized to maintain a steady state condition by regulating the output voltage or current in a DQ synchronized reference frame. A similar use for pr controllers is the regulation of output current or voltage in a reference frame that remains stationary. The following data transfer function is shown by a pr controller:

$$K_{RES}(s) = k_P + \frac{k_R s}{s^2+\omega_n^2} \tag{1.8}$$

What is the nominal microgrid angular frequency and where is the resonant control gain? At a nominal frequency, the terms$s^2 + \omega_n^2 = (j\omega_n)^2 + \omega_n^2$ becomes zero. Consequently, at the nominal frequency, the pr controller's open-loop gain is unlimited. When a sinusoidal reference signal oscillates at the nominal frequency, the pr controller achieves zero steady-state error if it has an infinite open-loop gain [14].

Optimal Controllers: Modeled in the state-space domain, the LQR approach forms the basis of optimal controllers. The LQR seeks to decrease the input and state energies. Kalman filters and LQG controllers are examples of methods that derive from this approach [15]. Heuristic approaches like PSO (Particle Swarm Optimization), which employs a group of agents to systematically search for the best value of a given cost function, may also be used to synthesize

optimal controllers [16]. If the system is characterized in terms of the linearized state space, then optimum controllers are often applicable in this domain:

The state vector, which contains the values of all relevant variables, and the input vector are located at. The 'state matrix' is a matrix that describes the dynamics of a state. The 'input matrix' is a matrix that connects the input vector to the state vector. The state vector is related to the system's output by a matrix, which is called the output matrix. In the end, a matrix called a 'feedforward matrix' is used to establish a direct correlation between the system's input and output. The state-feedback controller, which might be denoted by a matrix or a vector, is described by the equation (10) figure 1.9[17] shows the basic schematic representation of a state-feedback controller

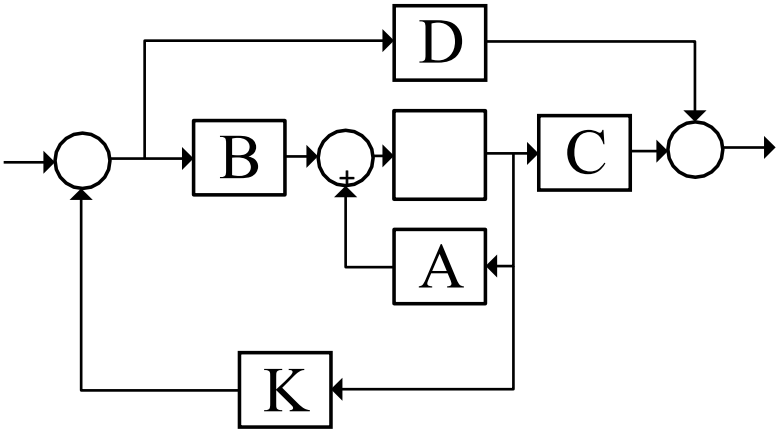

Fig. 1.9. state-feedback controller [17]

The LQR is the most often used optimum control technique. The quadratic cost function that this controller optimizes is given by:

$$J(t_0) = \frac{1}{2}x^T(T)S(T)x(T) + \frac{1}{2}\int_{t_0}^{T} (x^T Q x + u^T R u)dt \quad (1.9)$$

where and stand for, respectively, the weighting matrices in the input vector and state vector. Furthermore, the weighting matrix of the final state is represented by (). The following expression can be used to determine the ideal controller $*$:

$$K^* = R^{-1}B^T S(t) \quad (1.10)$$

Where ( ) is the solution to the ricatti differential equation:

$$-\dot{S} = A^T S + SA - BR^{-1}B^T S + Q \quad (1.11)$$

The algebraic RICATTI equation (are) can be solved to provide a suboptimal solution:

$$0 = A^T S + SA - BR^{-1}B^T S + Q \quad (1.12)$$

A less-than-ideal feedback matrix is located in equation (1.12) when the time-varying matrix () becomes static. The strong and stable characteristics of LQR controllers make them an attractive option for a broad range of control challenges.

The mathematical complexity of nonlinear controllers is larger than that of traditional control systems. At the v-i control level, nonlinear controllers may be categorized as either hysteresis controllers, feedback-linearization type controllers, or sliding mode controllers [9]. When compared with other control approaches, these con-trollers likewise need greater processing resources. A performance assessment of these methodologies also has its drawbacks. Because of these factors, nonlinear controllers will not be covered in this study.

The last step in designing controllers that account for uncertainties that can impact stability or performance is to use robust control techniques. The performance and uncertainty limits must be well-defined for this control method to work. Strong control techniques for v-i control, such as ∏ control and -synthesis, are often used.

These controllers reframe the control issue as an optimization problem, aiming to synthesis the optimal performance of a predetermined frequency response. Figure 1.10 shows a typical robust control block diagram. Signals ( ) and ( ) represent disturbances in measurements and processes respectively. Signals ( ) and ( ) represent reference and output signals correspondingly. Next, the following is the equation that characterizes the output:

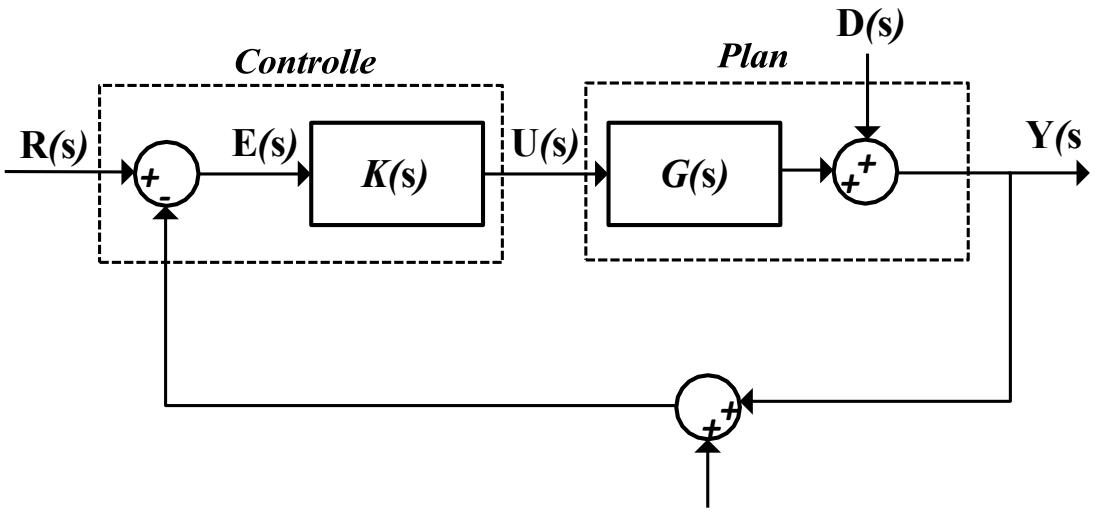

Fig. 1.10. Control block diagram with disturbances [18]

The output is immediately impacted by process and measurement disturbances via various transfer functions, as can be shown in (15). Determining the open-loop (), sensitivity (), and co-sensitivity () transfer functions:

$$Y(s) = \frac{D(s)}{I+K(s)G(s)} + \frac{K(s)G(s)}{I+K(s)G(s)}[R(s) - M(s)] \tag{1.13}$$

This is another way to express equation (15). As a result, it is clear that the impact of process perturbations on the output of closed-loop systems. There is a correspondence between the effect of measurement disruptions on closed-loop applications system output and the function. This means that a controller () may be programmed to act in a certain way on either () or (). It should be noted that, according to the definitions of () and ( ):

$$S(s) = [I + K(s)G(s)]^{-1} \tag{1.14}$$

$$T(s) = \frac{K(s)G(s)}{I+K(s)G(s)} \tag{1.15}$$

$$L(s) = K(s)G(s) \tag{1.16}$$

$$T(s) + S(s) = I \tag{1.17}$$

Because of this, we may say that the functions are mutually supportive. Disruptions to measurements tend to Be high-frequency, while process disturbances tend to be Low- frequency. For this reason, although it is designed to work as a low-pass filter in ∞ control, it is meant to behave as a high-pass filter. The predefined weighting functions 1 and 2 are used to minimize the infinity norm of the sensitivity and co-sensitivity transfer functions. One way to define the ∞ problem is:

$$\min_K \left\| \begin{matrix} W_1 S \\ W_2 T \end{matrix} \right\|_\infty \tag{1.18}$$

The greatest gain on a certain frequency response is represented by the operator ‖. ‖∞, which is defined by the infinity norm. For multivariable systems, this method works well for defining the appropriate frequency response. The usage of ∐ controllers to mimic pr controllers is prevalent. High processing costs and susceptibility to nonlinearities are two of the downsides of the ∐ controllers.

−**Synthesis controllers**: robustness bound wherein stability and performance may be reached is defined by this controller, which is on the basis of ∞ control and employs linear matrix inequalities (LMI). Alternate approaches include optimization techniques such as the glover-doyle algorithm [18], particle swarm optimization [19], or iterative methods like LQR [15].

The literature on inverter v-i control may also include various control systems, such as adaptive, predictive, and intelligent control [9]. The absence of methods to evaluate these tactics' stability and performance metrics in comparison to the ones already stated puts them beyond the purview of this study [7]. An outline of the key contributions to V-I control techniques is provided in section 2.1

1.1.2.2 Power Sharing Control (Primary Control Level)

The main control level is in charge of regulating how much power each dg may share on the shared ac bus. In addition, the main control level has the option to transfer the maximum power generated by the RES to the main grid. There are two main types of power in alternating current (AC) systems: active and reactive. The author of [20] offers a theory that may be applied to three-phase systems in general to determine the active and reactive power at any given time. Whether the currents and voltages are balanced or unbalanced, sinusoidal or non-sinusoidal, and with or without zero sequence, this method will work. In figure 1.11, we can see a three-phase power supply linked to either the load or a network, which might stand in for the standard ac bus. The values of, and are measured in relation to the ground

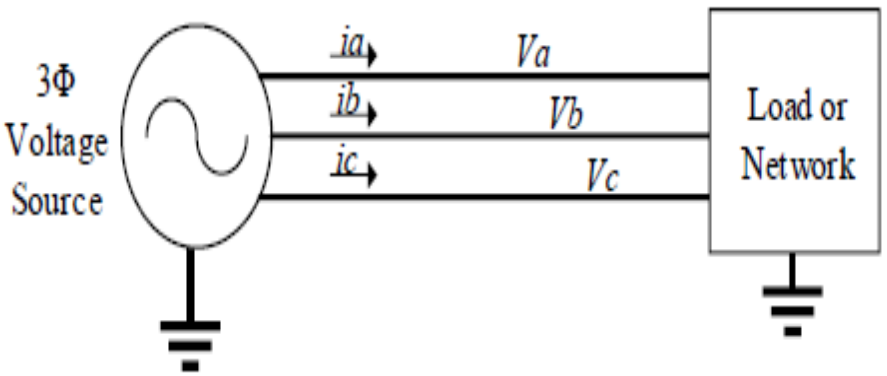

Fig. 1.11. Three-phase system structure [20]

The dot product of the voltage and current vectors can be used to describe instantaneous active power as follows:

$$P = v \cdot i = v_a i_a + v_b i_b + v_c i_c \tag{1.19}$$

Likewise, the cross-product of the voltage and current vectors can be used to describe the instantaneous reactive power as follows:

$$S = \sqrt{P^2 + Q^2} \tag{1.20}$$

The definition of apparent power can be used to establish a connection between active and reactive power.

$$P = v_{\alpha\beta 0} \cdot i_{\alpha\beta 0} = v_\alpha i_\alpha + v_\beta i_\beta \tag{1.21}$$

$$Q = v_{\alpha\beta 0} \times i_{\alpha\beta 0} = v_\alpha i_\beta - v_\beta i_\alpha \tag{1.22}$$

These formulae lead to the conclusion that the dot product of the instantaneous active and reactive power, which represent two orthogonal vectors, equals zero [20]. The active and reactive instantaneous power can also be expressed in the 0 do-main[21] to further develop this idea:

$$\begin{bmatrix} P \\ Q \end{bmatrix} = \begin{bmatrix} v_\alpha & v_\beta \\ -v_\beta & v_\alpha \end{bmatrix} \begin{bmatrix} i_\alpha \\ i_\beta \end{bmatrix} \tag{1.23}$$

Assuming a resistive load causes the output voltage and current to be in phase, the reactive power components in equation (1.23) will cancel each other out, leaving just active power usage. Regarding the. The powered components will cancel each other out and the power consumption will be entirely reactive if the current and voltage at the output are⁄4 phase-shifted because of an inductive or capacitive load. Therefore, the power that does not go into the load but is instead transferred between reactive components and ac sources is known as reactive power [20]. This means that reactive power is a source of transmission line energy losses rather than a contributor to energy transfer across systems [10]. An electrical study is required to examine power sharing among DGs. An AC inverter generator is seen in Fig. 1.12 coupled to a stiff ac voltage source, which might be the main electrical grid or the common AC bus of the microgrid.

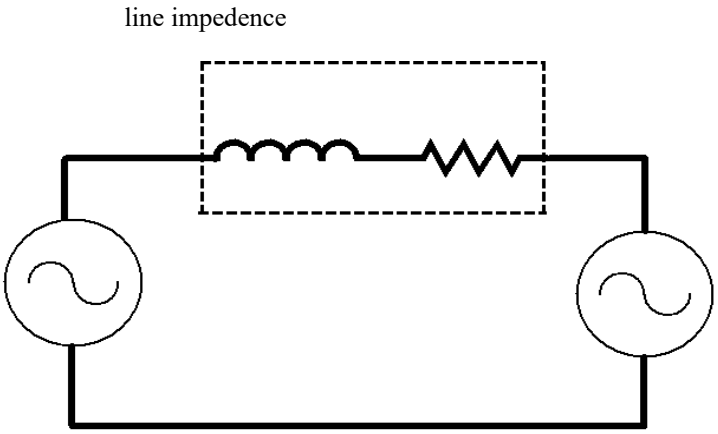

Fig. 1.12. a DG Connected to an AC Stiff Source

The active power and reactive power received by the main grid in a system like the one shown in Figure 12 are determined by:

$$P = \frac{1}{R^2+X^2}(RE^2 - REV\cos\delta + XEV\sin\delta) \quad (1.24)$$

$$Q = \frac{1}{R^2+X^2}(XE^2 - XEV\cos\delta - REV\sin\delta) \quad (1.25)$$

In this case, reflects the phase difference between two ac power sources. The active and reactive power are shown by equations (1.24) and (1.25) to be nonlinear functions of the voltage amplitude and phase shift of the two ac sources. That means you can regulate the active and reactive power by adjusting and e. keeping this idea in mind, the fundamental goals of primary control are as follows: based on each dg's rated power, control the sharing of active and reactive power. It is preferable to do this activity without communicating. Working in grid-linked mode, injecting a certain quantity of active and reactive electricity into the main grid prevents harm to energy conversion systems by reducing the occurrence of overcurrent incidents. In the previous ten years, a plethora of methods have been released to tackle these goals. One way to classify them is as either autonomous controllers or controllers that rely on communication.

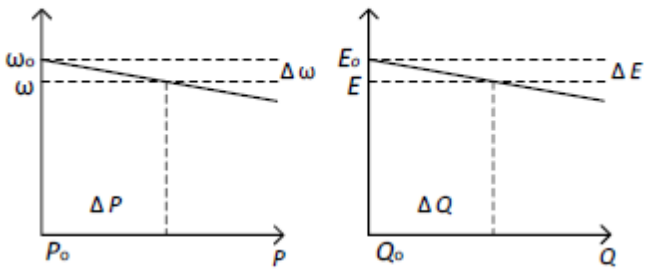

Fig.1.13. Active and Reactive Power Droop Control Functions

$$\omega = \omega_0 - m(P - P_0) \tag{1.26}$$

$$E = E_0 - n(Q - Q_0) \tag{1.27}$$

Centralized [23], master-slave [24], average load sharing [25], [26], and circular chain approach [27] are some types of communication-based controllers. Due to their reliance on continuous connection between DGS, communication-based controllers are not reliable and robust. Contrarily, the majority of the published work on distributed microgrid power-sharing controls in the previous decade has focused on autonomous controllers, which are shown to be more dependable [28].

The famous droop control approach [6] is the foundation of autonomous controllers; it allows for the emulation of synchronous machine activity without requiring communication between generators. As the active power demand rises in a synchronous machine, the voltage frequency falls [29, 30]. In a similar vein, an increase in reactive power demand causes a decrease in voltage amplitude. Equations (28) and (29) may be used to simulate the droop characteristics of synchronous power generators, allowing the inverter to exchange active and reactive power with the common AC bus or another DG without communication:

The nominal values of active power, reactive power, operating frequency, and amplitude are denoted by $_0$, $_0$, $_0$, and $_0$, respectively. Each DG's capacity to generate electricity is directly correlated with its coefficients, which show the droop rates. Figure 13 displays the droop control curves for the sharing of active and reactive power.

Connected DGs with droop control, as displayed in Fig. 1.14, cause each generator to lower its frequency as well as amplitude in response to its active and re-active drooping curves. When the frequency of all generators reaches the same level and the voltage on the AC bus becomes stable, we have achieved a steady state [31].

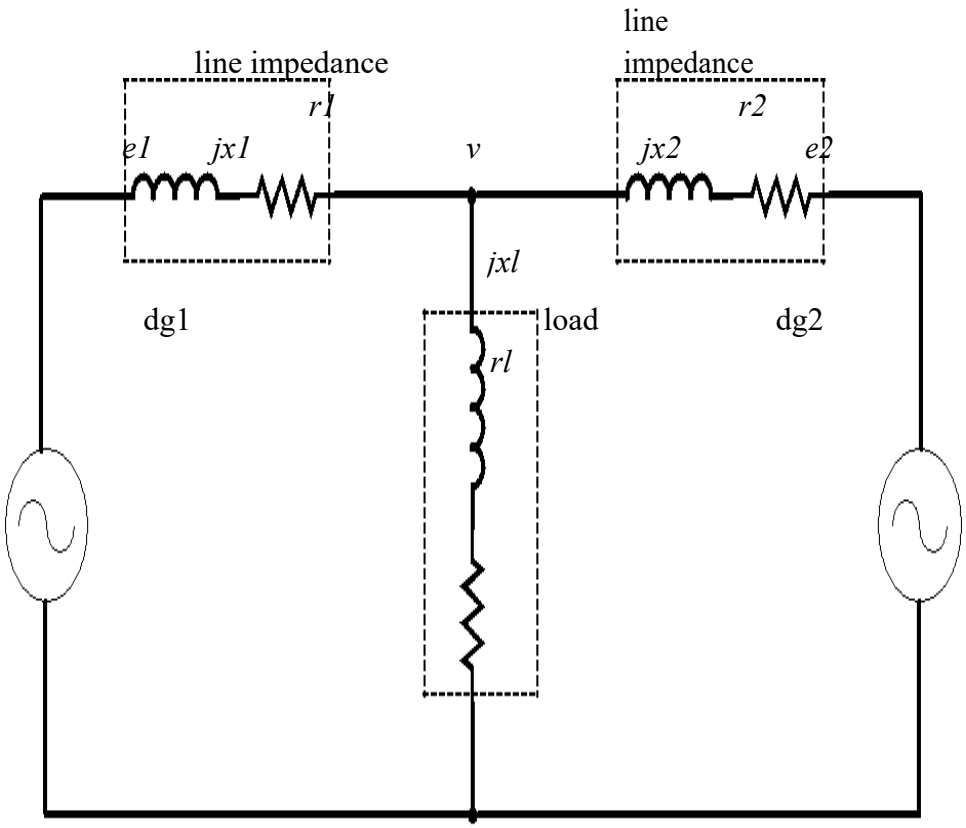

Fig. 1.14. Two DG's Sharing a Load

A common main control hierarchical control diagram is shown in Fig. 1.15. For a main controller-generated sinusoidal voltage with amplitude e and frequency, a V-I control loop is utilized. A low-pass filter power calculation block is part of the main droop controller; it calculates the average value of the power that is active and reactive powers. In response to the signals from the two droop controllers, the reference generator produces the signal as a sine wave with a voltage amplitude e and a frequency

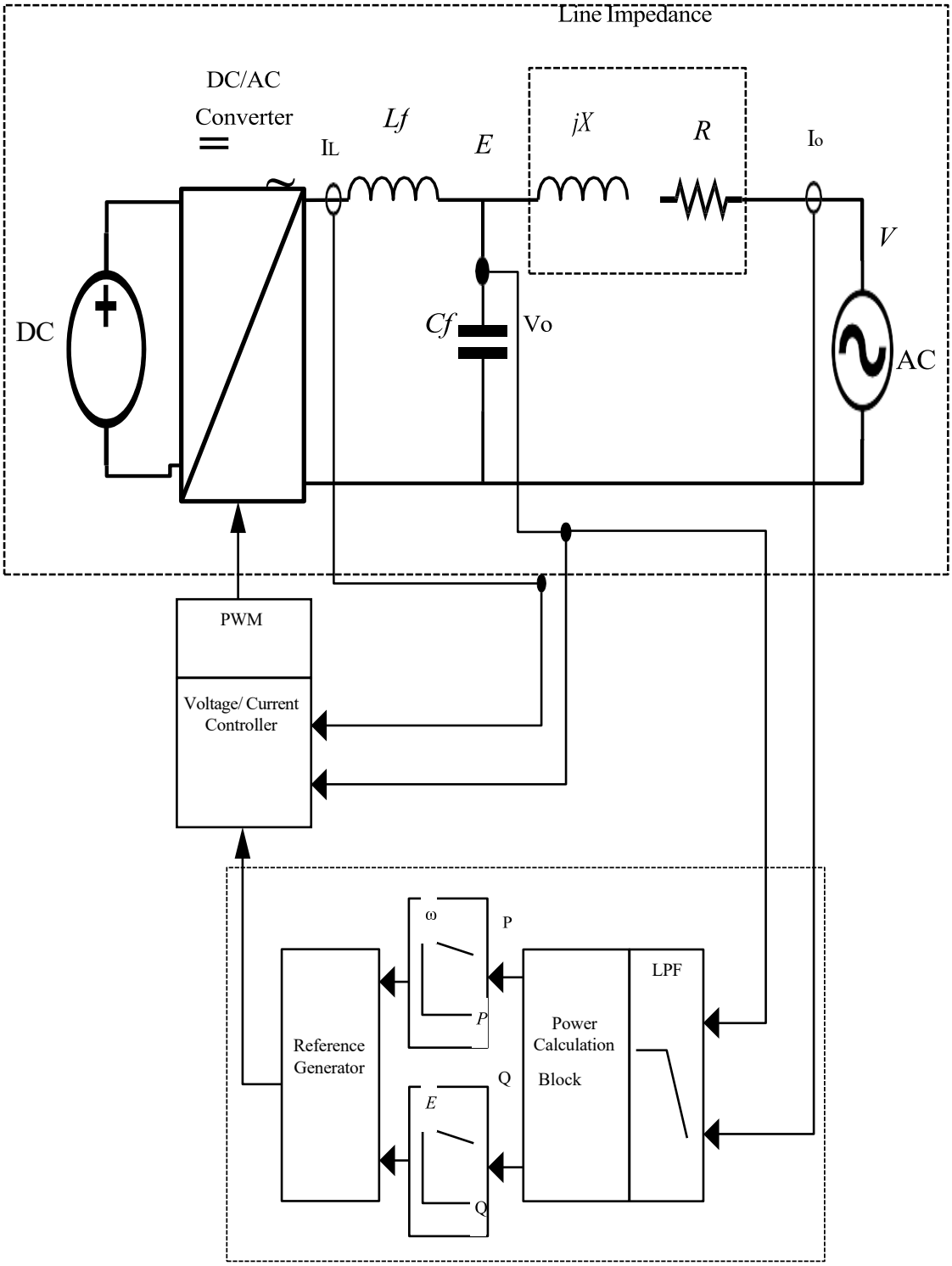

Fig. 1.15. Single phase Inverter Connected to a stiff AC source with Voltage-Current Control and Power Sharing Droop Control

- Since droop management does not need communication between generators, it provides dependability to microgrid systems. Nevertheless, this approach does have a few downsides, such as droop control establishes a direct correlation between the active power given and the phase lag, which leads to a lack of controllability[32], [33]. The same holds true for the link between reactive power with the amplitude of the signal. The traditional droop approach presupposes that reactive and active power are independent. Because of this, controlling active power and reactive power may be done with only one input variable, namely voltage and frequency. This suggests that achieving many control goals simultaneously is challenging. The regulated system's settling time, for instance, and the regulation of voltage and frequency are both affected by this tradeoff.
- A minor departure from the operational point occurs when the complete microgrid achieves a steady state of supplied power among DGs [28]. This is because the droop management is on the basis of a shared lowering of voltage & frequency.
- You need to know the line impedance beforehand: the traditional droop technique presupposes a highly inductive line of transmission for power sharing [7, [28], [34]]. For big transmission systems, this is correct. This assumption, however, may be challenged by the fact that certain microgrids that share low-voltage electricity may encounter transmission lines that are very resistive.
- Unwanted voltage behavior may occur when reactive power fluctuates significantly with critical loads, as reactive power is managed by adjusting the signal amplitude, and the amplitude may differ between generators [34].
- The distortion power, which is induced by harmonic currents produced by nonlinear loads, is not controllable. Traditional droop techniques lack the ability to quantify distortion power and hence cannot regulate the microgrid's distortion power allocation [35].

Depending on the architecture, voltage levels, operating mode, etc., of the microgrid, droop controllers may take several forms. In [28], we find a comprehensive analysis of most of the droop controller variants that have been published. In order to manage the transient response, power-sharing controllers often utilize conventional pi controllers. Due to the mathematical complexity of the main control level, optimum control techniques are not often applied. Furthermore, developing optimum or robust control techniques like LQR, PSO, ∞, or lmi becomes challenging when the power-sharing issue is formulated in a state-space domain. To improve the microgrid primary control's resilience and transient responsiveness, the literature study presented in section 2.2 examines droop control techniques.

The distribution of electricity among DGs is controlled at the primary level. There is no primary electrical voltage reference for the microgrid to follow while it is operating in island mode without connectivity. Voltage and frequency fluctuations on the shared ac bus result from this lack of reference. A second control layer is used to adjust for these variations and return the microgrid's voltage and frequency to their nominal levels. In addition, when transmission line imbalances occur, the generation is compensated for by the secondary control level.

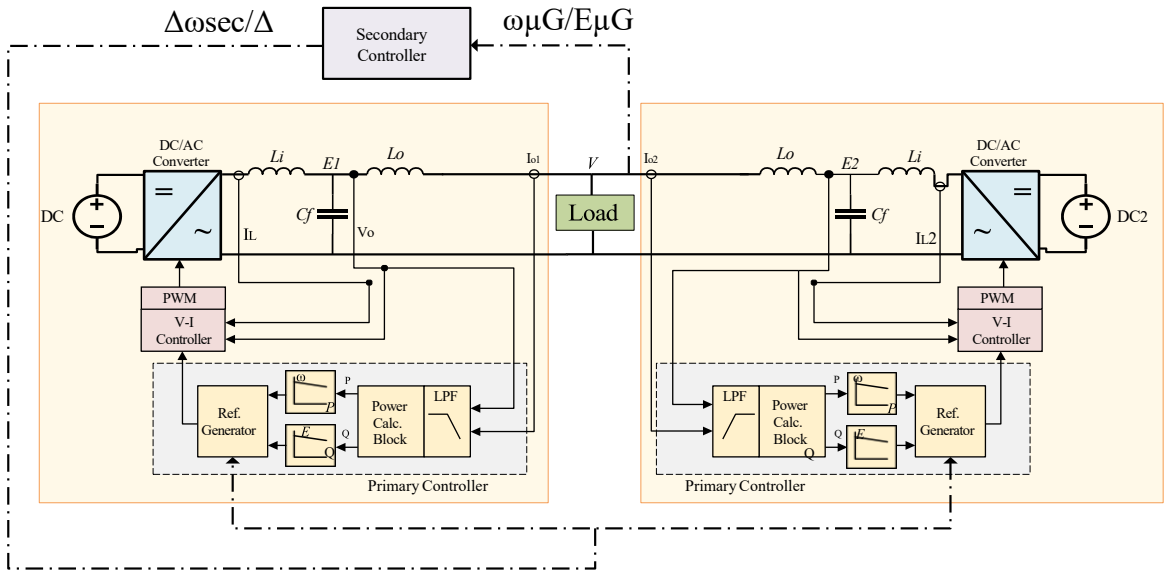

Fig. 1.16. Typical Scheme of a Secondary Control Level to Recover Microgrid's Voltage and Frequency

According to references [7], [36], figure 1.16 depicts a standard secondary control level strategy for voltage and frequency recovery in a microgrid with 2 island generators. The main controller will utilize the compensation signals (δ and δ) generated by the secondary controller to restore the nominal values of the common ac bus's voltage and frequency, which are read from the common ac bus by the secondary controller. Having to communicate on a local level between DGs is one of the major problems with secondary control. Because secondary control dynamics are slower, their communication is more dependable than main control's. Because of the sluggish dynamics, low-speed communication technologies are more practical to use [37]. Decoupling from both primary and v-i stages of control is also possible due to the sluggish dynamics of secondary control. Due to their sluggish dynamics, traditional controllers like p, pi, or pid are usually used as a basis for secondary controllers. The controllers in question also pay little attention to the dynamics and resilience characteristics of the microgrid, preferring instead to concentrate on the power quality of the grid.

1.1.2.3 Tertiary Control for Microgrid Power Sharing

The microgrid's active and reactive power sharing with the main grid is regulated at the tertiary control level. Taking Fig. 2's microgrid system into account, the tertiary control measures the microgrid's power output to the larger grid. The tertiary control level then communicates a reference value to the secondary control level in accordance with the control aim such that the voltage and frequency of the microgrid's shared AC bus may be adjusted to control power transfer to the larger grid [22].

The tertiary controlling level is also responsible for managing expenses and resources. To determine when to inject the generated electricity into the main grid or charge the batteries, for instance, the tertiary controllers may interact with each DG or ESU. It is common practice to optimize expenses, availability of energy, battery life cycle, etc., while designing the tertiary controller. Combining heuristic approaches with PSO and intelligent control strategies is a common approach to solving these optimization issues [22]. Research into tertiary control is outside the purview of this thesis as its primary goal is not to strengthen the dynamics and resilience of microgrid

1.1.3 Discussions of Main Challenges In Microgrid Control

Such that the voltage and frequency of the microgrid's shared ac bus may be adjusted to control power transfer to the larger grid [22].

Section 1.1.3.1: Key Difficulties In Microgrid Management

A new option for integrating res into the traditional energy distribution and transmission system is microgrids. Hierarchical control, as we've seen in this chapter, may help you meet needs like quality of power, stability, and robustness. Increasing the use of microgrids in traditional energy distribution networks is not without its obstacles, but [7]. Prior to anything else, keep in mind that inverters aren't as heavy as those old-fashioned, high-powered synchronous generators. Microgrids are susceptible to harmonic distortion and high-frequency disturbances when subjected to nonlinear loads because of their low inertia. As mentioned in section 1.1.2.2, there are several complicated issues with power-sharing control. These challenges mostly stem from transmission line qualities and the tradeoffs between reactive power sharing and voltage regulation. Thirdly, issues with voltage and frequency fluctuations brought on by mains regulation might compromise power quality. A solid standardized foundation, including regulations, electrical standards, communication protocols, community socialization, etc., is necessary for microgrid integration.

1.2 Statement of the Problem

This study aims to solve the challenge of developing and executing a control strategy for isolated microgrids that incorporates v-i and power-sharing dynamics into 3-phase inverter-based generators. As far as we are aware, there are no formal ways that combine v-i and sharing of power control into one entity, even if there are approaches that enhance a microgrid's stability and responses to transients. Additionally, in order to conduct stability and robustness analysis, no state-space inverter models exist that include v-i and power-sharing dynamics. As a closed-loop model, every one of the studies we looked at incorporates control dynamics into their inverter models. The majority of robustness and stability analyses, however, need a plant model without control dynamics operating in an open-loop configuration.

We Want To Know How Successful A Control Mechanism Is By Asking: Incorporates Voltage-Independent And Power-Sharing Control In Comparison To Traditional Hierarchical Microgrids

Method for controlling chicles? In order to answer this issue, we suggest the following hypothesis: compared to standard hierarchical control techniques for microgrids, a control approach that combines v-i and power-sharing management improves microgrid stability, resilience margins, and transient responsiveness.

1.3 Objective of the Present Work

Below, you can find a description of the research work's aims. We begin by outlining the overarching goal of our study. Based on this, the specific goals are outlined.

1.3.1 Overarching Goal

The goal of this study is to formalize a control approach for isolated microgrids that uses three-phase inverter-based generators and incorporates V-I and power-sharing management.

1.4. Outline of the Thesis

1. Present an innovative v-i and power-sharing-dynamics-incorporating open-loop state-space models of an inverter-based generator.
2. Analyze the open-loop state-space framework for stability and resilience.
3. Check the state-space model using an open-loop. Formulate a control technique that optimizes performance and guarantees stability and robustness characteristics of the inverter-based generator in islanded mode.
4. Perform robustness and stability analysis to the controlled state-space model.
5. Validate controller performance.
6. Compare results against other control methods in the literature.

Chapter 2

Literature Review

In this chapter, we take a look at the research on ac microgrids, specifically at the current state of V-I and primary control. Using criteria including control technique, stability, robustness, response to frequency, and power quality, this chapter examines the referenced works through the lens of control systems. The primary developments in v-i controlling for microgrids with ac are discussed in the first part. A survey of recent developments in shared control is provided in the second part.

2.1 Voltage and Current Control (V-I Control)

The voltage that is output or current is controlled by the v-i control level in accordance with the requirements of the microgrid. Because of the strong correlation between voltage amplitude and phase and active/reactive power sharing, the regulation of voltage is often used in isolated microgrids. When the main grid is rigid and there is no need to generate an output voltage in order to inject a certain quantity of electricity, current control becomes very useful for grid-connected microgrids.[9]

The control techniques presented here may be broadly categorized into three types: classical, optimum, and robust. A synchronous reference frame and a stationary reference frame are both used to build these approaches. This section concludes with a brief overview of V-I control techniques.[10]

2.1.1 Classical Controllers

Because they are easy to build, classical controllers are utilized, as shown in section 1.1.2.1. Classical controllers often don't have complicated mathematical designs and only need their gains fine-tuned. Hierarchical control is shown with a classical controller, as seen in [36]. This paper presents full hierarchical control architecture for a microgrid operating in a fixed reference frame. [36]

Two PR controllers were used by the writers to provide sufficient voltage monitoring and current sharing.[39]

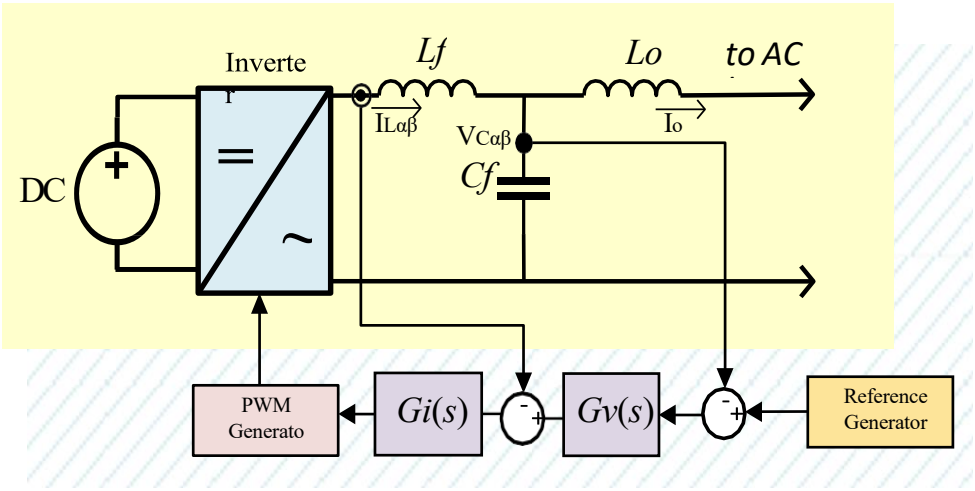

Fig. 2.1. V-I Control Structure Proposed in [36]

Furthermore, to ensure that harmonic currents are shared and to minimize harmonic distortion in voltage, a series of resonant filters are utilized in the current and voltage control loops. The following transfer function defines both variables as controllers

$$G_{v,I}(s) = k_P + \frac{k_R s}{s^2+\omega_0^2} + \sum_{k_h=5,7,11} \frac{k_h s}{s^2+(k_h\omega_h)^2} \quad (2.1)$$

These are the angular frequency and resonant gain of the harmonic *h*, respectively. Controllers can precisely follow the reference signal at harmonic 5, 7, and 11 with the use of resonant filters at those frequencies. To improve THD, the voltage controller has zero references at harmonics 5, 7, and 11. Improving the harmonic current share to the common ac bus is achieved by precisely tracking the current references produced by a voltage controller in the current controller. All microgrid control levels show satisfactory outcomes when using the method suggested in [36]. Having said that, we don't test for stability or robustness. Furthermore, both voltage and current controllers' gain settings were determined by trial & error, thus they don’t provide optimal performance or resilience.

Because they are easy to execute and based on the premise that the V-I control level's dynamics are much quicker than the primary control level's dynamics, similar techniques to [36] have been frequently employed in literature to develop higher control levels. Additionally, a synchronous

dq frame may be subjected to the same analysis as in [36]. The PI controller takes the position of the PR controller in the dq frame, and the harmonic frequencies are moved to the left of the range of electromagnetic waves by a factor of 0. References [38]–[42] detail a few uses of pi controllers at the V-I control level.

In [43], the pole positioning approach is used to create a state-feedback current controller. The controller is specifically designed for 3-phase inverters that are linked to the grid and use an LCL filter in a synchronous DQ frame. To provide precise monitoring of the internal inductor current, the controller employs an additional loop with a PI controller, as seen in figure 2.2.

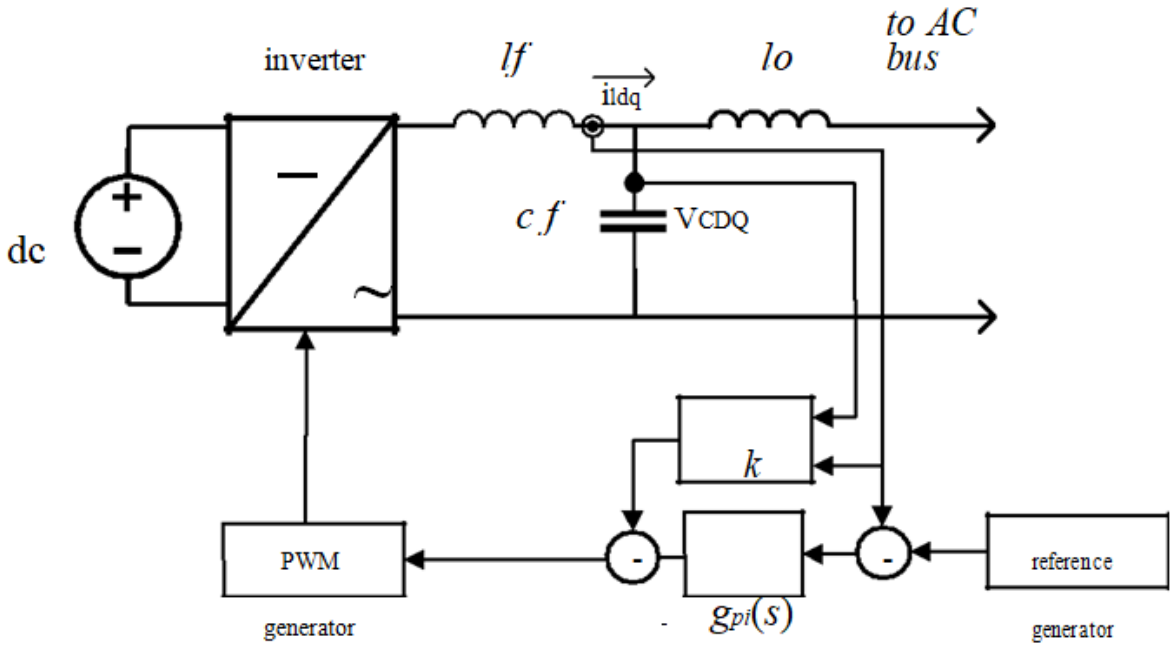

Fig. 2.2. State-Feedback and PI Control Implementation Presented In [43]

There are three primary processes to designing the controller given in [43]: first, determining the appropriate overshoot and settling time, and then computing the three required closed-loop poles. The second step in achieving the closed-loop poles is to calculate pi and state-feedback gains. The PI controller is then enhanced with an additional harmonic correction. With respectable tracking and little harmonic distortion, this controller produces satisfactory performance. One thing to keep in mind is that the controller was designed for a converter that is linked to the grid. Because of the main grid's ability to provide all the harmonics power to the nonlinear loads, voltage distortion from harmonics is kept low. Furthermore, an examination of the work's stability and resilience in the face of process or measurement perturbations is absent.

$$\vec{y}_{\alpha\beta} = \frac{\vec{u}_{\alpha\beta}}{p - j\omega_0} \tag{2.2}$$

In this case, the operator is called the complex derivative. Since the d and q axes are orthogonal, this analysis may be transformed into the dq frame. Compared to the traditional resonant filter, this method is computationally lighter. Because the rogi is only effective with signals that follow a positive sequence, however, its implementation is more complicated. Because of this, the resonant filter will not function in the event of a grid failure or line imbalance.

Presented in [45] is a pr controller that can rectify circulating currents in a single-phase inverter system that consists of many modular ups modules. Figure 2.3 shows the author's proposed method for calculating the average output current, which would then be used as both a feedforward and feedback signal. The circulating current impedance may now be controlled, which allows for frequency response adjustment and inverter-to-inverter circulating current minimization. There was a sufficient reaction to reduce circulating currents, according to the results. The average of the currents flowing out of each ups inverter is necessary for this application, however. Therefore, it is essential for every ups inverter to be able to communicate locally with a central measurement unit.

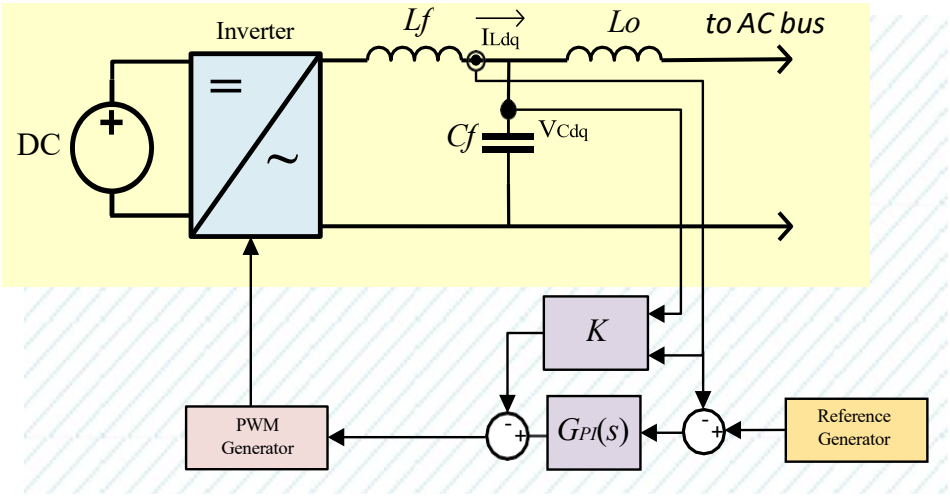

Fig. 2.3. Pr controller with average output current injection [45]

The simplicity of PI and PR controllers makes them the go-to for most classical control techniques at the V-I control level. No alternative laplace-domain controllers, like lead or lead-lag, were discovered in this literature study. When it comes to microgrid V-I control, lead-lag controllers provide additional advantages that are worth investigating.

2.1.2 Optimal Devices for Control

Numerical approaches are used to find the optimum value of a predetermined cost function, which characterizes optimal controllers. Some of the most well-known optimum control systems are Kalman filter estimators, particle swarm optimization, linear quadratic regulator control, and many more.

Using the DQ frame, an ideal v-i control method for a three-phase inverter is discussed in [46]. The author employs a 'perfect servo' controller (RSP) that minimizes total harmonic distortion (THD) and ensures flawless tracking via the employment of a series of resonant filters. The suggested block diagram for this approach is shown in figure 2.4. A state-feedback controller 1 is calculated using an LQR optimization approach and paired with the set of resonant filters (). To determine the best settings for the resonant filter gains, we utilize the state-feedback controller 1.

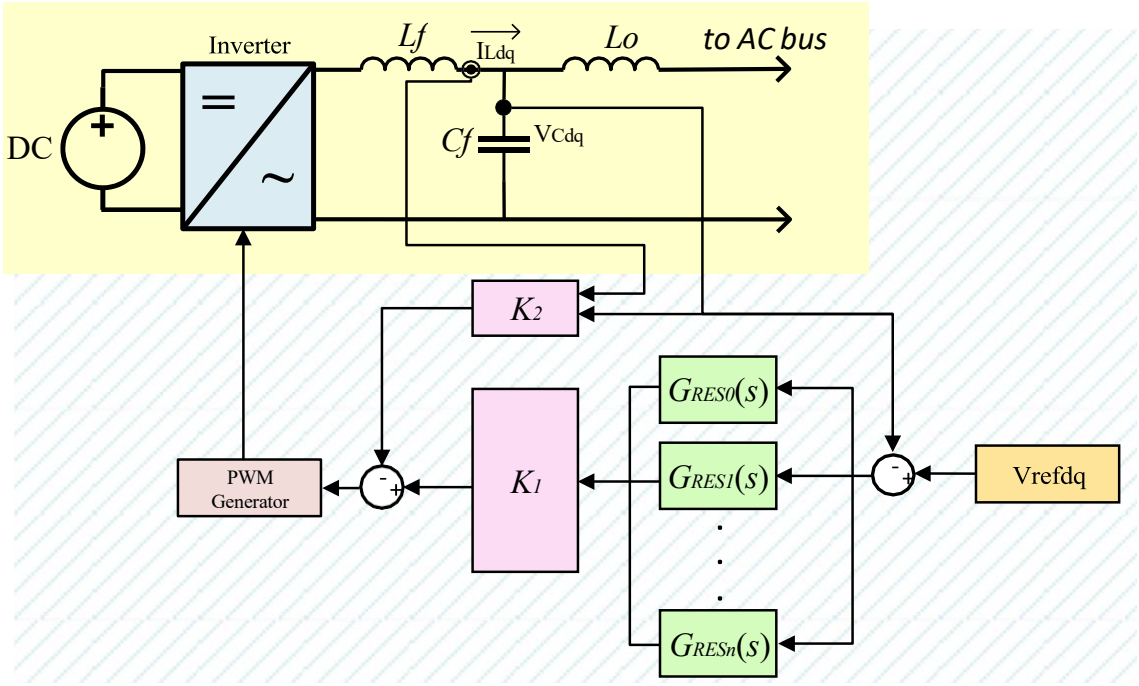

Fig. 2.4. RSP Controller with Optimal State-Feedback [46]

The output voltage, load current, load voltage, and delayed control signal are the five state variables needed by the state-feedback controller 2 to attain stability. It may not be feasible to detect voltage and current at the load side for the controller in microgrid applications, since this would imply that. An analogous method was devised in [47], wherein an ideal LQR controller was used to ascertain the pr controllers' gain values that ensure minimal losses of energy on an inverter with three phases linked to the main grid. Inductive-resistive impedance was used to

connect the 3-phase inverter to the main grid. So, to manage the quantity of electricity sent to the main grid, a current controller was suggested. The intended instantaneous power, which is the total of the active & reactive power, was divided by the grid voltage to get the current reference. The following pr controller was then used, which had the following transfer function

The two parameters that need optimizing using the LQR approach are 1 and 2. The outcomes of the simulation demonstrate that the present regulation and power sharing are functioning adequately. An appropriate method for integrating the v-i and main control levels is shown by this technique. Nevertheless, more investigation into the sharing of harmonic currents when operating in island mode is required.

The same author goes on to discuss a 3-phase voltage source inverter's pr gains in the ABC frame using an LQR controller in [48], which follows this work. Using a resonant filter operating at the nominal frequency, the author enhances the system states. Through the computation of ideal pr gains, this technique aims to maximize energy while attenuating the resonant peak in the frequency response of an LCL filter. This method produces acceptable outcomes; however, it can only be used for grid-connected inverters that do not exhibit harmonic distortion.

A grid-connected three-phase inverter with an LQG current controller was created in [49]. The LQG controller's block diagram is seen in figure 2.5. For the plant models in the DQ reference frame, the LQR synthesized the optimum pi control gains. To address grid imbalances and rectify the coupling between the d and q voltage components, a method known as filter current decoupled control (FCDC) and a grid voltage feedforward control/compensation (GVFC) approach were devised.

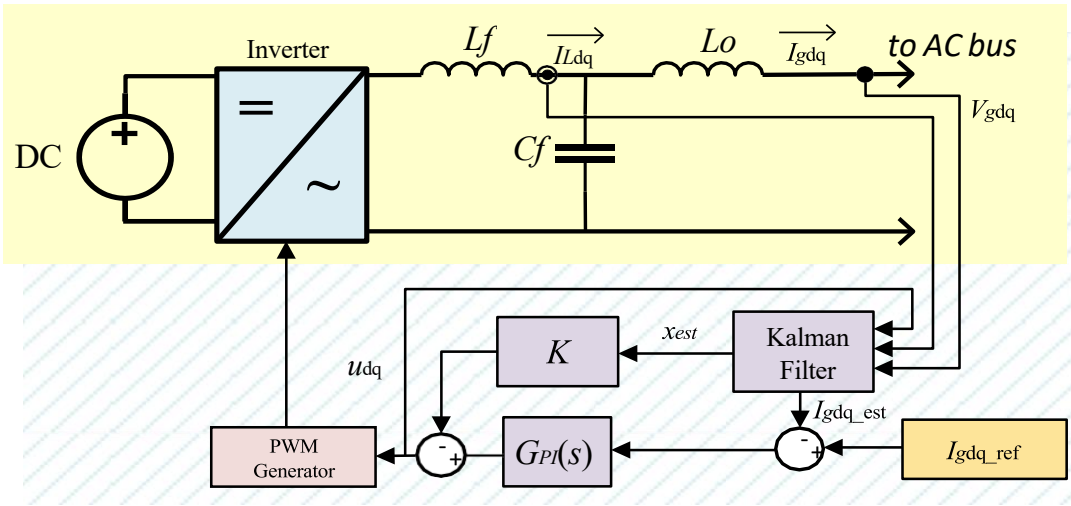

Fig. 2.5. LQG Implementation with a Servo Controller Approach [49]

Additionally, as seen in figure 2.6, a Kalman filter was created to predict the output current while taking into account the voltage on the grid as an external disturbance. A luenberger observer, the kalman filter synthesizes an ideal kalman gain l by minimizing the variation of the measurement error. You may find the whole history of the kalman filter's development in [15].

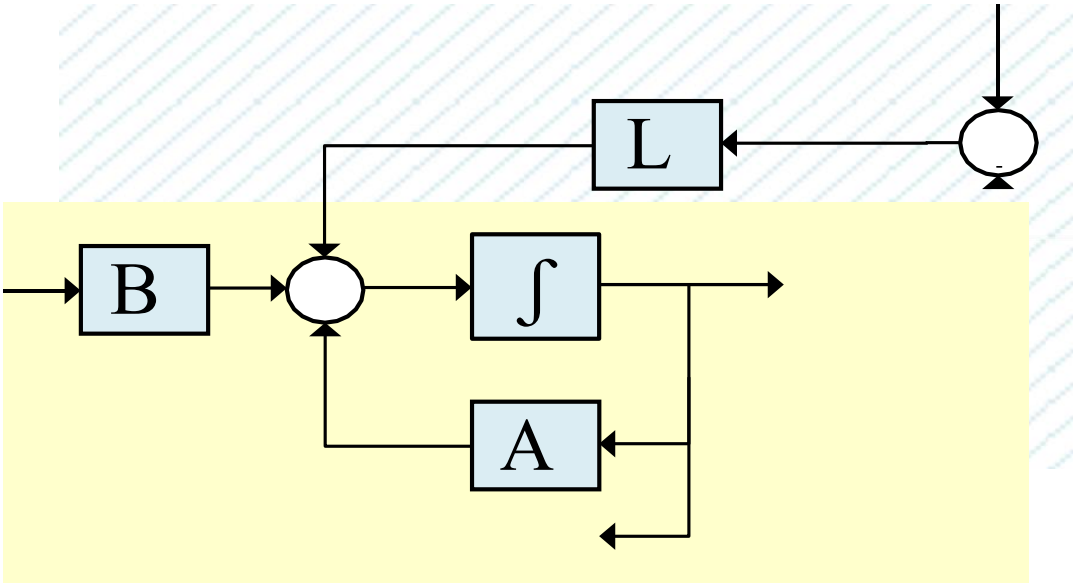

Fig. 2.6. Luenberger Observer [15]

The method indicated in [49] yields satisfactory results. Still, in a grid-connected setting, the controller's original intent was to follow a current signal. A voltage control, independent of the grid voltage, must be put into place for island microgrids. This suggests that it is necessary to handle both primary and secondary control. Additionally, harmonic sharing of power becomes an obvious issue in isolated microgrids. When it comes to isolated microgrids and nonlinear loads, a more detailed performance evaluation of Kalman filters is necessary. In [50], a detailed approach to creating a grid-connected 3-phase inverter's LQG current controller is detailed. The LQG combines a servo controller, an LQR controller, and a Kalman filter estimator. The DQ reference frame was used for the development of the whole work. The dc-link voltage and the output current were integrated during controller development. Solar panel applications that pump electricity into the grid are well-suited to this use. To maximize the power supply to the grid, the current reference on the LQG controller reduces in the event of a rapid reduction in the DC-link voltage. The most intriguing idea presented here is a Kalman filter that may increase the accuracy of estimations by utilizing the voltage of the grid as a disturbance. For the purpose of creating an input vector for a Kalman filter and obtaining precise values for the inductor current and capacitor voltage, the author combined the input vector and the grid voltage. The paper also

includes an important approach for creating an LQG controller specifically for this purpose. There are nonlinear loads that could create harmonic currents, but this study only analyzed the system by adding noise, therefore it doesn't take them into account. As seen in figure 2.7, a V-I controller was computed in [51] by multiplying the tracking errors of each state by the full-state feedback gain of a LQR controller. This controller necessitates not only every state but also every reference signal, including the current reference signals for input and output. When nonlinear loads are present, the shared harmonic power on the same bus could lead to stability issues since the reference signals for the input as well as the output were specified as pure sine waves.

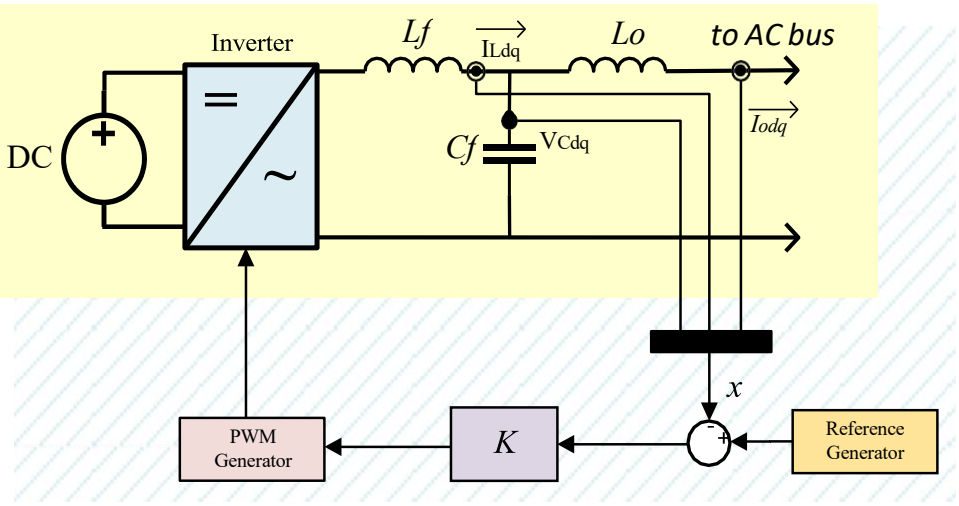

Fig. 2.7. Full State Feedback with Multiple Reference Signals [51]

A current controller for grid-connected inverters is methodically designed in [52]. Integrating the reference signal dynamics into the system to ensure faultless tracking, the author offers an optimum LQR controller on the basis of the well-known "internal model principle" (IMP) [14]. Here we offer a resonant filter realization:

$$A_c = \begin{bmatrix} 0 & -\omega_g \\ \omega_g & 0 \end{bmatrix}, B_c = \begin{bmatrix} 1 \\ 0 \end{bmatrix} \tag{2.3}$$

After resonant dynamics are added to the system, the whole thing is multiplied by the equation (2 + 2). The reference input and grid voltage are both pure sine waves, which causes certain parts of the system dynamics to go to zero. By performing this procedure, computations may be simplified and the derivative of the error in tracking can be used as a state variable in order to enhance the controllability of the system. Similarly, an amended quadratic cost equation that

relies on tracking errors and the adjusted input was used to construct an optimum LQ tracker [53]. By modifying the input as a sinusoid and applying a 2nd-order differential model that becomes 0 whenever a sinusoid is employed as a reference, the state equations are adjusted. The tracking issue is therefore transformed into a conventional LQR-solvable regulator problem. Lastly, a resonant filter is added to the states to ensure that the output is harmonically rejected and that tracking is faultless. This method yields acceptable outcomes in terms of lowering THD and issues with tracking. Nevertheless, some dynamics are overlooked due to the system's continuous time architecture. Additionally, there is no robustness analysis carried out.

An LQR-based voltage controller with frame-optimal tracking was created in [54]. To ensure flawless tracking, the author adds a resonant controller to the system operating at the nominal frequency. Also, to change the tracking issue into a regulator problem, the author applies a transformation for si-nusoid signals on the output [52]

$$\frac{X(z)}{U(z)} = \left(z - e^{j\omega T_s}\right)^{-1} T_s = \frac{T_s}{z - e^{j\omega T_s}} \tag{2.4}$$

Each filter resonates. For positive sequence input variables, this approach has infinite gain and minimizes the number of auxiliary states. This indicates that there is a positive angle between and. The resonant filters and control delay enhance the system as a whole. The controller's design restricts the optimal solutions to specific robustness parameter adjustments by utilizing a linear quadratic index in conjunction with the linear matrix inequality approach. This method produces satisfactory outcomes. However, the system is susceptible to nonlinearities due to the mathematical complexity of working with multiple variables, which also makes frequency analysis and numerical implementation challenging.

In [26], a voltage controller for parallel coupled inverters to a shared resistive load is designed utilizing an LC filter and an optimum LQR technique. To reduce tracking error, the author first adds an integrator to the voltage error signal. Next, the writer describes a

$$J(t_0) = \frac{1}{2} x^T(T) S(T) x(T) + \frac{1}{2} \int_{t_0}^{T} \left(u^T W u + x^T Q_1 x + (v_r - y)^T Q_2 (v_r - y)\right) dt \tag{2.5}$$

The input signal's weighting matrix is 1, the system states' weighting matrix is 2, and the tracking error's weighting matrix is 3. With the addition of an oscillating function based on the Laplace transform of a sine wave, the author modifies the input variable finally. Figure 2.8 shows the control diagram of the system that is being controlled. The author may achieve a state of balanced current sharing across many inverters by choosing the weighting components of 1 that correspond to the inductor current. As a result, a system for controlling the distribution of electricity is put into place. The stability of this approach, however, depends on measuring the load current. As seen in figure 2.8, this necessitates the presence of a communication channel connecting the load to the controller in the case of distant loads. Additionally, reactive power management and harmonic current sharing are not guaranteed by this control.

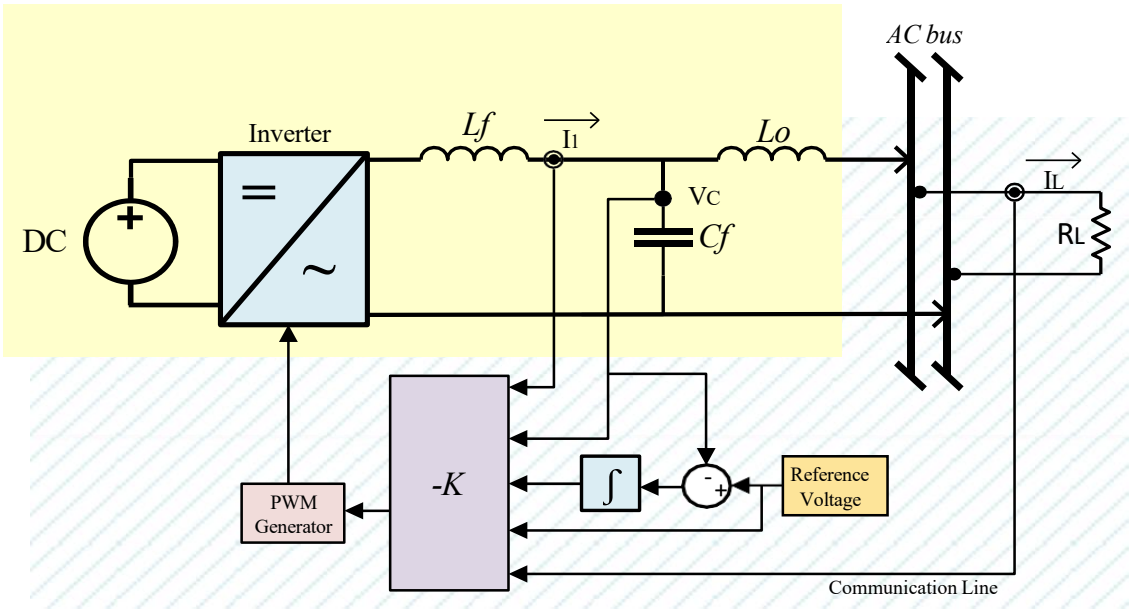

Fig. 2.8. Optimal LQR tracking with Average Load Current Sharing [26]

The performance and stability of the V-I control level are both improved by using optimal controllers. System modeling and sharing of harmonic current are not without their significant constraints, however.

2.1.3 Robust Controllers

Some closed-loop systems may have their stability margins optimized or enhanced with the use of robust controllers. Nonlinear loads, transmission problems, and imbalances are some of the microgrid uncertainties that robust controllers may help to reject.

The closed-loop system seen in figure 2.9 is often equipped with ∐ controllers that are used to provide the desired frequency response. To prevent harmonic disturbances induced by nonlinear loads and improve tracking error, ∐ controllers are used in microgrid v-i control. The paper [56] suggests a reliable controller that utilizes ← control. One of the key concerns impacting grid-connected inverters' stability is the uncertainty in transmission line impedances, according to the author. The author shows that inverter stability is severely impacted by increasing transmission inductance and decreasing line resistance using a standard pole-zero map analysis. To assess for robustness limits, this fluctuation in line impedances is modeled as a linear fractional transformation system (LFT). In order to distinguish between the system ō( ), the controller (), and disturbances, the LFT shown in figure 2.9 is used. Assigning signals to input and output vectors, respectively, is the case. The reference signal is denoted by () while the measurement signal is represented by (). The uncertainty matrix is connected via the auxiliary signals denoted by signals () and ().

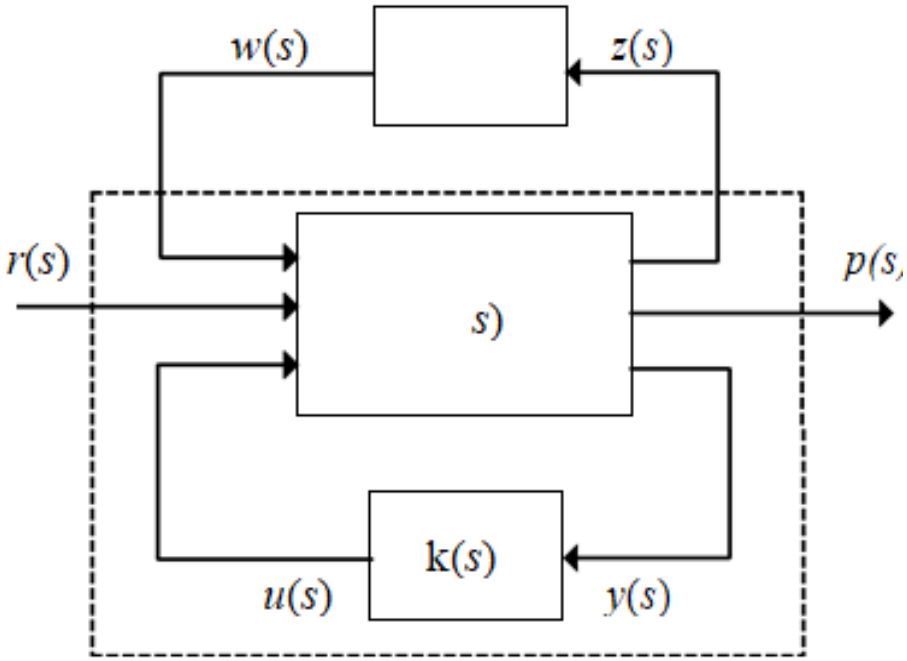

Fig. 2.9. Linear fractional transformation (LFT) of a closed-loop system [18]

For the ∐ controller to work, weighting functions for the sensitivity () and co-sensitivity () transfer functions, which represent measurement and process uncertainties, correspondingly, must be defined. In order to reduce uncertainty due to transmission line fluctuations, the weighting functions were constructed to follow the reference signal. A resilient controller that maintains system stability in the face of fluctuations in line impedance was synthesized using the mixsyn matlab function [57] after the weighting functions were established. Regardless of the fact that this method fails to account for harmonic distortion due to the controller's design for grid-connected inverters; nevertheless, it does provide an acceptable tracking error and disturbance rejection [56]. For grid-connected inverters using LCL filters, a reliable current control scheme is detailed in [58]. Here, the author takes the line inductance extremes as the basis for a polytopic model of the plant. The polytopic model incorporates variations on certain plant characteristics into the states. Furthermore, in order to ensure the regulator's robust performance, this method employs a linear matrix inequality (LMI) with an enhanced constraint of ∐ [59]. A resonant filter at the nominal frequency is represented by the enhanced states that the controller generates as a state feedback gain. This controller is not meant to guarantee an increase in power quality and total harmonic distortion (THD) under nonlinear loads, even if it takes into account variations on the plant in isolated mode. Performance under specific changes may be assessed using the ∞ idea. The synthesized structure. A single-phase ups inverter controller was developed in [60]. A voltage-controlled inverter's robustness, performance, and tracking error were assessed using a -synthesis analysis in this study. Defined by is the -value, also known as the structured singleton value.

$$\mu_{\delta}(M) := \frac{1}{min\{\bar{\sigma}(\delta):\delta\in\delta,\det(I-M\delta)=0\}} \tag{2.6}$$

The plant M's feedback loop. To achieve tracking performance and stability robustness simultaneously

$$\mu_{\delta}(\hat{\sigma}(j\omega)) < 1; \forall\omega \geq 0 \tag{2.7}$$

This is where z represents the transformation of the plant transfer function, which has to be connected with the planned controller and kept apart from uncertainties. Figure 2.9 shows the LFT of the framework analyzed controlled system with uncertainties. By using the D-K iteration algorithm [61], the author suggests a controller that can accomplish an open-loop function while

still meeting the control goals, even when inductances, capacitances, and line impedances vary. In order to evaluate how well a v-i controller works, this study establishes a standard.

With predicted uncertainty for use in microgrid applications. To top it all off, the -framework's performance constraints may be met by creating a controller utilizing the D-K iteration algorithm.

A grid-connected 3-phase inverter's current controller is designed utilizing the -synthesis architecture in [62]. By utilizing an LFT and the DKIT MATLAB function, the -controller is designed to eliminate uncertainty related to components and temporal delays [57]. Users are able to see the changes in the frequency response of the system thanks to the LFT, which parameter sizes the desired uncertainty. The last step is to stabilize the system under specified uncertainties and achieve the required performance using a loop-shaping technique similar to ∞ synthesis using a set of weighting functions 1() and 2(). To ensure tracking error at the fundamental frequency and reject harmonics 1, 3, 5, and 7, this study used a transfer function from reference to the tracking error (). The product of resonant filters is used to reject harmonics, as illustrated in equation (2.8) where is the grid angular frequency and denotes the harmonic number.

$$W_1(s) = \frac{4000}{s(0.0001s+1)} \prod_{k=1,3,5,7} \frac{s^2+1000s+(k\omega_g)^2}{s^2+s+(k\omega_g)^2} \tag{2.8}$$

This method yields acceptable outcomes. However, converters that are linked to the grid and do not experience frequency or amplitude fluctuations are the only ones for which the controller is valid. Because of its resistance to changes in nominal frequency brought about by droop control techniques, the controller should not be employed as a main control in microgrid applications.

The current controlling of a 3-phase connected to the grid inverter is implemented using a linear matrix inequalities design technique [63]. A theorem is defined by the author using the polytopic system robustness inequality [64]. The dynamics of a polytopic system may take on a limited range of values when one or more factors are varied. By calculating the lowest and maximum variations in line inductance, the author proved that there are enough variables to be stable. A thorough approach to controller design under parameter fluctuations is shown in the work of [63]. Furthermore, by combining all the models into a unified state-space model, the author

created a series of discrete resonant controllers to govern the supply of harmonic power. We need to do further research on isolated microgrids to better understand their stability.

This method yields acceptable outcomes. However, converters that are linked to the grid and do not experience frequency or amplitude fluctuations are the only ones for which the controller is valid. Because of its resistance to changes in nominal frequency brought about by droop control techniques, the controller should not be employed as a main control in microgrid applications.
In response to changes in grid voltage and frequency. This method may also be useful for developing a main controller that makes use of state space techniques.

Finally, an alternative method to robust control is presented in [65], which uses a linear sliding mode controller to ensure that island microgrids are resilient against current disturbances. It is not possible to build the sliding mode controllers with current disturbances in mind for any one of the sliding modes. To further enhance the thd and tracking error, an adaptive filtering strategy is used. With a minimal tracking error, small THD, and steady active power sharing across DGs, the experimental findings demonstrate an appropriate response. The primary controller does not take into account any of the dynamics of the v-i control, and it is worth noting that the two controllers were developed independently. Potentially impacted by this split include stability, robustness, and performance

To study how uncertainties affect the stability and performance of microgrids, robust controllers for isolated microgrids are appropriate. To assure power quality under various disturbances and flawless tracking in v-i control, strong controllers may be utilized. Important metrics on stability margins may also be provided by robust controllers. It is possible to assess various control parameters by combining these measurements with other control approaches. However, robust controllers aren't often used since their mathematical analyses might be complicated and, in some instances, they're only suitable for linear systems familiarity with stability

2.1.4 V-I Control Summary

The 26 papers that made up this literature review all dealt with V-I control approaches as they pertain to microgrids. Table 1 provides an overview of these publications. Eleven of these articles are published in proceedings from conferences, while fifteen appear in journals or IEEE transactions. Only a few of the articles cited are more than a decade old; all of the fundamental

papers that were considered were published between 2004 and 2006. Figure 2.10 provides a summary of this.

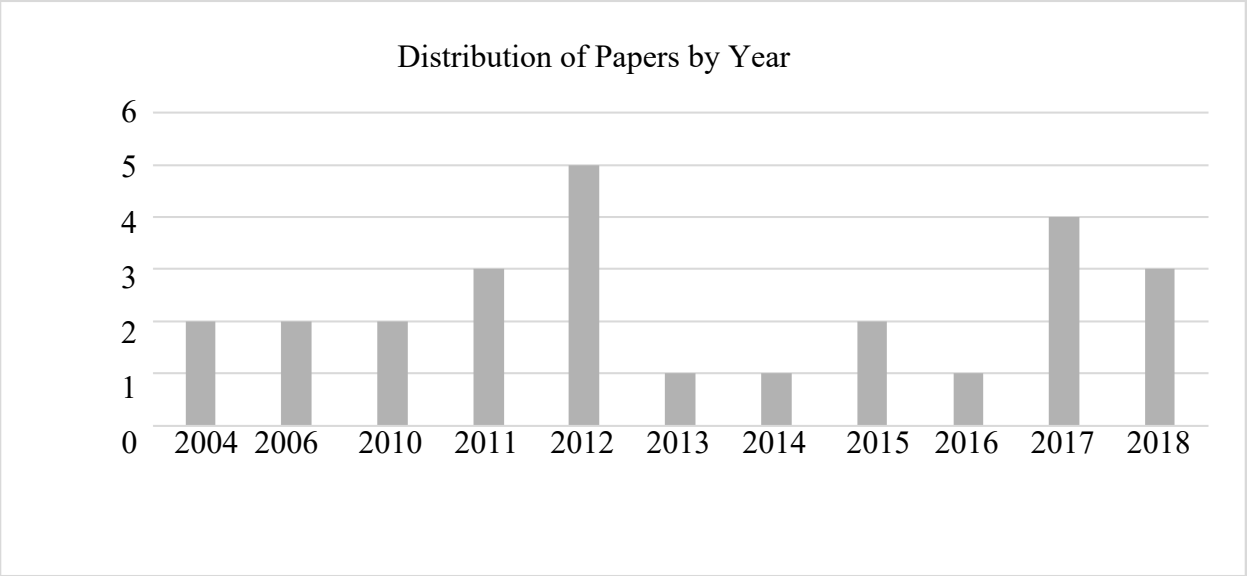

Fig. 2.10. Distribution of Reviewed V-I Control Papers by year

Because of the simplicity of implementation with the main control level, the majority of articles in microgrid V-I control concern conventional pi/pr controllers. The assumption that v-i control is already in place and that its dynamics will not impact other control levels is why many papers on primary or secondary control levels exclude it.

In general, LQR and LQG controllers, which augment the plant states with a PI/PR controller and maximize their gains, are the most representative of optimal control schemes. Due to its infinite gain nature under nominal frequency, PI/PR controllers have a profound effect on robustness margins whether used for optimum control or when added to plants [18]. A parameter representing stability or performance margins is defined by robust control procedures using LMI and synthesis. When looking to assess stability, robustness, and performance, it is usual to see optimum control approaches paired with robust control analysis theory. Enhancing stability, compensating for harmonics under nonlinear loads, and making V-I controls more resilient to plant changes and line imbalances are among the most pressing issues in this field.

TABLE 2.1 SUMMARY OF "REVIEWED V-I CONTROL METHODS FOR MICROGRIDS

Ref.	Year	Type of Publication	Citations (gscholar)	Controller	Frame	Control Variable	Mode
[26]	2006	Journal	77	Optimal-LQR	3 −	Voltage	Islanded
[36]	2013	Journal	398	Classical-PR	3 −	Voltage	Islanded
[66]	2017	Journal	41	Classical- PR	3 −	Voltage	Islanded
[38]	2017	Conference	Na	Classical-PI	3 −	Voltage	Islanded
[43]	2010	Journal	229	Classical- PI	3 −	Current	Grid connected
[44]	2012	Journal	131	Classical-PR	3 −	Current	Grid connected
[45]	2017	Conference	Na	Classical- PR	1	Voltage	Islanded
[46]	2004	Journal	294	Optimal- LQR	3 −	Voltage	Islanded
[47]	2011	Conference	9	Optimal- LQR	3 −	Current	Grid connected
[48]	2012	Conference	14	Optimal- LQR	3 −	Current	Grid connected
[49]	2015	Conference	11	Optimal-LQG	3 −	Current	Grid connected
[50]	2012	Journal	60	Optimal- LQG	3 −	Current	Grid connected
[51]	2010	Journal	492	Optimal- LQG	3 −	Voltage	Islanded
[67]	2015	Conference	Na	Optimal- LQG	3 −	Voltage	Islanded
[52]	2018	Journal	5	Optimal- LQR	1	Current	Grid connected
[53]	2011	Conference	10	Optimal- LQR	1	Voltage	Islanded
[54]	2018	Conference	2	Optimal- LQR	3 −	Voltage	Islanded
[55]	2018	Journal	Na	Optimal- LQR	3 −	Voltage	Islanded
[56]	2011	Journal	299	Robust- ∞	3 −	Current	Grid connected
[58]	2012	Conference	17	Robust-LMI	1	Current	Grid connected
[60]	2004	Conference	43	Robust- ∞	1	Voltage	Islanded
[62]	2016	Conference	3	Robust-	1	Current	Grid connected
[63]	2014	Journal	56	Robust-	1	Current	Grid connected
[65]	2012	Journal	74	Robust-sliding Mode	3 −	Voltage	Islanded

2.2 Power Sharing Droop Control (Primary Control)

The main control level is responsible for regulating the power-sharing among the main grid, loads, and generators. It is common practice to classify shared authority as either active or reactive. The transmission line's characteristics greatly affect the degree to which active and reactive power may be shared. In addition, whether a microgrid is islanding or linked to the grid has a significant impact on the power-sharing approach. Primary control is a well-liked area of study because of these qualities. There has been a plethora of survey articles published in this field [22], [28], [68], [69]. Improvements in stability, transient responsiveness, active/reactive power decoupling, virtual impedance management, harmonic power sharing, and transitioning between island and grid-connected modes are some of the main contributions to primary control.

To ensure fair distribution of electricity, communication-based main controllers connect several generators. Reliability and resilience to unexpected changes in the microgrid may be impacted by these communication channels. As a non-communicated alternative, droop control approaches arise to handle this issue by making all generators act as synchronous generators. So, until the frequency is uniform across the microgrid, all inverters will lower their nominal frequency in response to the power demand. It is possible to determine the rate of frequency change in relation to the maximum rated power of every generator in order to achieve power-generating balance.

This section provides an overview of the key advancements in microgrid droop control. To begin, we will take a look back at the much iteration of traditional droop control techniques. Following this, we provide a few strategies for optimum droop techniques.

2.2.1 Classical Droop Control Methods

Power distribution among generators, loads, and the main grid is controlled at the main control level. Both active and reactive forms of shared authority are often used. How much active and reactive power may be exchanged is heavily dependent on the characteristics of the transmission line. A further factor that greatly affects the power-sharing strategy is whether a microgrid is islanding or connected to the grid. These features make primary control a popular field of research. Multiple survey papers have been published on this topic [22], [28], [68], [69]. Significant advancements have been made in primary control, including stability, transient

responsiveness, active/reactive power decoupling, harmonic power sharing, virtual impedance management, and the ability to move between island and grid-connected modes.

As mentioned in section 1.1.2.2, conventional droop control techniques are utilized to distribute power output proportionally over the microgrid in the absence of communication links. Shared power may be either active or reactive. Consumption of electricity at load is one way to quantify active power. On the contrary, reactive power is linked to the transfer of energy from generators to end users. The notion of reactive and active power sharing was established by akagi et al. In 1984 [70]. This paper presents a method for effectively reducing transmission line reactive power utilizing a 3-phase inverter. Furthermore, the author stresses that reactive power is not supplied to the load but is instead continuously transferred between generators and loads. To reduce the grid's reactive power and fix the power factor, the compensator measures active and reactive power and then determines the current needed to provide the additive inverse of reactive power. The formula for the output current required reducing grid reactive power, as shown in equation (2.9), may be expressed as follows:

$$\begin{bmatrix} i_\alpha \\ i_\beta \end{bmatrix} = \begin{bmatrix} v_\alpha & v_\beta \\ -v_\beta & v_\alpha \end{bmatrix}^{-1} \begin{bmatrix} 0 \\ -Q \end{bmatrix} \tag{2.9}$$

Injecting the control currents into the grid reduces reactive power's fundamental and harmonic components. Microgrid research on active and reactive power sharing has built on the work of akagi et al.

In [39], one of the first methods for controlling droop was created. Figure 2.10 shows the author's assumption of an inductive transmission line while sharing a load in a single-phase microgrid.

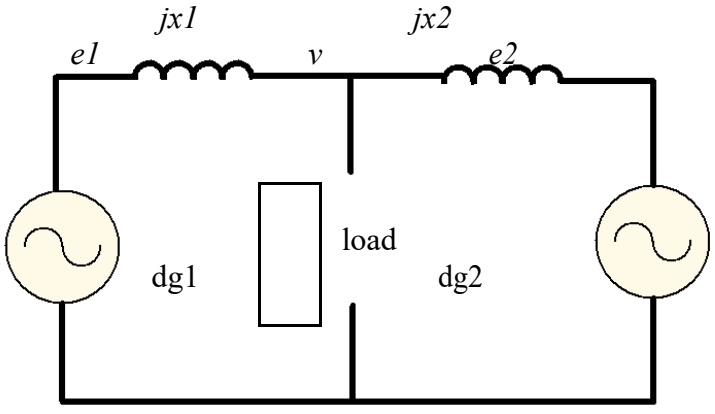

Fig. 2.10. Two generators sharing a load through a purely inductive transmission line [39]

The droop control idea is expanded in this study to single-phase inverters that don't include the DQ transformation. The designer is therefore compelled to operate entirely inside an oscillating framework. The shared active and reactive power of every generator is determined by (2.10) and (2.11) in a manner similar to that of expressions in (26) and (27)

$$P = \frac{EV}{X}\sin\delta \tag{2.10}$$

$$Q = \frac{V(E\cos\delta - V)}{X} \tag{2.11}$$

When the phase shift is minor, cos is around 1 and sin is about. As a result, the amplitude of the generator's voltage is precisely proportional to the reactive power and the phase shift is directly proportional to the active power.

To control the proportionate share of active & reactive power in relation to amplitude & phase shift, one may utilize the droop functions provided in (28) and (29) as stated in equations (2.12) and (2.13). When choosing the droop coefficients, be sure to use these expressions to ensure proportionate load sharing:

$$m_1 S_1 = m_2 S_2 = m_3 S_3 \ldots = m_k S_k \tag{2.12}$$

$$n_1 S_1 = n_2 S_2 = n_3 S_3 \ldots = n_k S_k \tag{2.13}$$

The rated apparent power in VA is represented by, and the active & reactive droop coefficients for the k-th generator. Also presented in [2.14] is the distortion power, which the author suggests has some relationship to perceived power via the following expression:

$$S^2 = P^2 + Q^2 + D^2 = E_1^2 I_1^2 \cos^2\varphi_1 + E_1^2 I_1^2 \sin^2\varphi_1 + E_1^2 \sum_k I_k^2 \tag{2.14}$$

There are nonlinear loads, and the harmonic current that results from them is going somewhere. Figure 2.11 shows the author's proposal to include a multiplicative block into the v-i control loop in order to distribute distortion power. This block would adjust the bandwidth in response to the presence of nonlinear currents.

The findings indicate that the distribution of active power is proportionate. However, due to the fact that line impedances are not fully inductive and vary on each generator, reactive power is not proportionate. The creation of droop controllers for use in microgrids is laid forth in this study. More research is needed to determine stability in a microgrid with primary control, though.

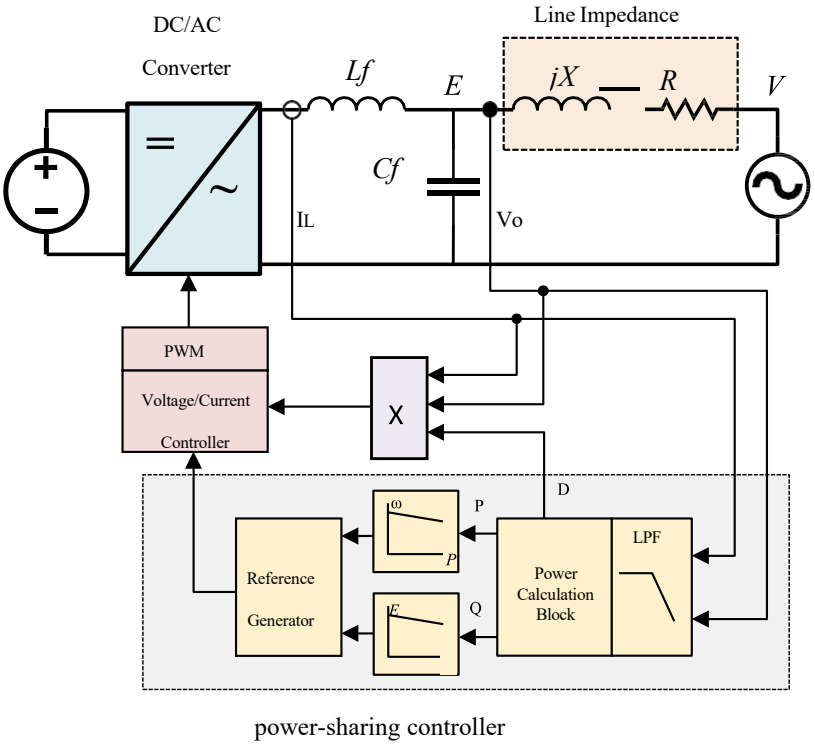

Fig. 2.11. Distortion Power-Sharing with Multiplicative Component [39]

In [71], the author builds on the work in [46] and suggests a power-sharing control technique that combines the conventional droop and average power control methods. The combination of these two factors makes the system more robust against transient changes in voltage and current. Also, as illustrated in [46], the author suggests a way to control harmonic power droop by measuring the harmonic current and adjusting the resonant filter poles accordingly. In order to carry out the basic power-sharing control, this study relies on low-band communication and does not stress the consequences of including a harmonic power droop control. Coelho described a 1999 study of the stability of tiny signals for a single-phase droop-regulated inverter coupled to a rigid AC source [40]. As seen in Figure, this approach involves connecting the inverter to the stiff AC source via a resistive-inductive load. Presuming that to get the nominal values of 0 and 0, one may evaluate each of the powers to 0, as the stiff ac source amplitude is 120 in equations (2.15). In order to linearize around the point p, we may use the following formula:

$$f(x) \approx f(p) + \nabla f|_p \cdot (x - p) \tag{2.15}$$

One may find the linearized expressions for p, q, and e:

$$\delta Q = k_{qe}\delta E + k_{qd}\delta\delta \tag{2.16}$$

$$\delta\omega = -m\delta P \tag{2.17}$$

$$\delta E = -n\delta Q \tag{2.18}$$

Where $k_{pe}, k_{pd}, k_{qe},$ and k_{qd} and are constants resulting from evaluating the linearization function on the operating point p [40]. Using a low-pass filter with cut-off frequency, merging equations (2.16) to (2.18), and indicating that δ ( ) = ( ) one may define the following system:

$$\delta\delta(s) = -\frac{k_p\omega_f}{s(s+\omega_f)}\left(k_{pe}\delta E(s) + k_{pd}\delta\delta(s)\right) \tag{2.19}$$

$$\delta E(s) = -\frac{k_v\omega_f}{s+\omega_f}\left(k_{qe}\delta E(s) + k_{qd}\delta\delta(s)\right). \tag{2.20}$$

To find the stability of a droop-regulated inverter coupled to a stiff AC source, the analysis given in [40] is used. To do this, we use equations (2.19) and (2.20) to create eigenvalues of the system, which we then examine. Another thing to note is that the inverter frequency and voltage amplitude will converge to zero divergence from the linearization point p for appropriate values of and.

$$\delta\dot{x} = A \cdot \delta x \tag{2.21}$$

Coelho followed up with a comparable small-signal stability study for power sharing between two parallel linked inverters in 2000 [31]. An all-inclusive linearized microgrid state-space model in the dq frame is created in this study. The nominal voltage in the dq frame for the i-th inverter, which is in phase and quadrature, and the frequency of each inverter is represented by δ. Matrixes that rely on droop coefficients, nominal voltages, and nominal current vectors make up the state For a comprehensive explanation of these matrices, see [31]. the whole dq-frame linearized microgrid is created. The whole system is detailed in equation (52): Coelho described

a 1999 study of the stability of tiny signals for a single-phase droop-regulated inverter coupled to a rigid AC source [40]. As seen in Figure 15, this approach involves connecting the inverter to the stiff AC source via a resistive-inductive load. Presuming that to get the nominal values of 0 and 0, one may evaluate each of the powers to 0, as the stiff ac source amplitude is 120 in equations (26) and (27). In order to linearize around point p, we may use the following formula: if we know the matrix value, we can compute the eigenvalues and use them to find the system's stability and transient responsiveness.

Additionally, it is shown that, given a stable matrix, the frequency values will exhibit a transient response up to the point when the target values of p and q are reached, at which point the frequencies zero out. A secondary control loop is necessary to restore the nominal frequency in both inverters at the same time if, after the transient response, both frequencies exhibit a little divergence from the normal frequency.

The work of Coelho offers a practical approach to evaluating microgrid stability using the droop technique as the main control mechanism. This study, however, cannot disentangle the droop controller from the system and does not account for the v-i control loop's effects.

Using small-signal analysis, a whole microgrid was modeled in [41]. To examine the impact on microgrid stability, V-I, and power-sharing control settings were combined. An inverter model, a network model, and a load model were all used to represent the whole system.
The inverter model took into account the LCL output filter dynamics, as well as the V-I and main droop controls. An m-node network with n resistive-inductive lines was taken into account in the model of the network.
The load model accounted for a resistive-inductive load. The number of generators, network connectivity, and loads determine how each of these models may be integrated into the entire microgrid model.

The root locus approach was used to examine the whole model. The arrangement of the microgrid's eigenvalues was found to have three distinct clusters. The inverter dynamics-related first cluster stood for the fastest cluster. The location of the eigenvalues in this cluster is somewhat far from the imaginary axis. These eigenvalues are directly affected by adjusting the LCL filter values. The eigenvalues produced by the V-I controllers were represented by the second cluster, which was situated somewhat to the right of the first cluster. The proportional

and integral/resonant constants of these controllers had an immediate impact on these eigenvalues. In close proximity to the imaginary vertical axis lies the third and most crucial cluster. Line impedances and droop control constants have a direct impact on these eigenvalues. The microgrid will lose stability when the eigenvalues shift to the positive semi-half plane due to an increase in the droop constants. If we know the matrix value, we can compute the eigenvalues and use them to find the system's stability and transient responsiveness. Additionally, it is shown that, given a stable matrix, the frequency values will exhibit a transient response up to the point when the target values of p and q are reached, at which point the frequencies zero out. A secondary control loop is necessary to restore the nominal frequency in both inverters at the same time if, after the transient response, both frequencies exhibit a little divergence from the normal frequency. The work of Coelho offers a practical approach to evaluating microgrid stability using the droop technique as the main control mechanism. This study, however, cannot disentangle the droop controller from the system and does not account for the V-I control loop's effects.

Using small-signal analysis, a whole microgrid was modeled in [41]. To examine the impact on microgrid stability, V-I, and power-sharing control settings were combined. An inverter model, a network model, and a load model were all used to represent the whole system.
The inverter model took into account the LCL output filter dynamics, as well as the V-I and main droop controls. An m-node network with n resistive-inductive lines was taken into account in the model of the network. The load model accounted for a resistive-inductive load.
The number of generators, network connectivity, and loads determine how each of these models may be integrated into the entire microgrid model.

This method uses tiny signal analysis to provide important details on microgrid stability. Having said that, the control topology and control constants are foundational to the whole microgrid paradigm. The typical approach to modeling a dynamic system is with the goal of making it easy to link with a control strategy. Nevertheless, this method incorporates the control parameters into the microgrid model, thus modifying them directly impacts the analysis. Additionally, as the microgrid model can only be constructed with the closed-loop system in mind, no formal stability study can be conducted from an open-loop viewpoint.

The use of droop controllers in microgrids is the subject of yet another significant body of studies.[72].the author classifies microgrid stability as either transient, small signal or voltage stability. The V-I and primary feedback controllers have the most impact on the small signal stability. The control settings determine the system's transient response and how poles are allocated. The majority of the minor signal stability problems in isolated microgrids are caused by feedback controllers using decentralized control approaches like droop control [72]. Optimal and resilient control methods, additional control loops, coordinated control, and stabilizers like flywheels may all help with this stability. Because there is no link to a rigid grid in island mode, fluctuations in frequency and voltage amplitude may have a significant impact on transient stability. Nonlinear system analysis and lyapunov function approaches are used to study transient stability [73]. Additionally, energy storage and load-shedding techniques may be used to address transient stability by sustaining the whole system in the event of a sudden power outage. Lastly, induction motor connections or reactive load-sharing issues might disrupt voltage stability. To fix voltage stability, reactive power may be injected into the microgrid to make up for the abrupt decrease in voltage.

In [74], a dynamic phasor modeling (dpm) of the main droop control of a microgrid is created, which is another method for stability analysis in droop controllers. The Fourier series is the source of the DPM idea:

$$f(t) = \sum_{k=-\infty}^{\infty} x_K(t) e^{jk} \omega_s \tau \tag{2.22}$$

Where is the fundamental frequency and ( ) represents the k-th phasor at time t defined by:

$$x_k(t) = \frac{1}{T} \int_{t-T}^{t} x(\tau) e_s^{jk\omega_s \tau} d\tau = \langle x \rangle_k(t) \tag{2.23}$$

Where ⟨ ⟩ ( ) is the average k-th phasor over a time period t. The most important property of dynamic phasors is their time derivative, which is given by:

$$\frac{dX_k(t)}{dt} = \left\langle \frac{dx}{dt} \right\rangle_k (t) - jk\omega_s x_k(t) \tag{2.24}$$

As the angular frequency at which the device operates. The word does not exist in traditional circuit theory, as you may have noticed. Compared to the traditional tiny signal analysis shown in [31], this factor improves the inverter circuit's dpm. We compared the new active and reactive power model we devised to two existing models, one for whole orders and one for tiny signals, to see how accurate it was. In terms of eigenvalue location and transient response, the results demonstrate sufficient modeling. More so than in the past, this model also performed better when tested with a virtual-frame droop control. However the v-i control loop isn't accounted for in this model, so it's hard to figure out how the real and imaginary parts of power, current, and impedance are coupled. When examining transient responses in a whole microgrid, this approach may provide better results.

The authors of [75] devised a droop controller that uses additional phase shift control action and tiny signal analysis to enhance transient responsiveness. The power-sharing controller now has more leeway to tweak the closed-loop poles thanks to the supplementary phase control action. Here is the new droop controller:

$$\delta\delta = \left(-\frac{k_p}{s} - k_d\right)\delta P \tag{2.25}$$

One novel aspect of this method is the development of a droop controller using a small-signal model. When combined with appropriate control procedures, this analysis of tiny signals may enhance transient responsiveness and ensure resilience. Transient reaction has been shown to improve. Be advised that this implementation is only applicable to grid-connected inverters, as long as the frequency and voltage remain within the operational point.

For active power sharing, a supplemental droop control loop is suggested in [51]. This additional control loop is designed to enhance stability that is brought about by choosing large droop gains. A new block that computed the active power's oscillatory response was introduced by the authors to accomplish this. Afterward, a series of lead-lag controllers were used to guarantee a dampened reaction even when droop gains were set to high levels. A stability analysis was conducted on the complete system, including the v-i and main control. The author accomplished this by modeling the whole system in a DQ frame. In the same linear state system, this enables the analysis of both the v-i control and the main control. Because of its high-bandwidth behavior, the author claims

that the v-i control's dynamics have no effect on stability. The eigenvalues are also changed to point away from the imaginary axis by adding the additional control loop. The stability may be compromised when utilizing higher control levels, such as secondary or tertiary control, due to the non-minimum phase zeros generated by inserting the supplemental control loop. Although the author does the study using an already-designed internal V-I controller, they do not provide a full linear state system that might be used to create an integrated PQVI controller.

The steady-state error and fluctuating transient response are two infamous problems with traditional droop controllers that use proportional droop coefficients [6], [22]. In addition, the stability of the v-i control loop may be impacted by transient oscillations, which provide a challenge to steady-state accuracy. Another sign of unwanted energy transfer between inverters is transient oscillations. This issue may be resolved by applying a PID control strategy to the droop controller in accordance with the following formula [76]:

$$\delta = -m\int_{-\infty}^{t} P d\tau - m_p P - m_d \frac{dP}{dt} \tag{2.26}$$

$$E = E^* - nQ - n_d \frac{dQ}{dt} \tag{2.27}$$

$$\omega = -mP \tag{2.28}$$

Which is equal to the classic proportional frequency droop control law shown in [39]. Results from this approach show that transient response is improved, and steady-state error is reduced. However, this approach requires high precision with a trial and error method to find a suitable set of droop gains. Furthermore, there is no robustness analysis performed for these types of controllers. The integral component indicates the presence of a pole at the origin, which may represent small gain and phase margins.

Similarly, a complete microgrid hierarchical controller in a stationary reference frame was presented in [36]. In this work, a PR V-I controller was integrated with a pi droop controller and a secondary PI controller. The pi droop controller shows that power is shared proportionally according to the power ratings of each generator. However, no stability analysis was performed

and the control gains for each level were calculated heuristically, which does not guarantee optimal performance.

Another example of a complete microgrid control system is shown in [77], where a fully distributed control approach for AC microgrids is presented. The author integrates primary, secondary, and tertiary control to share power, restore grid frequency, and exchange energy with other microgrids respectively. To ensure stability, the author sets some base rules for each inverter's time constant and maximum frequency values. Additionally, the tertiary control is based on a nonlinear function that evaluates the actual costs of selling energy and adjusts the frequency to sell or buy energy accordingly.

One of the main challenges in primary control is the effect of line impedance in power dynamics. As shown in Fig. 2.12, the output current vector varies with the line impedance angle and the phase shift between generators. Thus, active and reactive power expressions vary as well.

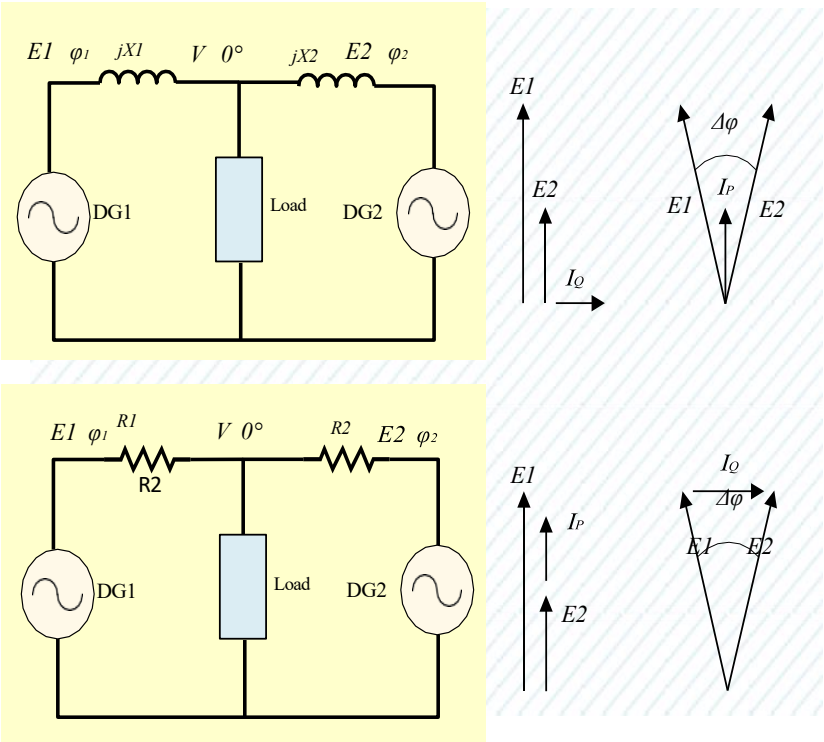

Fig. 2.12. Effect of Line Impedance in Output Current [78]

As shown mathematically in (2.29), the active and reactive power changes in relation to the output impedance angle, the phase difference between the inverter and the ac bus, and the amplitude of the inverter voltage e.

$$P = \frac{EV}{Z}\cos(\theta - \varphi) - \frac{V^2}{Z}\cos\theta$$
$$Q = \frac{EV}{Z}\sin(\theta - \varphi) - \frac{V^2}{Z}\sin\theta \quad (2.29)$$

Resistive transmission lines are typical in microgrids since the distances between generators are minimal. Since traditional droop controllers assume a very inductive transmission line, this could compromise the precision of power sharing. As a function of the voltage reference and the output current, the regulated inverter's output voltage may be expressed as follows [78]:

$$V_c = G(s)V_{\text{ref}} + Z_o(s)i_o(s) \quad (2.30)$$

The controlled inverter's output impedance may be understood as (). If you want to know how droop controllers share power, you need to grasp this idea. As seen in Figure 2.13, guerrero et al. [78] suggested a virtual impedance loop to mitigate the impact of inaccurate transmission line impedances

$$V_c = G(s)V_{ref} + Z_o(s)i_o(s) \quad (2.31)$$

To Get the Output Of The Droop Controller Without The Virtual Impedance (), Just Follow These Steps

$$V_{ref} = V_o^* - Z_D(s)i_o(s) \quad (2.32)$$

The goal is to achieve a phase shift of 90 degrees and an inductive frequency response of 20 DB/Dec, thus the output impedance is adjusted accordingly. The standard method for compensating harmonic power sharing involves selecting a first-order high-pass filter. By adjusting the inverter's output impedance, Guerrero et al. Demonstrate remarkable success. Under the operating frequency range, the output impedance is strongly inductive, allowing for the implementation of a droop controller.

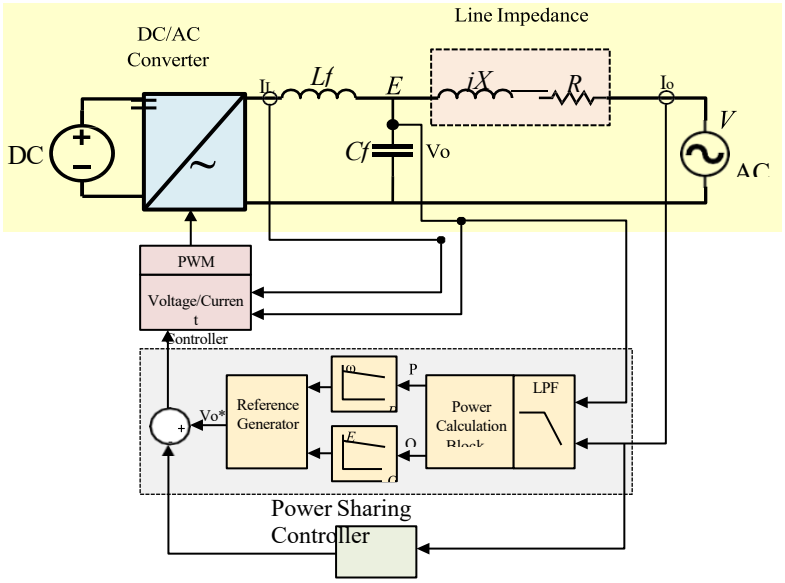

Fig. 2.13. Virtual impedance loop proposed by Guerrero et al. [78]

Improved harmonic current sharing and reduced current spikes caused by abrupt changes in load are two goals of virtual impedance design. A technique for controlling harmonic power sharing is described in [79]. The foundation of this approach is "the relationship between the amplitude of the voltage at the AC bus and the reduction of the output impedance at harmonic *h*, which is achieved by the regulation of harmonic power droop (h − droop) and negative virtual harmonic impedance. Each DG calculates its estimated available power using the rated apparent power, active power, and reactive power shown in (44). This allows for a proportionate sharing of harmonic power. The amount of power that can be transferred via harmonic current is shown by this estimate. Each harmonic's virtual output impedance is decreased in proportion to the power capability of the generators, using this available power. By allocating harmonic current among DGs in accordance with the apparent power capacity that is available, the simulation results demonstrate that the harmonic power-sharing control approach is" successful. Nevertheless, in order to ensure effective and dependable functioning, a stability study has to be conducted.

In [66], a hierarchical framework for three-phase island microgrids is given, using a similar method. Using virtual impedances, this structure employs a number of harmonic current control loops. To counteract the positive and negative sequence currents brought on by imbalances in the transmission lines, this structure also makes use of several virtual impedance loops. The analysis of power-dampening behavior induced by secondary control is completed by developing a small signal stability model that integrates main and secondary control loops. The use of pi/pr

controllers for all of the control loop development undermines their resilience and their ability to handle transient behavior appropriately.

Changing the output impedance to be completely resistive is another option. To manage power sharing in isolated microgrids, the authors of [80] use a resistive virtual impedance approach. The author avoids the problems associated with inductive output impedance by simulating resistive virtual impedance using a proportional coefficient at the output voltage. Take note that the droop-boost control →, − is used instead of the usual droop control −, − when the output impedance is mostly resistive. It follows that voltage deviations have a direct proportional relationship with active power and phase deviations have an inverse relationship with reactive power. To account for voltage fluctuations in a steady state, the output voltage has an extra proportional droop coefficient. In a proportional relationship between the generator voltage deviation and the grid voltage, this extra coefficient controls the output amplitude. By using this approach, the model becomes resistant to changes in impedance and measurement mistakes, and the controller becomes independent of the output impedance. This is one of the major problems with the approach requires very accurate measurements of the grid voltage to ensure reliability.
There are certain benefits to using classical droop control techniques instead of power-sharing control tactics based on communication. Unfortunately, there is no systematic process included in the design of these controllers to ensure microgrid stability and performance. Heuristics are utilized to find most of the gains or coefficients in conventional droop controllers, and the stability is evaluated by looking at where the eigenvalues are in a pole-zero diagram. Classical droop techniques also presume a very inductive output impedance. Several variants of a virtual impedance loop that alter the frequency response to exhibit inductive behavior are suggested as solutions to this issue. Nevertheless, the inclusion of this virtual impedance as a feedforward element has the potential to impact robustness and stability.

2.2.2 Optimal Droop Control Methods

By determining the ideal values of droop gain for active and reactive power, optimum droop control systems strive to provide the best performance and stability margins. Optimal droop controllers were the subject of only a small number of publications in this literature review. A full mathematical model of the system is required, which is the major drawback of these controllers. Altering the reference signal's frequency and amplitude couples the main and V-I controllers in hierarchical control. Because of this nonlinear coupling, the inverter cannot be described as a system in linear state space. Fig. 15 shows the power calculation block with a low-

pass filter installed to separate the primary and V-I controls. This is likely the major reason for this separation. The information in references [31], [40], [41], [51], [72], [74], and [75] is helpful for building a mathematical model of the inverter linked to a microgrid. The problem is that these studies use a single state-space model for both controller and inverter dynamics, which makes it hard to articulate a potentially optimal control rule.

An islanded microgrid's proportional frequency and voltage droop gains stability margins are examined by a small signal analysis employing the dynamic phasors technique [81]. An oscillating system's stability analysis and transient response may be better understood with the help of dynamic phasor modeling. Here, two inverters were shown, each linked to a resistive-inductive line. After that, the active and reactive power transfer functions were subjected to a closed-loop analysis. In order to achieve the maximum potential range of proportional droop, the author used partial derivatives to determine the ideal values of the constants and components.

Unchanging parameters. When it comes to finding ideal ranges, the results demonstrate that the model is spot on. To provide state-feedback control, this approach may be used for state-space models. PSO with a different performance index or LQ control could also help refine the optimization process.

In order to maximize load sharing utilizing an ideal servo LQG technique comparable to [49], a virtual impedance controller [78] is used in [67]. In order to create a signal reference, the writer used a second-order generalized integrator (SOGI). Furthermore, the whole inverter is represented as a thevenin equivalent, complete with a virtual impedance, an alternating current (AC) voltage source, and a parallel AC current source for fundamental and harmonic current. The controller takes harmonic power into account by using instantaneous current and voltage values.

A PSO-based optimum control strategy was laid forth in [65].

In order to reduce frequency variations, the author suggested the following performance metric:

$$J = \sum_{k=1}^{N} \sum_{n}^{l} \left[nTE_{\omega_k}(n) \right]^2 \tag{2.34}$$

At what point does the inverter's frequency error occur? Which “represents the total number of samples, which represents the sampling period, and which represents the total number of inverter

units in the isolated microgrid. The frequency deviations are optimized and the transient responsiveness is enhanced by power sharing. Active power losses are avoided and phase oscillatory behavior is decreased by limiting frequency variations.

One last place to look for the best values for the V-I and active-reactive power-sharing controller coefficients is in [42], which uses a PSO approach. After determining that the integral component is unnecessary for the present controller because of its effect on system eigenvalues, the V-I controllers are specified as pid and p con-trollers. For better transient responsiveness and controllability, the active power controller is also built as a PD controller. In this method, choosing the active power-sharing controller's proportional gain with the largest possible margin is the goal. It has been shown that droop controllers have an effect on the stability of isolated microgrids, therefore this is done. The optimization is limited to solutions where the damping ratio is less than 0.5 and the greatest eigenvalue remains in the right half complex plane. The pso technique was used to determine the best possible values for the active power proportional, integral, and derivative control constants as well as the voltage proportional and derivative control constants at the local level. When compared to earlier work, the results give significant improvements, as seen in [41]. It was shown that this approach maximizes the active power-sharing controller's proportional gain. Maximizing these aspects enhances the stability and transient responsiveness of the system.

The contributions of optimal control to the regulation of distributed power sharing have been limited so far. Developing a mathematical model that incorporates power sharing and V-I dynamics is a major constraint, which is the primary cause of this. A wide variety of resilient and optimum control methods are applicable to this model. The system and controller are treated as one cohesive state-space system in the models that have been established in the literature. Next, we examine the eigenvalues of this system by varying the droop control gains. While these models work well for stability analysis, they aren't cut out for making durable or optimum controller designs.

2.2.3 Power Sharing Droop Control Summary

A total of twenty-five articles pertaining to droop control techniques for microgrids were examined in this literature study. A synopsis of these works is shown in Table 2. Journal articles account for eighteen of these publications, while conference proceedings account for seven.

Figure 31 shows that all relevant works were assessed before 2008, and the majority of the reviewed works are less than 10 years old

Summary of Reviewed Droop Control Methods for Microgrids

Table 2.2

Ref	Year	Citations (gscholar)	Type of Publications	Controller
[22]	2012	527	journal	survey
[28]	2016	209	journal	survey
[36]	2013	398	journal	classical
[66]	2017	41	journal	Virtual impendence
[39]	1997	374	conferencia	classical
[40]	1999	125	conferencia	classical
[41]	2007	1545	journal	classical
[42]	2014	2	conferencia	optimal
[51]	2010	492	journal	optimal, classical
[65]	2012	74	journal	optimal
[67]	2015	na	conferencia	optimal
[68]	2017	79	journal	survey
[69]	2008	595	journal	survey
[70]	1984	3902	journal	Teoria de potencia
[71]	2004	450	journal	classical
[72]	2013	195	journal	classical
[74]	2014	90	journal	classical
[75]	2012	80	journal	classical
[76]	2004	949	journal	classical
[77]	2015	39	journal	classical
[78]	2005	992	journal	Virtual impendence
[79]	2017	na	conferencia	Virtual impendence
[80]	2013	487	journal	Virtual impendence
[81]	2014	na	conferencia	optimal
[82]	2002	552	journal	classical

2.3 Conclusion

The bulk of the literature that has been examined focuses on classical droop control techniques. The reason is that heuristics for determining droop gains form the basis of conventional droop controllers. In order to guarantee stability, certain classical controllers examine the controlled microgrid's eigenvalue structure. Adding control loops to mitigate counter effects in microgrids during faults has also been the primary emphasis of droop control contributions.

Stability is affected by numerous elements at the power-sharing control level. The transmission line impedance uncertainty is the most crucial component. A suggested virtual impedance control loop aims to tackle this uncertainty. Harmonic distortion and transient responsiveness to abrupt load changes may both be improved by using virtual impedance.

The number of papers on optimal controllers for power-sharing control has decreased during the last decade. One possible reason for this is the need for a consistent model that depicts the dynamics of v-i and power sharing as a system in state space. Improving transient responses, stability, and resilience may be achieved by using several optimum and robust control techniques.

Chapter 3

Methodology

The approach that was employed to generate this study is presented in this chapter. The methodology used to achieve specific objectives from section 1.3.2 is developed in each subsection of this chapter.

3.1 Specific Objective 1: Introduce a Novel Open-Loop State space Model of an Inverter-Based Generator that Includes V-I and Power Sharing Dynamics.

There are two steps to get the model that this study suggests. In grid-connected mode, the dynamics are represented by an inverter's model which is linked to the main grid. The recommended control method is also developed using this model. Then, to depict the dynamics of the microgrid in island mode, all of the inverter models are combined into a single state-space model.

3.1.1 Model of a Single Inverter Connected to the Main Grid

The suggested model was built in grid-connected mode using the circuit seen in Figure 3.1. The output of a three-phase inverter is linked to a rigid voltage source, which stands in for the main grid, using a LCL output filter. The output, input inductor current, and voltage across the capacitor are represented by:

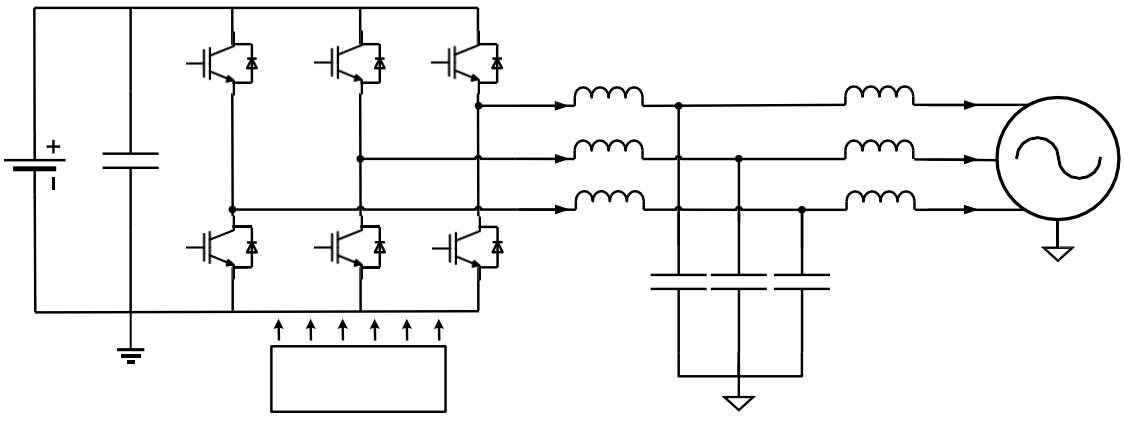

Fig. 3.1. Three-phase generator connected to a voltage source

This circuit's state-space model is provided for every step in the ABC frame by (65)

Appendix A shows the dq transformation that is used to construct the state-space model (66) [83]. To carry out the dq transformation, we assume an angular frequency that is constant; this frequency is the same as the main grid's nominal angular frequency.

$$\begin{bmatrix}\dot{V}_c\\ \dot{I}_l\\ \dot{I}_o\end{bmatrix}=\begin{bmatrix}0 & 1/c & -1/c\\ -1/L_i & 0 & 0\\ 1/L_o & 0 & 0\end{bmatrix}\begin{bmatrix}V_c\\ I_l\\ I_o\end{bmatrix}+\begin{bmatrix}0\\ 1/L_i\\ 0\end{bmatrix}E+\begin{bmatrix}0\\ 0\\ -1/L_o\end{bmatrix}V \tag{3.1}$$

$$\dot{x}=A_{dq}x+B_{1dq}E_{dq}+B_{2dq}V_{dq} \tag{3.2}$$

$$x=\begin{bmatrix}V_{cd}\\ V_{cq}\\ I_{ld}\\ I_{lq}\\ I_{od}\\ I_{oq}\end{bmatrix};A_{dq}=\begin{bmatrix}0 & \omega_c & 1/C & 0 & -1/C & 0\\ -\omega_c & 0 & 0 & 1/C & 0 & -1/C\\ -1/L_i & 0 & 0 & \omega_c & 0 & 0\\ 0 & -1/L_i & -\omega_c & 0 & 0 & 0\\ 1/L_o & 0 & 0 & 0 & 0 & \omega_c\\ 0 & 1/L_o & 0 & 0 & -\omega_c & 0\end{bmatrix} \tag{3.3}$$

$$B_{1dq}=\begin{bmatrix}0 & 0\\ 0 & 0\\ 1/L_i & 0\\ 0 & 1/L_i\\ 0 & 0\\ 0 & 0\end{bmatrix};E_{dq}=\begin{bmatrix}E_d\\ E_q\end{bmatrix};B_{2dq}=\begin{bmatrix}0 & 0\\ 0 & 0\\ 0 & 0\\ 0 & 0\\ -1/L_o & 0\\ 0 & -1/L_o\end{bmatrix};V_{dq}=\begin{bmatrix}V_d\\ V_q\end{bmatrix} \tag{3.4}$$

The active and reactive power injected is defined by:

$$P=\frac{3}{2}\left(V_dI_d+V_qI_q\right) \tag{3.5}$$

$$Q=\frac{3}{2}\left(V_qI_d-V_dI_q\right) \tag{3.6}$$

$$Y=\begin{bmatrix}P\\ Q\end{bmatrix}=\frac{3}{2}\begin{bmatrix}\bar{V}_d & 0\\ 0 & -\bar{V}_d\end{bmatrix}\begin{bmatrix}I_{od}\\ I_{oq}\end{bmatrix} \tag{3.7}$$

3.1.2 Model of the Microgrid in Islanded Mode

By simulating an isolated microgrid, we were able to test the suggested controller's resilience and stability in islanded mode. To use the state-space model while operating in grid-connected mode, it is necessary to operate each generator independently (66). Figure 3.2 depicts the circuit that was taken into account for the isolated microgrid model and explained by self-explanatory equations in (3.8), (3.9), (3.10) & (3.11)

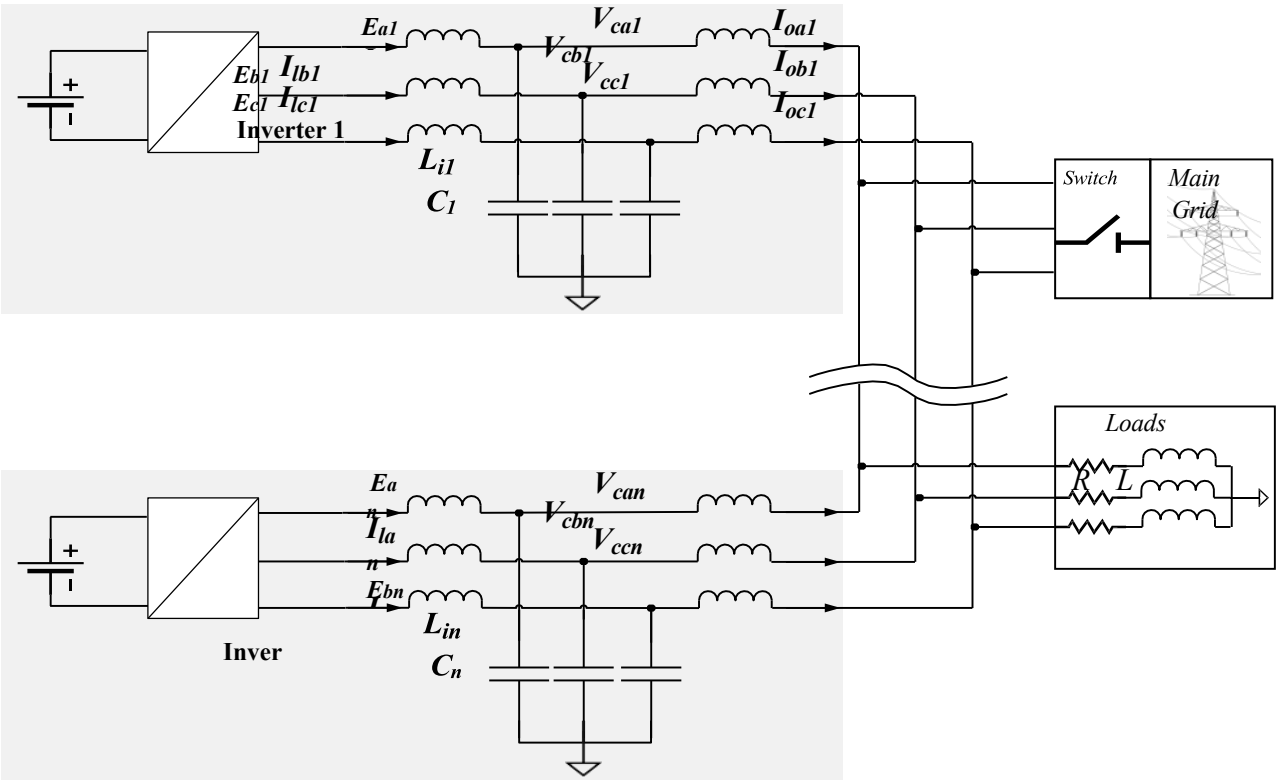

Fig. 3.2. Complete Islanded microgrid scheme with an RL load

Microgrids may accommodate a wide variety of loads; however, a circuit load is used for this example since it is ubiquitous in both residential and commercial settings. For the whole microgrid model to be generated, it is required to calculate the model for one phase of every inverter utilizing equation (65). Then, the following definition must be applied to the load components and output currents

$$V = L\dot{I}_{ot} + RI_{ot} \tag{3.8}$$

$$\begin{bmatrix}\dot{V}_{c1}\\ \dot{I}_{l1}\\ \dot{I}_{o1}\\ \dot{V}_{c2}\\ \dot{I}_{l2}\\ \dot{I}_{o2}\end{bmatrix}=\begin{bmatrix}0 & 1/C_1 & -1/C_1 & 0 & 0 & 0\\ -1/L_{i1} & 0 & 0 & 0 & 0 & 0\\ L_{t2}/L_t & 0 & (RL-RL_{t2})/L_t & -L/Lt & 0 & (RL-RL_{t2})/L_t\\ 0 & 0 & 0 & 0 & 1/C_2 & -1/C_2\\ 0 & 0 & 0 & -1/L_{i2} & 0 & 0\\ -L/Lt & 0 & (RL-RL_{t1})/L_t & L_{t1}/L_t & 0 & (RL-RL_{t1})/L_t\end{bmatrix}\begin{bmatrix}V_{c1}\\ I_{l1}\\ I_{o1}\\ V_{c2}\\ I_{l2}\\ I_{o2}\end{bmatrix}+\begin{bmatrix}0 & 0\\ 1/L_{i1} & 0\\ 0 & 0\\ 0 & 0\\ 0 & 1/L_{i2}\\ 0 & 0\end{bmatrix}\begin{bmatrix}E_1\\ E_2\end{bmatrix} \quad (3.9)$$

$$\begin{bmatrix}\dot{I}_{o1}\\ \vdots\\ \dot{I}_{on}\end{bmatrix}=\begin{bmatrix}(L_{o1}+L) & L & L\\ L & \ddots & L\\ L & L & (L_{on}+L)\end{bmatrix}^{-1}\begin{bmatrix}V_{c1}-RI_t\\ \vdots\\ V_{cn}-RI_t\end{bmatrix}=\begin{bmatrix}\varphi_1\\ \vdots\\ \varphi_n\end{bmatrix}\begin{bmatrix}V_{c1}\\ I_{l1}\\ I_{o1}\\ \vdots\\ V_{cn}\\ I_{ln}\\ I_{on}\end{bmatrix} \quad (3.10)$$

$$\begin{bmatrix}\dot{V}_{c1}\\ \dot{I}_{l1}\\ \dot{I}_{o1}\\ \vdots\\ \dot{V}_{cn}\\ \dot{I}_{ln}\\ \dot{I}_{on}\end{bmatrix}=\begin{bmatrix}\tilde{A}_1 & 0_{2\times3} & \dots & \dots & 0_{2\times3}\\ & & \varphi_1 & & \\ 0_{2\times3} & \dots & \tilde{A}_2 & \dots & 0_{2\times3}\\ & & \varphi_2 & & \\ \vdots & \vdots & \vdots & \vdots & \vdots\\ 0_{2\times3} & \dots & \dots & 0_{2\times3} & \tilde{A}_n\\ & & \varphi_n & & \end{bmatrix}\begin{bmatrix}V_{c1}\\ I_{l1}\\ I_{o1}\\ \vdots\\ V_{cn}\\ I_{ln}\\ I_{on}\end{bmatrix}+\begin{bmatrix}B_1 & \dots & 0_{3\times1}\\ \vdots & \ddots & \vdots\\ 0_{3\times1} & \dots & B_n\end{bmatrix}\begin{bmatrix}E_1\\ \vdots\\ E_n\end{bmatrix} \quad (3.11)$$

Microgrids may accommodate a wide variety of loads; however, a circuit load is used for this example since it is ubiquitous in both residential and commercial settings. Computing the model for one phase of every inverter utilizing equation (65) is necessary to generate the whole microgrid model. Then, the following definition must be applied to the load components and output currents

3.2. Specific Objective 2: Perform Robustness and Stability analysis of the Open-Loop State-Space Models

The three-phase inverter-based generator's stability, performance, and robustness measures, including eigenvalue structure, phase margin, and gain margin, were to be examined by creating an open-loop state-space model. Singular value plots, root locus, and other similar

approaches may help find these traits. We selected the most suitable method of control for this investigation based on the results of this research.

Both grid-connected and island models need stability and robustness analyses. When operating in grid-connected mode, it is necessary to examine the model of every inverter independently to conduct stability and robustness analyses. This inverter's discrete transfer function is denoted as:

$$G_i(z) = \bar{C}_{dqi}\left(zI - \bar{A}_{dqi}\right)^{-1}\bar{B}_{1dqi}. \tag{3.12}$$

Separate the matrices. In island mode, we also use the following microgrid discrete-time transfer function for robustness and stability studies:

$$G_{\mu G}(z) = \bar{C}_{\mu G}\left(zI - \bar{A}_{\mu G}\right)^{-1}\bar{B}_{\mu G} \tag{3.13}$$

We tested the stability and robustness of vg() and used it with randomly varying components to see how they fared under component variations using the robust control toolbox in MATLAB [57]. After getting the nominal values of μg( ), as well as cases with different values, the following study of stability and robustness may be carried out. One method is the eigenvalue analysis, which involves plotting the eigenvalues of a motion transfer function on the complex z-plane and seeing whether they stay within the unit circle. When certain eigenvalues are beyond the unit circle, it shows that the system or its variants are intrinsically unstable. It is possible to deduce information on the transient response from the location of the eigenvalues.

Stability margin analysis: The disc margin method may be used to assess the structured resilience of mimo systems with negative feedback in the presence of multiplicative uncertainty [86]. Once all loop interactions and frequencies have been taken into account, the disk-based margins are computed. Phase margins and structured gain are now supported by more careful evidence according to this research. It is common practise to utilise single-value graphs for studying the frequency response of mimo systems [18]. A mimo transfer function's maximum and lowest singular values are shown in this frequency response graphic. This paper shows the results of an inquiry into the stability and resilience of the open-loop state-space models employed in the research, which allows for the limitation of the regulated closed-loop system's performance.

3.3 Specific Objective 3: Validate The Open-Loop State-Space Models

To validate the model, we compared the output of the mathematical models νg( ) and () with the output of the circuits shown in Figure 3.3 and Figure 3.4 when subjected to the same input signal. This validation can only take place if there is communication between at least two uncontrolled generators connected to the AC bus. For safety considerations, it is required to use simulation tools, such as the Opal 5700 real-time simulation libraries for matlab-simulink [2], to develop the circuits. Opal libraries, like Artemis, allow for a precise simulation of the inverter's switching behavior, including its impacts on inductor currents and capacitor voltages.

To verify that the mathematical model of an inverter connected to the main grid is accurate, it is required to simulate the circuit, simultaneously with its mathematical model. Likewise, for an island microgrid's mathematical model to be validated, the microgrid scheme simulation it has to be executed simultaneously with its mathematical model μg(). Both the grid-connected and islanding validation modes used the same input signal, for both the mathematical model as well as the simulated circuit. To evaluate transient reactions, the three-phase reference generator causes amplitude changes to occur in discrete steps.

State vector and injected power responses are shown and contrasted graphically. When comparing the results from the mathematical model and the circuit, the NRMSE ("Normalized Root Mean Squared Error") is used, as stated in [87]:

$$NRMSE = 100 \times \left(1 - \frac{\|y_{\text{ref}} - y\|}{\|y_{\text{ref}} - \text{mean}(y_{\text{ref}})\|}\right). \tag{3.14}$$

The mathematical reference and the temporal response of a measurement are represented by vectors, respectively. If the fit is great, the nrmse is 100%, and if it's terrible, it's $-\infty$. Since it takes the whole measurement over a certain period into account, the nrmse is a good fit for this validation. Each power measurement as well as state variable must have its nrmse calculated. Because this study does not account for parasitic phenomena or other neglectable nonlinear dynamics of the components, it is reasonable to assume that there will be some discrepancies between the two systems. On the other hand, we may anticipate that both systems will have

comparable transient response and frequency response characteristics [57]. In Section 4.3, the open-loop state-space models that were used in this study are detailed.

3.4 Specific Objective 4: Formulate a Control Method that Optimizes Performance, Stability, and Robustness Characteristics Of The Inverter-Based Generator In Islanded Mode.

A contemporary control approach such as LQR, ∐, or -synthesis requires an open-loop state-space model to use numerical optimization techniques that find a suitable controller based on a specific control aim. Utilizing the proposed integrated model in the dq frame (66) and the superposition principle, inverter-based generators may be controlled using modern approaches. These methods include v-i and power-sharing dynamics while improving transient resilience and responsiveness.

Based on the classic LQR problem, this research proposes a PQVI controller. The LQR controller features an infinite gain margin and a minimum phase margin of 60°, which are robustness qualities that are guaranteed [15]. The LQR controller is designed to minimize input and state energy consumption to enhance transient reaction times and decrease power losses. Nonetheless, starting from a certain beginning state 0, the goal of the conventional LQR controller is to zero out all state variables. Optimum reference tracker (LQR-ORT) is a modification to the basic LQR controller that is used for this study [15]. This is because optimum power sharing is a typical tracking challenge.

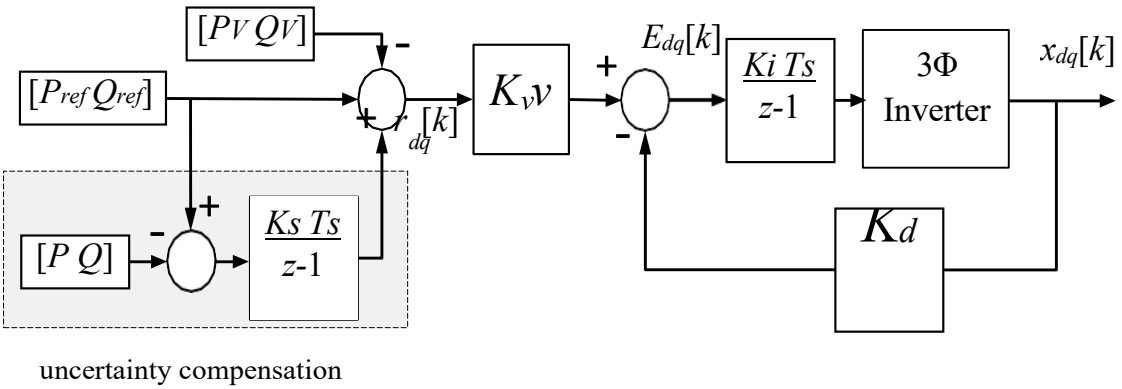

Fig. 3.3 Control scheme for the LQR-ORT controller

Every inverter's LQR-ORT controller is built using the grid-connected approach (66). This controller can switch between grid-connected and island modes of operation. Voltage and frequency fluctuations in the AC bus may be corrected using non-communicative additional loops in the event of an abrupt grid outage. Additionally, the secondary voltage correction loop may allocate power production based on the rated power of every inverter.

3.4.1 Proportional Power Sharing and Voltage Restoration

When the microgrid is operating in isolated mode, voltage discrepancies may be restored using a voltage restoration loop. See Fig. 3.4 for a schematic of the voltage restoration loop's control architecture. When the main grid connection is severed, the AC bus voltage drops and the grid connection flag goes to zero. It is presumed that grid disconnection may be detected building it is outside the purview of this study. To fix the AC bus voltage even when there is no connection, an additional

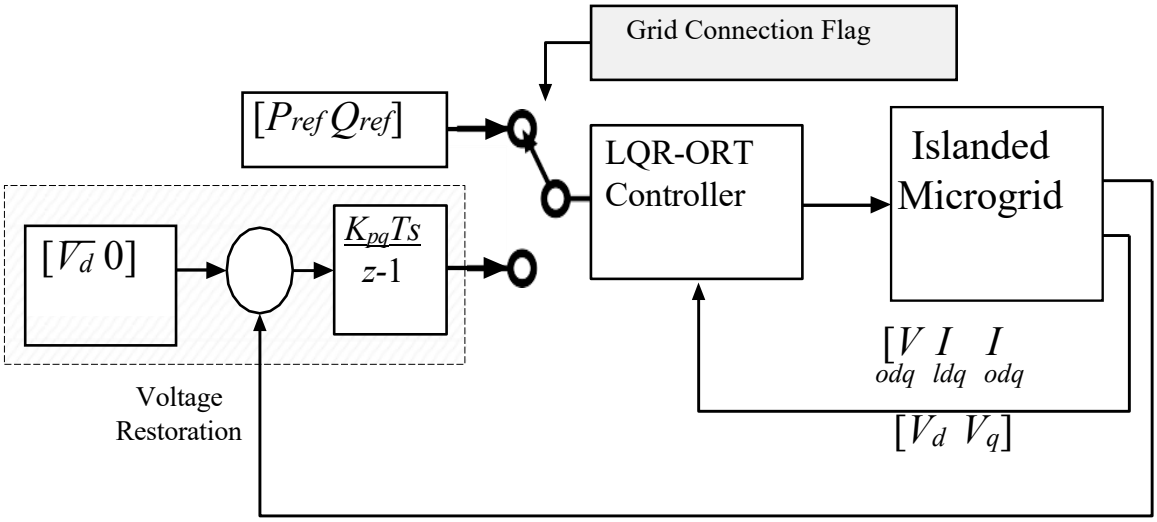

Fig. 3.4. Control scheme for the voltage restoration loop

Here is the revised power reference phrase for the i-the inverter:

$$P_{refi} = \frac{K_{pi}T_s}{Z-1}(V_d - \bar{V}_d) \tag{3.15}$$

$$Q_{refi} = \frac{K_{qi}T_s}{z-1}(V_q) \tag{3.16}$$

A positive active power increase and a negative reactive power gain are required by equation (70). Once the system is stable, the LQR-ORT controller's value is =. As a second example, consider a pair of inverters linked to an AC bus:

$$\frac{P_1}{P_2} = \frac{K_{p1}}{K_{p2}} \tag{3.17}$$

$$\frac{Q_1}{Q_2} = \frac{K_{q1}}{K_{q2}} \tag{3.18}$$

For two inverters linked to the ac bus, expressions (3.17) and (3.18) are obtained by splitting power expressions (3.15) and (3.16). The supplemental loop may distribute power according to each inverter's rated power capacity without communications in islanded mode, as shown by these formulas. With a 2 pu rating for inverter 2 and a 1 pu rating for inverter 1, the two inverters will share twice the power, so 2/1= 2.

3.4.2 Inverter Synchronization and Frequency Restoration

Figure 3.5 shows the AC bus synchronization with each inverter using a second-order generalized integrator (sogi-pll) [10]. Through the use of the sogi-output, PLL'S the input and output signals of the LQR-ORT controller are transformed using dq. The microgrid's operational frequency decreases and the frequency restoration loop operates in the event of a grid interruption. The PLL operational frequency is fixed by the frequency restoration loop by incorporating the frequency inaccuracy. Isolated mode restores the nominal microgrid frequency at the cost of increasing the output frequency of each generator. It follows that the suggested frequency restoration loop allows the PQVI controller and other dq frame controllers to function in grid-connected or island mode. An equation for the sogi-output PLL'S based on a frequency restoration loop

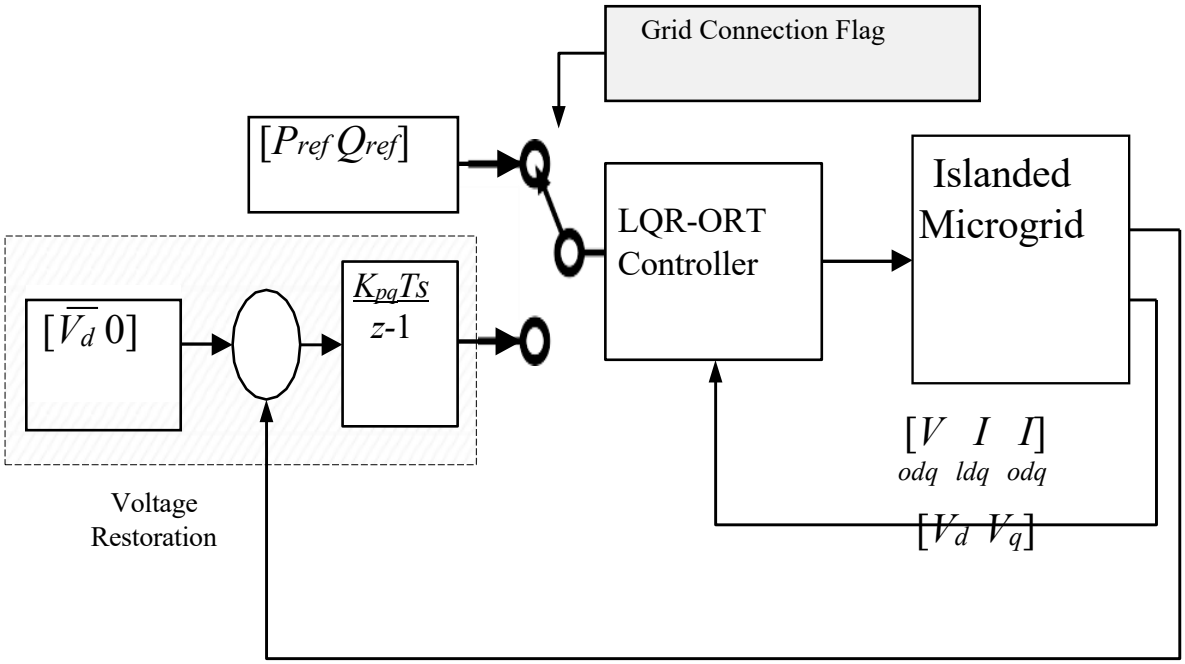

Fig. 3.5. Sogi-PLL with frequency restoration loop

3.4.3. Complete PQVI Control Scheme

In Fig. 3.6, we can see the whole PQVI control system operating one inverter. The PLL-SOGI is synced with the ac bus and operates independently of each inverter. Using the PLL-output, sogi's states and control input is dq converted. When connected to the larger grid, each inverter moves in lockstep with the grid, thereby creating a microgrid. For AC buses, this implies that grid regulation dictates both voltage and frequency. When the grid connection is broken, the inverters start acting as generators that contribute to the grid. When this happens, the voltage and frequency restoration loops are activated, and the grid connection flag is turned on.

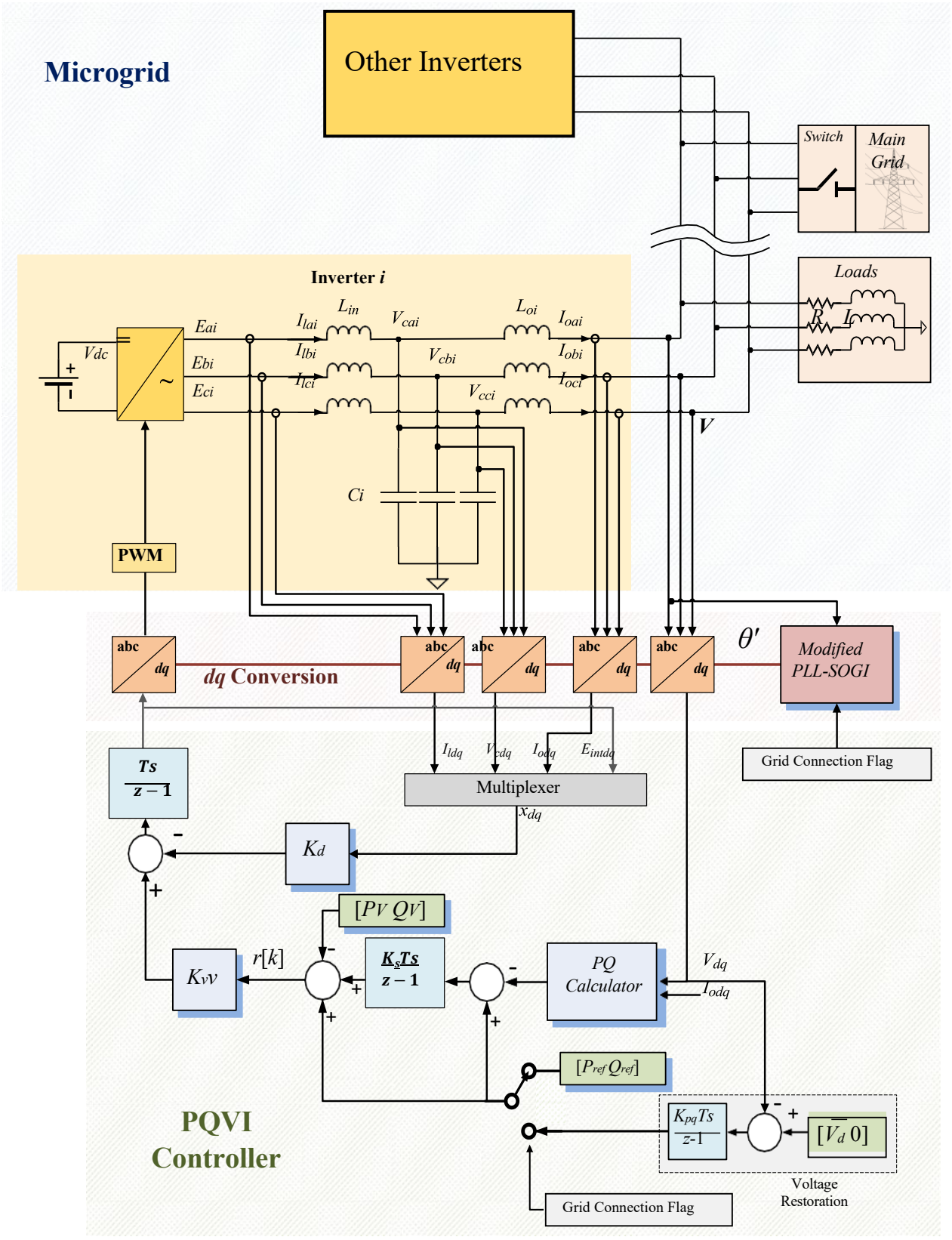

Fig. 3.6. Complete PQVI control scheme

3.5 Specific Objective 5: Perform Robustness and Stability Analysis to The Controlled State-Space Model

To achieve this goal, it is necessary to carry out the same analyses that were suggested in objective 2. The results of these evaluations show how capable the suggested controller is. Every inverter is required to use the following grid-connected open-loop model of the regulated plant for stability as well as robustness analyses:

$$\lambda_i(z) = K_{di}\left(zI - \bar{A}_{dqi}\right)^{-1}\bar{B}_{1dqi} \tag{3.19}$$

Furthermore, for the whole microgrid, the following controlled plant-islanded open-loop model is required:

$$\lambda_{\mu G}(z) = K_{dT}\left(zI - \bar{A}_{\mu G}\right)^{-1}\bar{B}_{\mu G} \tag{3.20}$$

Where ¯ and ¯ are "the discrete-time state and input matrices from (77) transformed to the *dq* frame. Equation =diag(1,2,...,) represents the feedback control matrix. One way to evaluate the stability is by looking at the return difference, which indicates where the closed-loop eigenvalues are located (+ λ( ).

$$\lambda\{(I + \Lambda_i(z))^{-1}\} = \lambda\{\bar{A}_{dqi} - \bar{B}_{1dqi}K_{di}\} \tag{3.21}$$

$$\lambda\left\{\left(I + \Lambda_{\mu G}(z)\right)^{-1}\right\} = \lambda\{\bar{A}_{\mu G} - \bar{B}_{\mu G}K_{dT}\} \tag{3.22}$$

The calculation of the eigenvalues is denoted by the operator $\{\cdot\}$. When studying the dynamics and frequency response of mimo systems, the singular value diagram is a popular tool [18]. The graphic depicts the frequency response of the matrix transfer function's maximum and lowest singular values. Additionally, certain performance criteria for the closed-loop system may be established for transient response and disturbance rejection. The singular value plots of λ1( ), λ2( ), λ3( ), and λ ( ) are to be evaluated according to the following requirements:

1) All Λi( ) must have a slope of -20db/dec at low frequencies to achieve zero steady-state error.
2) According to the IEEE 1547-2018 standard, a converter that is linked to the main grid is required to have a frequency ride through within a range of ±4hz (±25.13rad/s) [89]. This is

considered a low-frequency interruption for the part of the process in question. For frequencies lower than 25.14 rad/s, all λ () functions must have a minimum singular value higher than 40 dB to fulfill the ride-through criterion.

3) The Crossover Frequency Should Not Fluctuate By More Than 10% When There Are Process Disturbances To Maintain The Settling Time. Harmonic current is a hallmark of process disruption. Harmonic currents originate from the main grid while you're in grid-connected mode. Because of this, the grid-connected mode does not call for harmonic correction. According to the IEEE 1547-2018 standard [89], the total harmonic distortion (thd) must be 5% or below while operating in island mode. Part 4.5 presents the findings from the study's examination of the controlled microgrid's stability and resilience in both grid-connected and island modes.

3.6 Specific Objective 6: validate controller performance

In order to do this, it is necessary to model the integrated PQVI controller with several inverter-based generators linked to a shared AC bus and a shared load, as seen in Figure 3.7

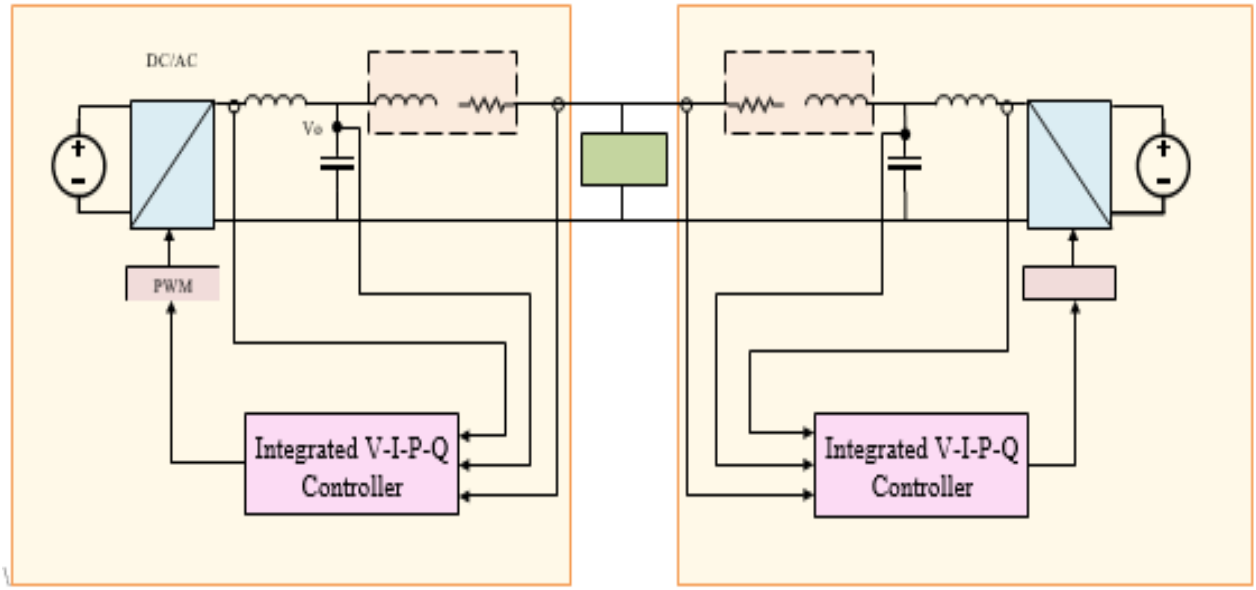

Fig. 3.7. Proposed validation scheme for the Integrated PQVI Controller

Following the validation of the integrated PQVI controller through simulation, it is necessary to utilize the DSPACE system in order to verify its functionality on the microgrid testbed. In order to do this test, you will require a physical AC bus, a regulated three-phase AC load, and at least two inverters that contain a variety of filter components (see Fig. 39). It is possible to use the AC bus to test the proposed controller in grid-connected and island modes simultaneously. Changes in loads are used to evaluate performance. The two generators should divide up the reactive and active power according to their respective ratings, even if they aren't talking with each other in isolated mode. The IEEE 1547 standard also stipulates that the total harmonic distortion (thd) must be below 5%.

3.7 Conclusion: Compare Results against other Control Methods in Literature

To achieve this goal, the controller that was designed for this thesis was compared to droop control and other commonly used control techniques for hierarchical microgrids. An essential set of metrics to compare includes the correct distribution of active and reactive power in island mode, steady-state error, transient response, voltage recovery, and frequency recovery, among others.

Chapter 4

Aggregate Smart Load Reserve pf a Typical system

This chapter uses the Great Britain (GB) transmission system as a case study to evaluate the cumulative effect of all the sls installed within. In the prior chapter, only loads of an impedance type were taken into account. To get a clear picture, we look at historical data while considering various voltage and frequency-dependent loads. As a whole, these SLS would respond to the local frequency measurement, which would allow them to aid in primary frequency management. A "fully decentralised" approach to controlling millions of loads with locally monitored frequency would aid main frequency management the most efficiently, according to analytical evidence [68, 69], and it would not need communication or coordination. The results showed a lack of coordination among the several electric springs (ess).

This study aims to classify the loads on the GB system as prospective sl candidates for the industrial and service sectors using real load data from 2013. (available from the DOE and Climate Change [70]). Due to an absence of similar data available to the industrial and service sectors, this study was unable to include the residential sector. It is possible, nevertheless, to apply the methods outlined in this chapter to the residential sector if the relevant data are available. The main sections of the work are:

(a) Using a time-domain simulation, we can determine (a) the candidate SLS's immediate impact on grid frequency control and (b) the SLS's combined effect on ROCOF and available reserve. Independent of motor as well as static loads, the gb system's power reserve from potential SLS is computed by making careful estimations for several unknown parameters, including load factor and supply voltage at every bus. In order to execute the time domain simulation, we add up the nodes' power reserves at the transmission level (275/400 KV) and represent the remaining demands using their exponential model, which takes into consideration the inherent frequency dependency. Chapter 4's results are supported by the gb system case studies, which show that sls can maintain an acceptable ROCOF and frequency deviation even when there's a big loss of infeed. This case study shows how SLS may help future low-inertia systems function safely,

even if there is a lot of opportunity for mistakes when appropriately expressing and distributing loads. These systems are prone to greater and more frequent infeed losses.

4.1 Smart Load Reserve Calculation

Following the introduction of SSL and MSL in Chapter 2, this section details the procedure for determining the reserve available from these two kinds of sl. An extensive list of parameters, including the following: converter rating, permitted voltage fluctuation across NCL, minimum allowable drive frequency across the motor load, NCL'S type, NCL'S power factor, and supply/mains voltage, are used to define the capabilities of SLS. Since the mains voltage differs at every node of the mv/lv network, the capacity of individual SLS coupled along the feeder would also vary. All mv/lv nodes are assumed to be kept at a minimum of 0.95 pu for the sake of simplicity in the analytical estimate and aggregation of the available reserve. An approximate, cautious estimation of the unlockable reserve from candidate SLS is given by this. Through analysis of average energy consumption statistics, we can determine what proportion of overall consumption is attributed to various NCL types in the GB industrial and service sectors. High power loads with an exceptional load factor are better suited to this strategy. As a last step in evaluating the combined impact on system frequency support, the total active power reserves at the transmission level (275/400 KV) from SSL and MSL may be added together to get the system-wide reserve.

Note That This Study Just Considers Slbc Type Ssl Configurations, As They Are Well-Suited To High-Power Applications

4.1.1 Static Smart Load Reserve

Using exponential relations [71], like (4.1) and (4.2 & 4.3), one may find the active and reactive consumption of a static NCL at any given voltage VNC (4.2 & 4.3). Power consumption at nominal voltage vnc0 is represented by pnc0, which includes both active and reactive power consumption (qnc0). For the sake of clarity, we shall utilize an exponential relation rather than a polynomial connection (zip model). You may use the zip model to get the exponential load model's parameters with little to no approximation. According to other sources, the load data is

also shown as an exponential curve [72~74]. After es is subtracted, the SL'S total nominal power consumption may be determined (5.3).

$$P_{NC} = P_{NC0}\left(\frac{V_{NC}}{V_{NC0}}\right)^{kpv} \tag{4.1}$$

$$Q_{NC} = Q_{NC0}\left(\frac{V_{NC}}{V_{NC0}}\right)^{kqv} \tag{4.2}$$

$$Q_{NC} = Q_{NC0}\left(\frac{V_{NC}}{V_{NC0}}\right)^{kqv} \tag{4.3}$$

The active and reactive power contributions of the compensator, with the ES switched on, may be represented as (4.4) and (4.5). The compensator's injected voltage (Ves) is the sine of the phase angle (es) between the NCL current and the injected voltage.

$$P_{ES} = V_{ES}\frac{\sqrt{P_{NC}^2+Q_{NC}^2}}{V_{NC}}\cos(\theta_{ES}) \tag{4.4}$$

$$Q_{ES} = V_{ES}\frac{\sqrt{P_{NC}^2+Q_{NC}^2}}{V_{NC}}\sin(\theta_{ES}) \tag{4.5}$$

The universal formula for the sl active power consumption may be obtained by applying equations (100) and (104) to any compensation value given by the es (5.6). In a similar vein, the formula for the sub-line reactive power consumption is (4.6 & 4.7)

$$P_{SL} = P_{NC} \pm P_{ES} \tag{4.6}$$

$$Q_{SL} = Q_{NC} \pm Q_{ES} \tag{4.7}$$

It has already been mentioned that the supply/feeder voltage, the compensator voltage, and the NCL voltage are all linked by (2.6). A variety of PSL and QSL values may be obtained by modifying the compensator's injected voltage's magnitude and phase angle. As shown, the smart load power reserve is determined by subtracting the notional consumption (psl0) from the actual consumption (PSL) (5.8). But SSL capacity spanning an area is the result of their being several pes and QES solutions for a given PSL value (fig. 2.13). Assuming “vc=0.95 pu, 20% VNC

relaxation, converter rating restricted to 20% of NCL, and power factor matching the specific sort of NCL being examined, one may determine the largest power reserve (-PSL for under-frequency event) for a SSL" using the p q capacity curve.

$$\delta P_{SL} = P_{SL} - P_{SL0}, \delta Q_{SL} = Q_{SL} - Q_{SL0} \tag{4.8}$$

4.1.2 Motor Smart Load Reserve

Centrifugal loads are driven by induction motors, which actively use power depending on the supply frequency. One may temporarily control the power consumption of certain loads by taking use of this sensitivity; this creates a buffer to sustain the system in case of a frequency spike. The power-frequency sensitivity exponent must be computed in order to represent these motor loads exponentially (KPF). The electrical and mechanical parameters of the induction motor must be used to solve the equivalent circuit equations in order to get the KPF (IM). The analogous circuit of the rotor circuit, with references to the stator side, is shown in Figure 4.1.

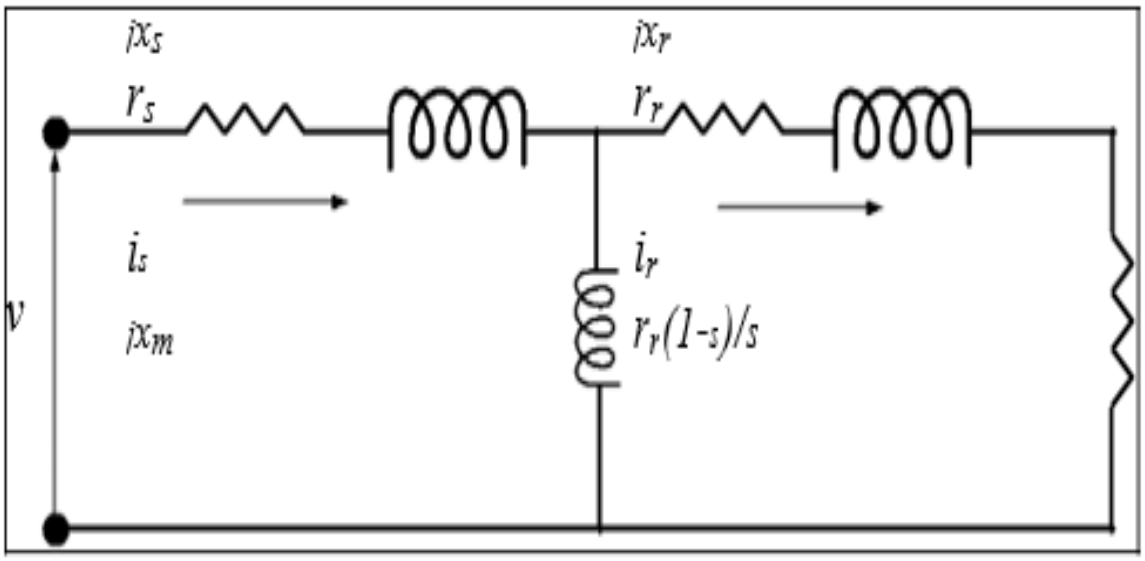

Figure 4.1: induction motor equivalent circuit

Figure 5.1 shows that the current through the stator is and that through the rotor is (107) and (108), with s being the induction motor's slip.

$$\begin{aligned} P_{sh} &= I_r^2 R_r \left(\frac{1-s}{s}\right) \\ P_{\text{loss-s}} &= I_s^2 R_s \\ P_{\text{loss}-r} &= I_r^2 R_r \end{aligned} \tag{4.9}$$

$$\frac{V[R_r/s + j(X_m + X_r)]}{\left[\frac{R_s R_r}{s} - X_s(X_m + X_r) - X_m X_r\right] + j\left[\frac{R_r X_s}{s} + \frac{R_r X_m}{s} + R_s(X_m + X_r)\right]}$$

$$I_s = \frac{V}{(R_s + jX_s) + \frac{jX_m\left(\frac{R_r}{s} + jX_r\right)}{\frac{R_r}{s} + j(X_m + X_r)}}$$

At the output, m's the shaft power is supplied by (5.12), and the stator and rotor losses may be calculated as (4.9).

The equation (5.15), which takes the load torque, motor mechanical speed (wm), and stator magnetic field synchronous speed (ws) into account, may be used to determine the mechanical power needed to draw the IM load. As mentioned in [75], the proposed general equation (5.16), which describes the relationship between motor speed and load torque, may take several forms, including a constant or a quadratic. Section 5.16 defines the variables a, b, c, and d, where c = 1 (a + b + d) and the value of the arbitrary exponent a varies according to the specific uses.

$$P_m = t_m W_m = t_m w_s (1\ s) \tag{4.10}$$

$$t_m = a w_m^2 + b w_m + c + d w_m^a \tag{4.11}$$

Most popular examples of IM applications have coefficients b and d of zero and one, respectively. If we remove the effects of friction and windage losses from equation (4.9), we get equation (4.10), and by replacing TM in equation (4.11) with (4.12), we get the equation that has to be solved to get the magnitude of slip (4.13).

The answers may be obtained by solving the following equation using different values for the electrical characteristics (reactances) of the machine and a variety of frequencies for the stator supply, all while maintaining a constant v=f ratio (4.11). For every supply frequency, knowing the slip of the motor(s) is necessary to obtain the active power consumption of an induction motor. This information is provided by the solution (pin). By combining equations (4.8), (4.9), and (4.10), we get the pin, and the final expression is (4.11), where d is the denominator and is enlarged in (4.12). A value for kpf may be found by plotting the active power consumption against the variation in stator frequency.

$$I_r^2 R_\tau \left(\frac{1-s}{s}\right) = AW_s^3(1-s)^3 + CW_s(1-s) \tag{4.12}$$

$$P_{\text{in}} = \frac{1}{D}\left((V_{\text{in}}X_m)^2 R_\tau \frac{(1-s)}{s} + (V_{\text{in}}X_m)^2 R_r + V_{\text{in}}^2 R_s \left(\left(\frac{R_\tau}{s}\right)^2 + (X_\tau + X_m)^2\right)\right) \tag{4.13}$$

$$D = \left(R_{\text{s}}\frac{R_\tau}{\text{s}} - X_{\text{s}}(X_{\text{m}} + X_r) - X_{\text{m}}X_r\right)^2 + \left(R_{\text{s}}(X_m + X_r) + R_\tau \frac{X_{\text{s}}+X_m}{s}\right)^2 \tag{4.14}$$

The minimum operating frequency of the induction motor drives varies depending on the application. Without specific data for each application, we can only speculate and use 30 hz as a bottom bound for all motor types. The driving frequency is lowered to 30 hz in situations when the grid frequency is outside of the intended range. It is necessary to take into account the sensitivity exponent (kpf), the lowest frequency limit, the operating frequency of a specific motor during the disturbance, and the power reserve from an MSL. A motor running at 50 Hz during the disturbance will generate greater power reserve than a motor running at 40 Hz, assuming the sensitivity exponent and lower frequency limit remain unchanged.

The research is based on the assumption that the operating frequencies of the motors follow a normal distribution with a mean of 50 Hz and a standard deviation of 3 Hz. Paragraph 5.2.8 details the outcomes of sensitivity studies that were conducted with different standard deviations and minimum operating frequency values. Looking at the cumulative distribution function (cdf) with the y-axis as the fraction of motors attached to a busbar allows us to determine all of the motor loads. The formula (5.20) may be used to calculate the power reserve (PSL) value of a busbar, and it represents an enormous range of operating frequencies from the typical distribution.

$$\Delta P_{SL} = \frac{\sum_i P_0\left[\left(\frac{f_1}{f_0}\right)^{kpf} - \left(\frac{f_{\text{dr}}}{f_0}\right)^{kpf}\right]}{\sum_i P_0} \tag{4.15}$$

A minimum acceptable driving frequency of 30 HZ and use fi to represent the random operating frequency at the moment of disturbance in equation (5.20). In the event of an interruption, motors running in constant power mode at frequencies higher than 50 hz will not contribute to the frequency response right away. Before they begin to contribute, their speed is lowered below the normal frequency. The effect of motor inertia is ignored in this study since the power reserve is estimated using a static model. The suggested system for improved drive control, on the other hand, makes use of a df=dt loop to generate artificial inertia.

4.2 Smart Load Reserve

We examine the 37-bus reduced equivalent model of the conventional transmission network to evaluate SSL and MSL'S management of the grid frequency. In the fundamental instance, we take into account both the present and a future low inertia situation. Both the industrial and service sector candidate sls' reserve values are determined using the procedure for reserve calculations given in section 5.1. The case study on the related transmission network subsequently makes use of these numbers.

4.2.1 Service and Industry Sector Loads

To calculate the potential power reserve from the SLS, we look at the yearly power consumption across various industries and sub-industries. Summary statistics from 2013[70] (table 1.07) from the metrological department reveal that overall power consumption was 26375 ktoe or 306.74 twh. All things considered, the home, service, industrial, and transportation sectors account for a portion of total consumption.

The biggest consumer is the residential sector at 37%, followed closely by the industrial sector at 30%, and the service sector at 32%. While the transportation sector (other than heat) only makes up 1% of the market right now, that should change in the not-too-distant future. The percentage shares are shown as a pie chart. industrial and service sector loads, which are further subdivided according to their specific applications such as space heating and lighting, are the only ones included in this study.

Several of the categories listed in Table 1.07 from [70] do not apply to the application and are hence not included in the reserve estimation process. These include computers and cooking/catering.

The distribution of various kinds of loads for the industrial and service sectors is shown in Table 4.2 in GB and figure 4.3 as a pie chart.

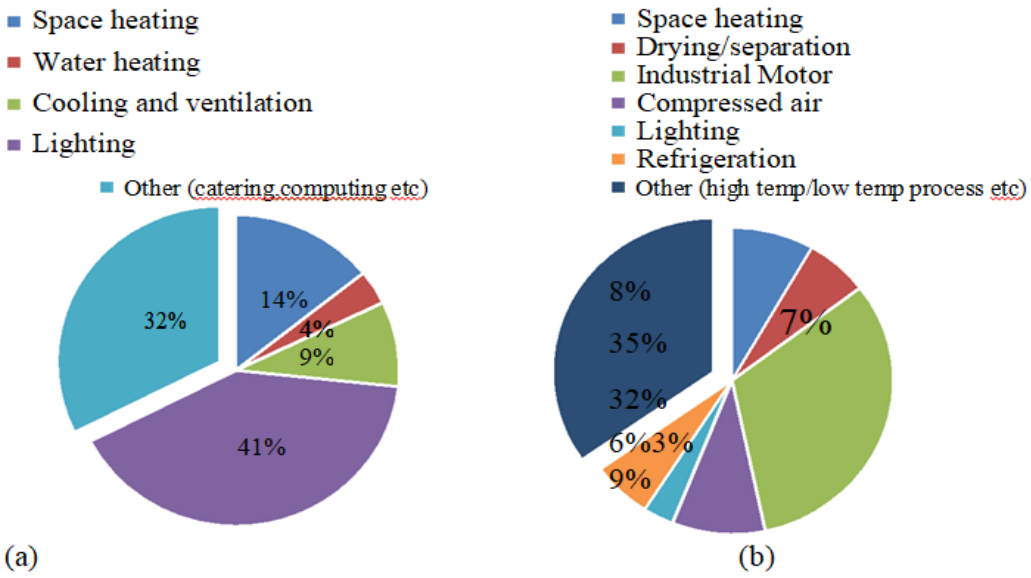

"Figure 4.2: Power System Load Classification for
(a) Service Sector and (b) Industrial Sector

Among the service sector's loads, lighting accounts for 41%, while motor loads make up 32% of the overall load in the industrial sector. Motors that fall into this category have a horsepower rating of 5 hp up to 200 hp or more. There is a distinct display for motor-type loads that serve specialized purposes, such as refrigeration, compressed air, space heating, etc. The "other" category is used for both sectors to gather together loads that aren't SL-appropriate, such as high/low-temperature operations, cooking/catering, computing, etc.

load sector	load category	%	load subcategory	%	lf[1]	capacity (gw)
service (32%)	space heating	14		100	0.6	2.65
	water heating	4		100	0.6	0.76
	cooling/ ventilation	9		100	0.6	1.71
	lighting	41	fluorescent	49	0.6	3.81
			halogen	51	0.6	3.96
	other/ critical	32		100	0.6	6.06
industry (30%)	space heating	8		100	0.8	1.07
	drying/ separation	7		100	0.8	0.93
	industrial motor	32	large motor	50	0.8	2.13
			small motor	50	0.8	2.13
	compressed air	9		100	0.8	1.20
	lighting	3	mercury hp[2]	6	0.8	0.02
			sodium hp[2]	58	0.8	0.23
			sodium lp[3]	2	0.8	0.01
			other	34	0.8	0.14
	refrigeration	6		100	1	0.64
	other/ critical	35		100	0.8	4.66
the total installed capacity of loads						32.12
Table 4.1	**[1]load factor, [2] high pressure, [3] low pressure"**					

There are essentially three types of industrial and service sector loads:

Three types of loads: (a) static, (b) motor, and (c) thermostatic. Static loads are those that do not include motors, such as lights, computers, and stoves, whereas thermostatic loads include all loads that regulate temperature, like ventilation, air conditioning, and heating. The objective of this classification is to ascertain the most efficient means of efficiently extracting frequency response from these loads. Option (a) is an on-off control system; option (b) is an MSL framework that continuously controls the motor supply frequency; and option (c) is a SSL framework that continuously controls the non-critical load voltage. While on-off control isn't always possible or appropriate for all loads, it often provides the highest power reserve and works well with thermostatic loads (owing to thermal inertia).

Recently, adjustable speed drive systems have replaced directly linked motors for loads in the industrial and service sectors, which may be further categorized according to their uses, such as space heating and lighting [76, 77]. For faster frequency response, you may run the loads as msl, and for longer time scales, you can use on-off control. Several categories are included in Table 1.07 from [70], among them are computers and cooking/catering.

4.2.2 Static Smart Load Candidates

Table 5.1 shows loads from the industrial and service sectors, which may be classified as either static or motor-type loads. Table 4.2 shows the two areas' potential static loads. The lighting load accounts for the vast majority of static load, which is mostly attributable to the fact that the service sector accounts for 41% of lighting load while industrial accounts for only 3%. This necessitates further categorization of lighting demand in the service sector [78] (table 4.14). Figure 4.2 is a pie chart that shows how the various sub-sectors contribute to the lighting in the service sector. The retail sector accounts for 35% of the total, which is about three times that of the second biggest contributor. A total of 13% of the illumination in the service sector comes from the necessary public services that deal with transportation (such as street lighting) and the health sector.

Then load using the decc data that is currently available. Due to the exclusion of these critical services, this research only takes into account 87% of the lighting load in the service sector when considering smart load applications. For smart load applications, solid-state lighting loads, such as LEDs, are excellent because they can withstand a broader change in supply voltage. Despite this, led lighting has a vanishingly small percentage in the UK's service and industrial sectors in 2013. As the use of LEDs grows in the future, they may make up a sizable chunk of the overall reserve. The service sector lighting load accounts for 87% of the installed capacity (column (a)) in Table 4.3, whereas all other loads account for 100%. Based on the mathematical approach provided in section 4.1.1, the figures in column (c) are extracted from table 4.3. Table 4.2's column (d) displays the available reserves in GWS, the absolute measure. Column (d) contains the corresponding load capacity, and these units are obtained by multiplying the per-unit reserve in column (c) (b).

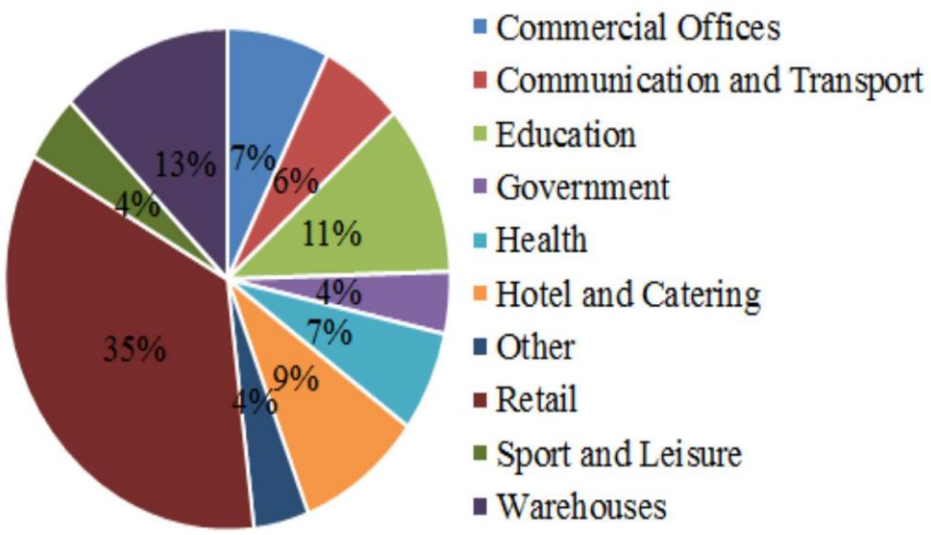

Figure 4.3: contribution of sub-sectors in total service sector lighting load in Great Britain

The lighting type influences the exponent KPV, which in turn defines the power reserve from lighting loads within different sub-sectors. It is clear from [78] (table 4.18), that energy-efficient fluorescent lights make up almost half of the lighting in the service sector, while halogen lamps make up the other half. Table 4.1 also shows the percentage contributions of the four main types of lighting loads in the industrial sector [78]. To keep from flickering or shutting off, these lights need a rather high minimum voltage, also known as switch-o voltage, which is highly dependent on voltage changes. A 20% drop in terminal voltage is quite acceptable, according to the switch on voltages for various hid bulbs [79].

load sector	load category	capacity (gw)	ssl capacity (gw)	ssl power reserve (pu)	ssl power reserve (gw)
		(a)	(b)	(c)	(d)
Service	water heating	0.76	0.76	0.26	0.20
	fluorescent light	3.81	3.31	0.14	0.46
	halogen light	3.96	3.45	0.22	0.76
Industrial	mercury hp light	0.02	0.02	0.29	0.01
	sodium hp light	0.23	0.23	0.3	0.07
	sodium lp light	0.01	0.01	0.08	0.00
	fluorescent light	0.14	0.14	0.14	0.02
	drying/separation	0.93	0.93	0.26	0.24
total static load		9.86	8.85		1.76

Table 4.2: Static Smart Load (SSL) Candidates

4.2.3 Reserve from Static Smart Load Candidates

According to studies [74, 79~81], Table 4.3 summarises the typical exponent values (kpv; kqv) and power factors (pf) for various kinds of static load. Table 4.3 also includes the calculated power reserves that were obtained from the processes outlined in section 5.1.1. With all loads, including the service sector lighting load, maintained constant at 0.95 p.u. (column (a)) from the supply mains voltage, the capability graphs for the static smart loads shown in Table 4.3 are shown in Figure 4.4. The values from column (cdata) in table 4.3 were extracted using the algorithm from section 5.1.1. Table 4.2 shows the entire amount of available reserves given as gws in column (d). Look at column (c) for the per-unit reserve, and then multiply it by the corresponding load capacity to get these units; they're in the table (in column).

load type	pf	kpv	kqv	power reserve (p.u.)
drying	1	1.95	0	0.26
water heating	1	2	0	0.26
fluorescent	0.9	1	3	0.14
halogen	1	1.62	0	0.22
mercury high pressure	0.98	2.4	6	0.29
sodium high pressure	0.99	2.5	-4.25	0.3
sodium low pressure	0.98	0.5	0	0.08

Table 4.3: Static Smart Load Exponents and Calculated Power Reserve

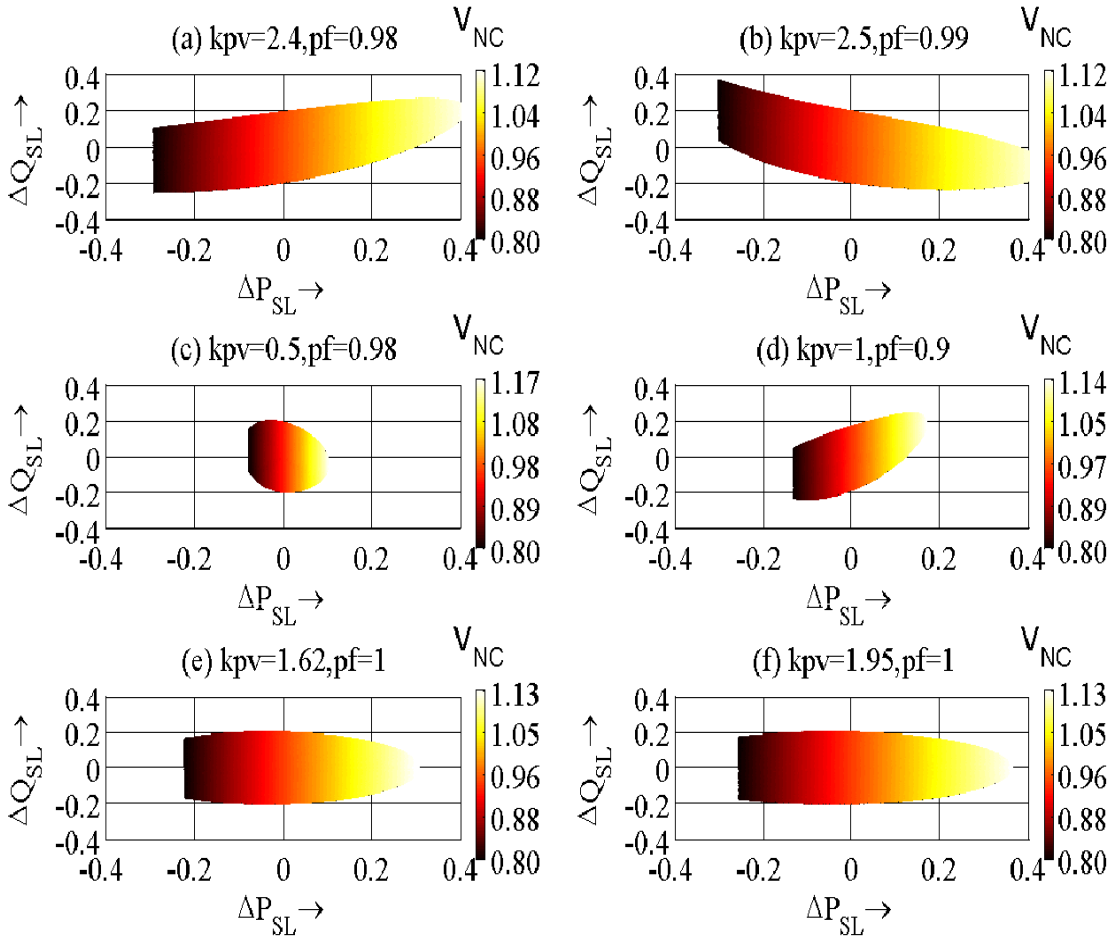

Figure 4.4: Active and Reactive Power Capability of Static Smart Loads
(a) Mercury High Pressure (b) Sodium High Pressure (c) Sodium Low Pressure
(d) Fluorescent (e) Halogen (f) Drying/Water Heating Capability Curves

Other kinds of SSLS, in addition to those used for low-pressure sodium lighting and fluorescent bulbs, may provide a power reserve of around 30% (based on nominal load rating) to allow for a 20% relaxation in non-critical load voltage. Because of their poor voltage dependency, low-pressure lighting loads that use fluorescent and sodium light have a limited power reserve. Sodium low-pressure lamps fall somewhere in the middle of the constant power and constant current types of loads, while fluorescent lights operate more like constant current loads when actively using power. A surge in voltage causes the reactive demand of the load to rise sharply because the reactive powers of fluorescent and mercury high-pressure lamps are very sensitive to changes in terminal voltage and have a positive slope. On the other hand, when sodium is subjected to high pressure, the reactive demand drops dramatically as the voltage increases due to the negative exponent kqv.

A cautious load ratio of 0.6 for the service sector and 0.8 for the industrial sector results in an overall installed capacity of 8.85 GW, or 16.2%, of the GB system's potential SSLS [80]. Therefore, the SSLS reserve deduction is

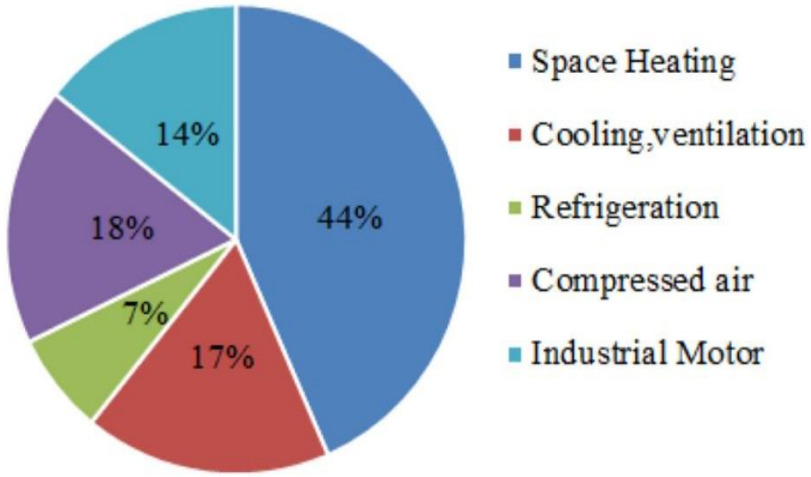

Figure 4.5: Share of Ve Application Areas Out Of Total Industrial and Service Sector Motor Loads

Based on the mathematical approach described in section 5.1.2, the figures in column (c) are derived from (5.20). To get the available reserves in absolute units (GWS), we multiply the per-unit reserve in column (c) of Table 5.4 by the corresponding load capacity in column (d). The results are shown in column (d) (b).

load sector	load category	capacity (gw)	msl capacity (gw)	msl power reserve (pu)	msl power reserve (gw)
		(a)	(b)	(c)	(d)
service	space heating	2.65	0.37	0.425	0.16
	cooling/ventilation	1.71	0.24	0.425	0.10
industrial	space heating	1.07	0.15	0.425	0.06
	large motor	2.13	0.30	0.717	0.21
	small motor	2.13	0.30	0.716	0.21
	compressed air	1.20	0.17	0.717	0.12
	refrigeration	0.64	0	0.692	0
total motor load		11.53	1.52		0.87

Table 4.4: Motor Smart Load (Msl) Candidates"

4.2.4 A Typical Transmission System Model

With 37 buses, 14 asynchronous machines, and 53 synchronous machines, (including marine and wind), as shown in Figure 4.9, a typical transmission system is simplified. Unlike asynchronous machines, which are shown as static generators, synchronous machines use active voltage regulators (AVRS) and governors to keep the active and reactive powers under control and at reference set points. The 1.8 GW spinning reserve in the gb system is a result of the synchronous machines. The transmission network is able to manage a combined load of 56.6 GWh, thanks to its nominal voltage of 400 kv. The 37 zones are constructed using shunt devices, bus-connected loads, and corresponding generators. Using a frequency-dependent exponential model, we can see the overall load in each of these zones. Aggregated loads have constant impedance active and reactive powers, at least in theory [82, 83]. Based on the real gb load classification data provided earlier in the section, each of these loads is labeled as either critical (sensitive) or non-critical. Use SLS to run the optional loads. This thesis does not contain the data given by the National Grid since it is intended for academic study.

4.2.5 Simulation Results

Time domain simulation findings demonstrate that the SLS are successful in providing frequency control service collectively. In order to create an under-frequency occurrence, a 2.0 GW nuclear power plant in zone 22 was turned off 20 seconds into the simulation. This infeed loss, which is slightly more than the gb network's current spinning reserve, caused the worst possible frequency event (1.8 gw). From what anybody can tell, this catastrophe will rank high among the most severe generator outages ever recorded. Smart loads enhance rocof and frequency management, as seen by the dynamic responses in Figures 4.6 and 4.7. These features will be crucial for low-inertia systems in the future [4]. Two scenarios were examined in this study: nominal inertia at current and future low inertia, which is half of present inertia. When inertia is low, the static generator model is used and the ratings of each synchronous generator are cut in half. Figure 4.6(a) and (b) demonstrate the frequency dynamic fluctuation at the upset bus and a remote bus with smart loads and regular loads (nosl) (sl). Quick grid frequency stabilisation and improved frequency nadir are both made possible by the aggregated sls's rapid frequency response.

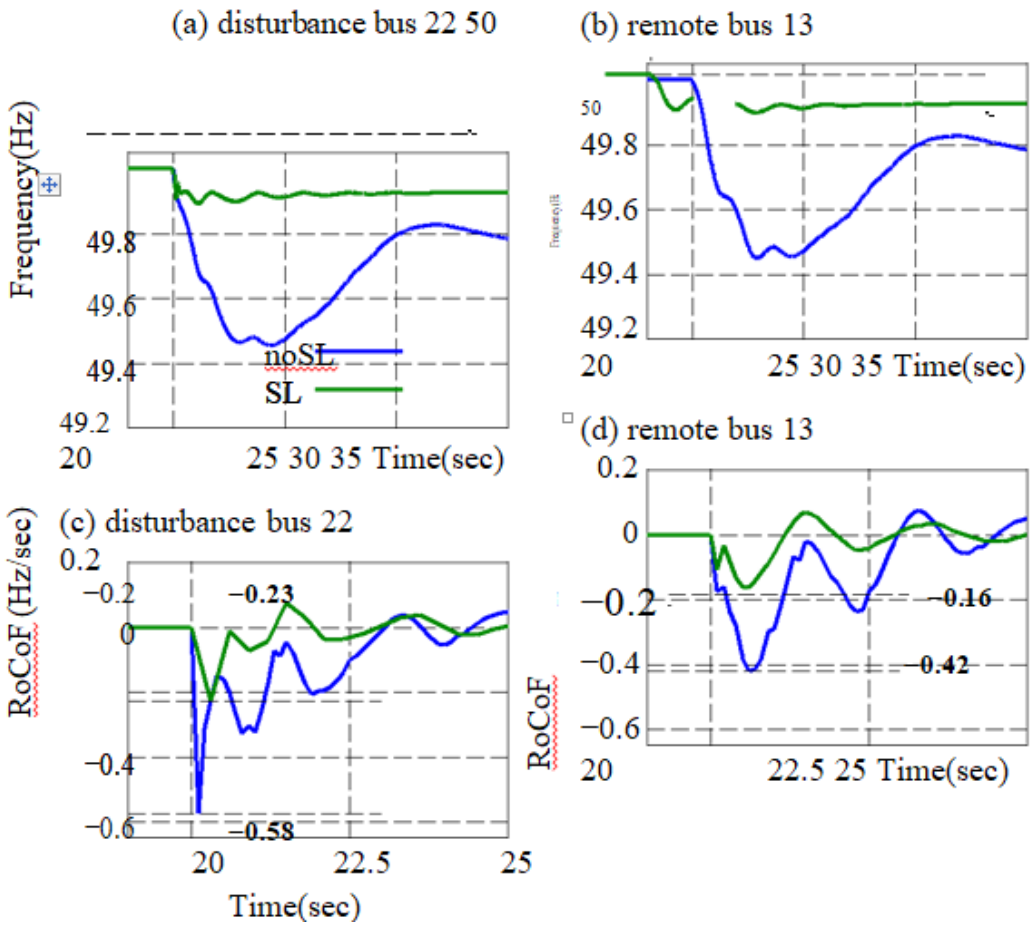

Figure 4.6: Dynamic Variation of Grid Frequency At Bus 22 (A) And Bus 13 (B); and Rocof At Bus 22 (C) And Bus 13 (D) For Present Inertia Scenario (Base Case)

Both the frequency nadir and rocof increase worse with decreasing system inertia compared to the current situation for the same disturbance (Fig. 4.7). When calculating the rocof values, 100ms sliding window is used [84]. As shown in Figure 4.7(c) and (d), Rocof is now operating at around 0.4 hz/s, but it is capable of reaching speeds of up to 1 hz/s in the future [4]. The rocof and frequency nadir may be improved by smart loading even when inertia is minimal.

4.2.6 Sensitivity Analysis

The estimation of the power reserve from SLS in sections 5.2.3 and 5.2.5 was done on the assumption of certain factors. This section presents the findings of the sensitivity analysis that was conducted around the assumed parameters.

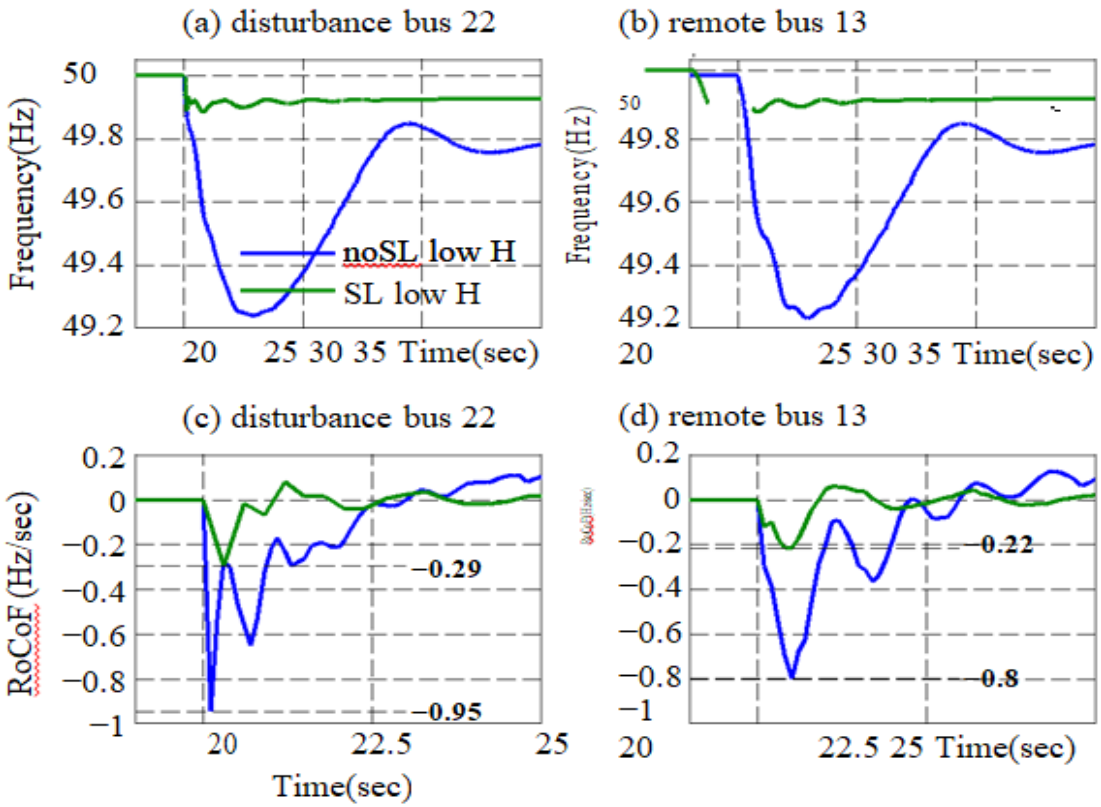

Figure 4.7: Dynamic Variation of Grid Frequency at Bus 22 (A) and Bus 13 (B) and Rocof at Bus 22 (C) and Bus 13 (D) For Future Low Inertia Scenario

In order to achieve better performance and efficiency, loads are anticipated to rise in the future. Figure 4.12 (a) displays the power reserve that may be used by MSL to reduce the number of DOL motors from 80% now to 50% in the future, which translates to an increase in drive-controlled motors. Maintaining the same mix of motor-type loads as in the current scenario significantly increases the available power reserve to a maximum of around 2.0 gw.

The power reserve from drive-based motor loads may be determined while operating at a frequency (fi) lower than the lowest permitted frequency set point (FDR). Power reserve for various standard deviation and minimum driving frequency values is shown in Figure 4.12. (b). The anticipated frequency of operation for motor loads linked to a node is 50 Hz, in accordance with the usual distribution. For the 30- and 40-hertz minimum driving frequencies, respectively, a typical variance of 1-5 Hz is seen. The total power reserve decreases as the standard deviation increases, given that all of the motors must operate at a minimum frequency of 30 or 40 Hz. Considerations such as the SSL grade are important since they determine how the

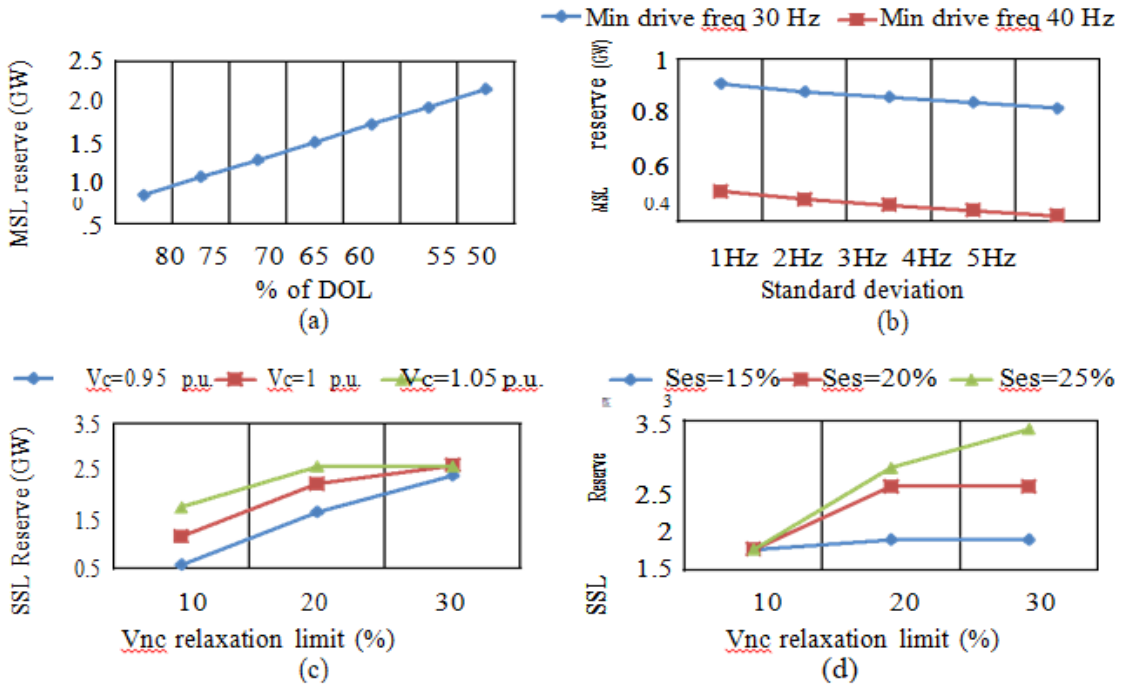

Motor smart loads' (MSLS) power reserve is being studied in relation to three variables: (a) dol motor loads percentage, (b) the minimum permitted drive frequency, (c) the standard deviation of motor loads' operating frequencies (figure 4.7). (c) how the converter rating (ses) relates to the sensitivity of the power reserve available from static smart loads (ssls) to the supply/mains voltage (vc), voltage fluctuation across non-critical loads (VNC), etc. Figure 4.12 (c) shows the effect on the SSL power reserve of changing the VC and VNC relaxation limits, assuming the converter rating cannot exceed 20% of the NCL rating. The power reserve from SSL is enhanced by rising VC and VNC relaxation limits. Any frequency disruption that increases the terminal voltage has our full support because of the tremendous impact it will have on the SSL capability. However, there is a limit to how much an SSL power reserve may rise beyond a certain amount because of the converter rating. For different VNC relaxation limits and converter ratings (ses), the power reserve from SSL is shown in Fig. 4.12 with vc = 1.05 pu (d). Contrary to what is shown in figure 4.8, it is clear that bigger power reserves may be achieved with higher converter ratings.

4.3 Conclusion

In order to demonstrate how SLS efficiently provides quick frequency response, this chapter use the Great Britain (GB) power system as an example. While conventional sources now provide for 1.8 GWh of spinning reserve, industrial and service sector SLS are anticipated to contribute an additional 2.6 GWh to the GB system's overall power reserve. The SLS is able to maintain a reasonable rate of change (rocof) and frequency deviation (FD) even after suffering a significant input loss, according to the simulation findings. Additional investment in a power electronic interface is necessary for SSLS in use the power-voltage dependence of non-motor type loads. Power reserve may be included in drive-controlled motors without the need for extra power electronics with only a little adjustment to the current control circuit. The future is looking bright for reserve from motor smart loads (msls), as the fraction of motors controlled by drives continues to rise. It is important to note that most candidate SLS, particularly in the residential sector, do not operate constantly (24/7). As a result, we need to calculate the power reserve using a window that is either hourly or half-hourly. The next chapter proposes an online estimating approach to deal with the problem of deriving reserve from non-critical loads with low load factors.

Chapter 5

Online Estimation of Aggregate Re-Serve from Smart Loads

Chapter 4's research [22] reveals that the industrial & service sectors in the typical power system might have a reserve employing pol voltage regulators that are similar to the current spinning reserve (1.8gw) of the GB transmission system. Nevertheless, the computations fail to account for the daily fluctuation in energy use as they are based on yearly data for various loads [70]. The time of day affects both the quantity and kind of voltage-dependent loads connected to the system, which in turn affects the available reserve. In addition, the reserve utilizing pol voltage management is sensitive to the ever-changing profile of voltage across the feeders. Therefore, determining the aggregate reserve available from voltage-dependent needs is a difficult but crucial task for grid operators in the context of pol voltage management.

(a) This chapter expands upon the fundamental concepts given in the [85] to provide a technique for load disaggregation on BSPS ("Bulk Supply Points"). To evaluate the aggregate reserve through the various voltage-dependent loads. To calculate the available reserve at a particular moment with a specified confidence level, the grid operators may use the created technology.

(b) It works at any BSP, independent of voltage or rated capacity, and is hence general; (b) after being taught (in the procedure) with a big bunch of data covering any conceivable combination, it may be used for an estimate all year round; (c) it incorporates changes in network losses implicitly and doesn't need an understanding of the distribution network structure. There are two potential applications for the created approach among grid operators: (1) With past/recorded power as well as voltage data at any BSP, one may predict the variance in reserve over the course of a day/month of any given year (2) It is also possible to estimate the available reserve in real-time for usage in time ahead reserve scheduling using current voltage as well as power measurements at any BSP.

(2) There are a few drawbacks to the suggested method: (1) the accuracy of the predicted reserve amount depends on how many voltages dependent load categories are taken into account, and (2) the estimation process becomes more complicated, which introduces inaccuracy. The fluctuations in voltage profile over supply lines. But it does help the grid operators plan other types of reserves by giving them a ballpark figure for the reserve that is available at any given moment, with a certain degree of confidence.

5.1 Reserve Estimation Method

There are a lot of variables that affect the total number of loads connected at any one moment, including the number of people in the home, the time of day, the season, the number of hours worked each shift, and the quality of the surrounding illumination. It is possible to get a significantly off estimate of the reserve if you use the average energy usage of individual loads for the day (or month). The suggested approach seeks to solve this problem by identifying the percentage of each kind of load (based on their voltage dependency) on a minute-to-minute basis via load disaggregation at the BSPS. After considering the voltage changes at BSP as well as the profile of voltage throughout the distribution feeders, the reserve from each load category is calculated. As will be explained later on, ANN (Artificial Neural Networks) have been utilized for the aim of load disaggregation.

There are other heuristic algorithms that can do load disaggregation, such as genetic algorithm, swarm intelligence, support vector machines, etc., and they could even outperform ann. Therefore, ANN-based load disaggregation is not proclaimed that it is best in this study.

There are a few drawbacks to the suggested method: (1) the accuracy of the predicted reserve amount depends on how many voltages dependent load categories are taken into account, and (2) The estimation process becomes more complicated, which introduces inaccuracy. (2) The fluctuations in the profile of voltage across supply lines. But it does help the grid operators plan other types of reserves by giving them a ballpark figure for the reserve that is available at any given moment, with a certain degree of confidence power & voltage at the BSPS for which “static load” models have been adequate. Since the primary focus of the current study is on reserve from pol voltage regulation, loads’ frequency dependence is not taken into consideration. The most frequently utilized zip (2^{nd} order polynomial) or polynomial model along with having

a constant coefficients [60] has been adopted for the current analysis and could be denoted by (1) & (2), here p (q) represented as the reactive (actual active) power, v denoted as the actual voltage, p_0 (q_0) denoted as the reactive (nominal active) power & v_0 represented as the nominal voltage. According to (5.1) & (5.2), in the zip model, Pz; pi; pp indicates the active power's constant coefficients and qz; qi; qp presents the reactive power's constant coefficients.

$$Q = Q_0 \left[qz \left(\frac{v}{v_0} \right)^2 + qi \left(\frac{v}{v_0} \right) + qp \right] \tag{5.1}$$

$$P = P_0 \left[pz \left(\frac{v}{v_0} \right)^2 + pi \left(\frac{v}{v_0} \right) + pp \right] \tag{5.2}$$

5.1.2 Formulation of ANN

The goal of an ANN is to provide a rough approximation of a function with many unknown parameters by using a network of artificial neurons, which are linked computational building blocks modeled after biological neural networks. There are some parallels between ann and biological neural networks, such as the fact that ann is not nearly as complicated as the brain but that connections between neurons determine the network's function.

Because of its simple design and capacity to map complicated input and output interactions, a 2 layer FFANN (Feed-Forward Artificial Neural Network), as illustrated in figure 5.2, is employed for load disaggregation [88]. Figure 5.2 shows the weight matrix as w and the ANN output, input, and bias vectors as a, p, and b, respectively, represented by tiny bold non-italic letters.

Determining the ideal concealed layer size is not a simple task and often requires experimenting. Here, we use a method that was suggested in [89] to estimate category, (b) generate a random sample of voltages and load categories' shares using monte carlo simulation within their certain limits, (c) think about every possible combination of voltages along with the load categories' shares, and (d) create the input as well as target matrices for artificial neural network training using the steps introduced in section 5.1.3.3.(a) through (e), we train the ANN using an FFANN that has hidden layer neurons, as described in equation (5.3).it is unlikely that the trained ANN would be sufficiently general to be used at other substations, since training it with a specific set of measurement data will not cover all potential operational situations. Therefore, in order to capture the daily as well as seasonal fluctuations inside a single estimating model, the ANN has

been trained using the monte carlo approach utilizing an exhaustive dataset, has been made in [85]. A previously trained ANN may be used for real-time load disaggregation without the need for re-training, provided that the training space (such as the p.u. Voltage limitations of the substation) remains constant. Keep in mind that reserve scheduling, which typically occurs every few minutes and does not need much calculation, would make use of the results of load disaggregation.

5.1.3.1. Voltage Measurements

The voltage at the BSPS is typically kept within specific limitations while the system is operating normally [15]. But according to the standard bs en 50160 [91], a voltage range of 0.94-1.1 p.u. is considered. A uniform distribution is used to choose voltage samples at random, guaranteeing that each sample point has an equal chance of being chosen. Nv is the overall number of the voltage samples taken into consideration.

5.1.3.2 Category for Sharing Load

The load combination at the bsp determines the several load categories that need to be evaluated. The five static load categories might include things like lighting, heating, smps, and the remaining two could be motor loads, such as constant torque induction motors and residential cold loads. The proportion of motor load and static load, as measured by the BSP, may range from 0% to 100% at any one moment. All the way up to 100%. There might be 21 different static-motor combinations if the proportion of motor loads changes from 0% to 100% in 5% increments, with the static loads also varying proportionally to make up 100%. To take into consideration the proportion of every load category in p^{agg} and q^{agg} at any given time t, weighting factors (w) must be created at random from a uniform distribution for each of these twenty-one possibilities. By way of example, when the motor load is 40% and the static load is 60%, the weighting factors for each category of motor load have been calculated from 0% to 40%, and the total of these factors is 40%. Similarly, for each category of static load, the weighting factors are calculated from 0% to 60%, and the sum is 60%. Therefore, for every one of the ten types of loads, there must be a positive n_w weighting factor for each of the twenty-one static-motor pairings. Applying equation (5.3) to all possible combinations of voltage samples, static motors, and load types yields the aggregate active power (p^{agg}). The same holds true for calculating q^{agg}

$$P^{agg} = \sum_{i=1}^{m} w_i P_i \quad (5.3)$$

The variables in (5.4) are expressed in units of measurement. The total number of load categories evaluated is represented by m, the "weighting factor for the i^{th} load category is indicated by w_i, and the active power of the i^{th} load category is given using pi. The following formula can be used to determine the i^{th} load category's/nit share (p^{lc} i) of the overall load at the bsp:

$$p_i^{lc} = \frac{w_i P_i}{P_{agg}} \quad (5.4)$$

Every potential combination of voltage-weighting factors, or N_v 21 n_w combinations overall, should be taken into account while creating the input along with the target matrices of an ANN.

5.1.3.3 Input and Target Matrices

At BSPS, the total active along with the reactive power could be computed for every potential voltage and weighting factor combinations using (5.4). These numbers can be thought of as the measures that the BSP has made available. Hence, p^{agg}, q^{agg}, and v make up the input matrix for the ANN training, which is provided by (5.5 & 5.6).

(6.5) is used to create the relevant target matrix for ANN, which is provided by

$$I_{trn} = \begin{pmatrix} P_1^{agg} & P_2^{agg} & \cdots & P_{N_v \times 21 \times N_w}^{agg} \\ Q_1^{agg} & Q_2^{agg} & \cdots & Q_{N_v \times 21 \times N_w}^{ag} \\ V_1 & V_2 & \cdots & V_{N_v \times 21 \times N_w} \end{pmatrix} \quad (5.5)$$

$$T_{trn} = \begin{pmatrix} p_{1,1}^{lc} & p_{1,2}^{lc} & \cdots & p_{1,N_v \times 21 \times N_w}^{lc} \\ p_{2,1}^{lc} & p_{2,2}^{lc} & \cdots & p_{2,N_v \times 21 \times N_w}^{lc} \\ \vdots & \vdots & \ddots & \vdots \\ p_{m,1}^{lc} & p_{m,2}^{lc} & \cdots & p_{m,N_v \times 21 \times N_w}^{lc} \end{pmatrix} \quad (5.6)$$

The dimension of the t_{trn} matrix is the entire several possible combinations of the voltages along with percentages of a load category down the column, and the number of load categories down the row.

5.1.4 Validation of ANN

We may utilize a certain load profile on BSP with a recognized proportion of particular load categories to validate the ANN, or you can build the input & target matrices randomly using the same approach as the training data. The use of a specific load profile may lead to a comparatively bigger inaccuracy when validating a trained ann, in contrast to utilizing a random collection of data (with the same seed as training data), which may demonstrate extremely excellent conformance. This argument has been further upon in section 5.2 with suitable comparisons made later on.

A validation procedure consists of the following steps: (a) creating an I/P matrix i_{val} and a corresponding target matrix t_{val}; (b) feeding i_{val} into the trained ANN to produce an output ovall with the similar dimensions as the tval; (c) because computational error causes the sum of the elements (plci0) in every column of oval0 to be less than one, normalize it as (5.7) and updating the O/P matrix to the oval; (d) the "load category percentage error" (l_{cpe}) matrix is obtained by comparing oval and tval.

$$p_i^{lc} = \frac{p_{i0}^{l^c}}{\sum_{i=1}^{m} p_{i0}^{l_0}} \tag{5.7}$$

You may display the lcpe as a pdf ("Probability Density Function") or a simple histogram graph to highlight the distribution of the errors, as the validation data is a big collection of randomly produced integers. The error distribution may be shown using a different form of the pdf (for ex gaussian or weibull) for each of the load categories

5.1.5 ANN-Based Load Disaggregation

The measurements of p,q, and v taken on BSP may be utilized for load disaggregation once the ANN has been trained as well as verified. The ANN has to be trained on quantities per unit, therefore any absolute readings in rms require to be converted to kw/mw utilizing the value of base or the rated demand on BSP, which changes over time according on the number of connected loads. Given that no BSP has the rated demand information, a probabilistic approach based on monte carlo might be utilized to provide an estimate of the rated demand [92]. For

every voltage value detected at the BSP, a huge set of aggregate active power per unit is computed using equation (5.4). In eq. (5.4), the weighting elements are chosen at random. As per the distribution of active power per unit, the most likely active power (in units) at which voltage is the one with the largest probability density. If we split the actual demand at that voltage by the most likely active power (in each unit), we get the most likely rated demand at BSP for that voltage. Section 5.2 provides evidence that this load disaggregation approach is valid.

5.1.6 Pol Voltage Control

Electric spring (es), a novel smart grid component described in chapter 2, is responsible for point-of-load (pol) voltage management [19]. It is a “power electronic compensator” that is linked in the series having load (house, for example) at a fraction (let's say 5 to 10 percent) of the load rating. To isolate the load from the feeder, the compensator injects a VES (Variable-End Series) voltage. In order to achieve the required control aim, es may either maintain a constant voltage across the load (VL) while regulating the voltage on the feeder side (VF) or set the LSV (“Load Side Voltage”) to a specific value in order to manage the load's power consumption.

5.1.7 per Unit Reserve Calculation

In order to estimate reserves, the suggested framework combines bottom-up and top-down methods. The bottom-up method involves estimating the reserve per unit by taking feeder pros and topology into account, whereas the top-down method involves the procedure of load disaggregation at the bsp. Get the final 24-hour estimated absolute reserve by combining the two techniques' outputs.an example of a set of LV (k) feeders, each with n nodes, will be used to demonstrate the reserve computation. There are m distinct types of linked loads, or groups of homes, at each node. In great britain (GB), the secondary substation voltage is 11/0.433 kv or 6.6/0.433 kv, which is an 8.2% boost above the normal “phase-to-phase” voltage of the 400V [14]. This value sets the voltage at the feeder's commencement. In a study conducted in about the usage of o-load tap changers, it was found that fifty two percent of the secondary sub-stations have been kept at tap position 3, which is the nominal position, while 38% are kept below nominal and just 10% are kept above nominal. There is a 5% drop in nominal voltage at the lowest tap position 1. Given that the primary side's nominal voltage is 400 volts, the secondary side's minimum voltage might be 1.03 p.u. The main side of the secondary substation typically

has an average voltage of around 0.99 p.u. [14]. Most secondary substations will have a voltage among 1.07 & 1.02 p.u. at the feeder start.

The voltage at feeder end must be more than 0.94 p.u. [91], and consumers often see voltages around 1 p.u.

When the load is modest. Accordingly, we assume that the voltage at the feeder end ranges from 1-0.94 p.u.

To choose a sufficient number (let's say a thousand) of points from a normal distribution for the feeder start as well as feeder end voltage that match the given values, a monte carlo simulation is run. n nodes along the feeder yields 1000 distinct feeder profiles; n can be a large number, for example, 100. The value of (5.9) for a solitary feeder and (5.10) for the collective feeders corresponds to a unique feeder voltage profile.

$$r_i^j = \frac{\sum_{ii=1}^{n} P_{0i}\left(pz_i\left(\frac{v_{1+1}^2 - v_{min}^2}{v_{0\mathrm{it}}^2}\right) + pi_i\left(\frac{v_{\mathrm{u}} - v_{min}}{v_{\mathrm{tat}}}\right) + pp_i\right)}{n} \qquad (5.8 \& 5.9)$$

$$r_i = \frac{\sum_{j=1}^{k} r_i^j}{k}$$

In equations (5.8) and (5.9), for every iteration of the load category, the notional active power is denoted as p0i, the nominal voltage as v0ii, the real voltage as vii, and the zip model coefficients as ppi, pii, and pzi, respectively, are given. Equations (5.8) and (5.9) can be used to calculate the per unit reserve at secondary sub-station for any practicable voltage profile and load category throughout the feeders (5.9). Utilizing the recorded p, q, and v measurements from the previous year, we multiply the share of every load category (obtained by using ANN for load disaggregation) by the per unit reserve for that category in order to obtain the absolute reserve for every min of the day in the year. For every minute and load category, this yields a reserve matrix of order 1000 365, as seen in (5.10).).

$$[r\_i\ ]\_(1000\times365)=[r\_i\ ]\_(1000\times1)\times[p\text{^}agg\ p\_i\text{^}lc\ ]\_(1\times365) \qquad (5.10)$$

At any given moment in time, the most likely reserve for the i^{th} load category is the one with the greatest density (namely, mode) in the probability distribution of i^{th} matrix. The overall reserve is

obtained by adding together the most likely reserve values for every load categories that are taken into consideration, as shown in equation 5.11. Applying this procedure minute-by-minute yields the most likely 24-hour reserve pro le at the bsp, as well as 90% confidence upper and lower boundaries.

$$R = \sum_{i=1}^{m} Mo([R_i]_{1000\times365}) \tag{5.11}$$

The mode of the pdf is denoted by m o in (5.12). By substituting the current values for the recorded measurements, a 1000 1 reserve matrix may be formed for each minute, allowing for real-time reserve estimate to be performed in a similar fashion. The system will be provided with disaggregation via the use of historical data gathered at a substation operator with a certain degree of confidence and minimum and maximum reserve margins from that specific supply. You may plan various types of reserve based on the reserve that is projected using current measures. To keep things simple, we won't be considering the reverse power of via the feeder and will instead assume that each node has a comparable distribution of loads.

5.2 Load Disaggregation Validation Method

The crest (center for renewable energy systems technology) stochastic high resolution residential power demand model [87] is utilized to verify the load disaggregation approach. Using a mix of active occupancy pattern, ambient lighting conditions, daily activity profiles, and 35 regularly used domestic appliances in great Britain, this model develops a household power use bottom-up model of. You may customize it to your liking by picking the number of tenants, the day of the week, the month, and even the random distribution of home items. The total home load pro le is the result of adding together the demand profiles of all the appliances in the house. By running the demand model several times, we can get the individual load profiles of each residential customer. These profiles can then be combined to provide an average profile at the BSP, like secondary substation.

The demand model generates 200 customer load profiles, each consisting of the rated demand (the actual load attached to the network) for every client and the aggregated rated demand on BSP that takes into consideration the presence of different appliances. These profiles include every conceivable variation, including month, occupancy level, and more. According to the BSP, there are five distinct types of loads based on their voltage dependency. The following reasoning

underpins the categorization: (a) all appliances having pi=pp= 0, pz=1, and zero reactive power usage (qz=qi=qp=1)

(A) are classified as resistive type, (b) as smps, and (c) as ctim, while freezer type loads having a quadratic torque characteristics are classified as constant power type, and appliances with a 'constant active power component' (pp=1) are classified as constant power type.

Since lighting accounts for 14.5 percent of residential energy use, it is treated as a distinct load under qtim (d) (table 3.08).

Table c in appendix c displays the zip load model's coefficients, which are derived from [15]. Table 6.1 lists the zip load models for every load category, along with the usual appliances that fall within each category. In order to disaggregate loads, these five groups and their corresponding load models are taken into account. Each category's specifications are chosen according to the appliances that fall within that group. The zip parameters for load categories 1–4 are the mean values of the parameters for each individual appliance

According to the literature, all freezer models have the same requirements for load category 5, although vacuum cleaners have different ones. Load category 5 is thought to share zip properties with freezers because to the much larger load factor of freezer-type loads compared to vacuum cleaners. The typical UK household appliances that were considered for this research were highlighted by the Department of Energy and Climate Change (Decc) in their 2016 update of energy usage in the UK (ecuk) [10].The characteristics of the zip model for these appliances confirm, as in [15], that the percentage of loads depending on voltage is still substantial. A recent eld research [94] calculated the 'aggregate domestic load real power' exponent to be roughly 1.3, further supporting this. Voltage-controlled demand response reserve through CVR (Conservation Voltage Reduction) [95] will remain effective even with an increasing percentage of power electronic interfaced constant loads of power as more people become interested in implementing CVR for lowering power consumption using voltage control.

5.2.1 Rated Demand at BSP

Figure 6.4 shows the average values and ranges of the aggregate rated demand on BSP for 5 different types of loads. This information is derived from the crest stochastic demand model, which accounts for the yearly fluctuations of 200 client load profiles. The rated demand fluctuation is most pronounced for resistive (lc1) & lighting (lc3) loads. Demand at the bsp peaks about 6 o'clock in the evening, as predicted

Load Category	Load Model	Appliances
lc1:resistive	pz=1, pi=0, pp=0, qz=0, qi=0, qp=0	iron, hob, oven, kettle, small cooking, deswh(water heating), e-inst(water heating), electric shower, storage heaters, other electric space heating
lc2:smps	pz=0, pi=0, pp=1, qz=2.09, qi=-5.76, qp=4.67	answer machine, cassette/cd player, clock, cordless telephone, hi-fi, fax, pc, printer, tv(type 1/2/3), vcr/dvd, tv receiver box
lc3:lighting	pz=-0.01, pi=0.96, pp=0.05, qz=-0.1, qi=0.73, qp=0.37	compact fluorescent lamp
lc4:constant torque induction motor (ctim)	pz=0.69, pi=-0.47, pp=0.78, qz=10.76, qi=-19.38, qp=9.51	dish washer, tumble dryer, washing machine, washer dryer, microwave
lc5:quadratic torque induction motor (qtim)	pz=1.17, pi=-1.83, pp=1.66, qz=7.07, qi=-10.94, qp=4.87	chest freezer, fridge freezer, refrigerator, upright freezer, vacuum cleaner

Table 5.1: load categories for disaggregation at" BSP

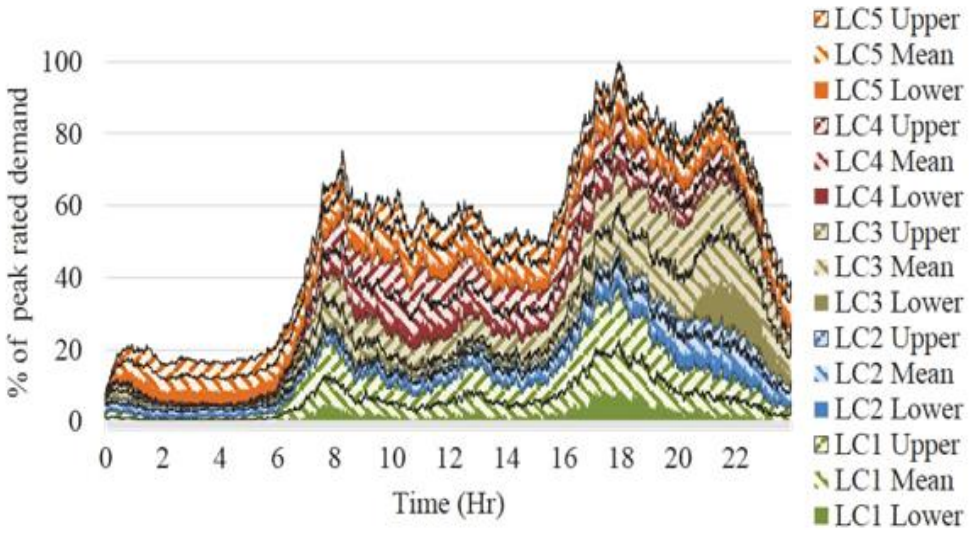

Fig 5.1: Change in the Rated Demand at the Bsp for Every Minute of the 5-Load Category

Figure 5.1 displays the values utilized in the base scenario, which nearly corresponds with Fig. 5.1. (a) & Figure 5.1(b) shows the error distribution against the base case and indicates that the most likely error is approximately 2.5 percent. This mistake is a natural byproduct of ANN training procedure and is not likely to be further decreased.

5.2.2 Scaled Rated Demand

While accurate, ANN training with recognized rated demand for every load category is currently impractical. It may be possible—though still challenging—to ascertain the pattern of change of the rated demand for every type of load rather than the exact quantity. Under such conditions, the load disaggregation accuracy is compared with the base case.

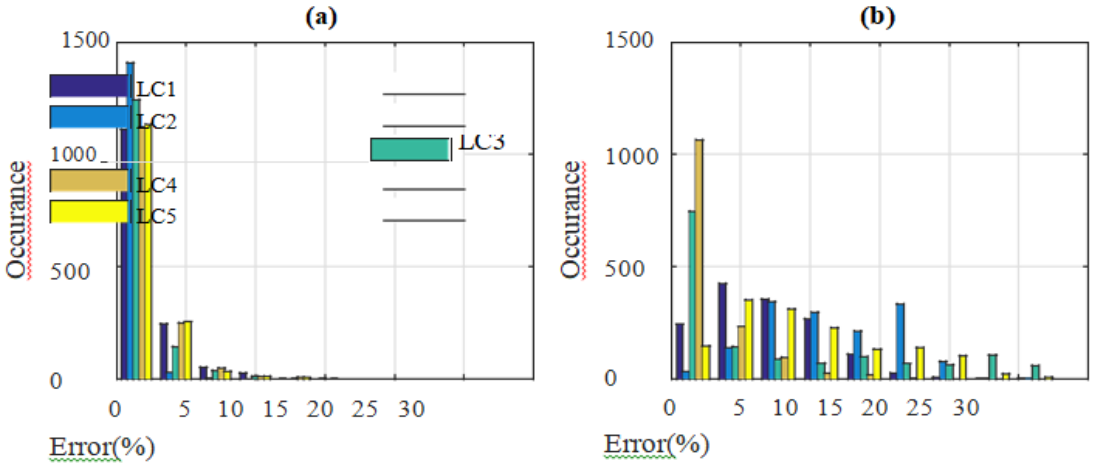

Figure 5.2: Error Distribution in the load disaggregation process according to (a) known rated demand (b) scaled rated demand

Figure 5.2 (a) displays the proportion of the rated demand that is actually there, as determined by the crest demand model. As seen in fig. 5.2 (b), these les are scaled randomly to alter the proportion share of every load category once every min while maintaining the pattern over a 24-hour period.

The scaled rated demand proto logue is used to train the ANN using the same method as for known rated demand. Utilizing the identical set of p, q, and v values as in figure. 5.3(c), the load on BSP has been divided into five load categories, as seen in figure 5.3 (a). Comparison with the base case reveals some

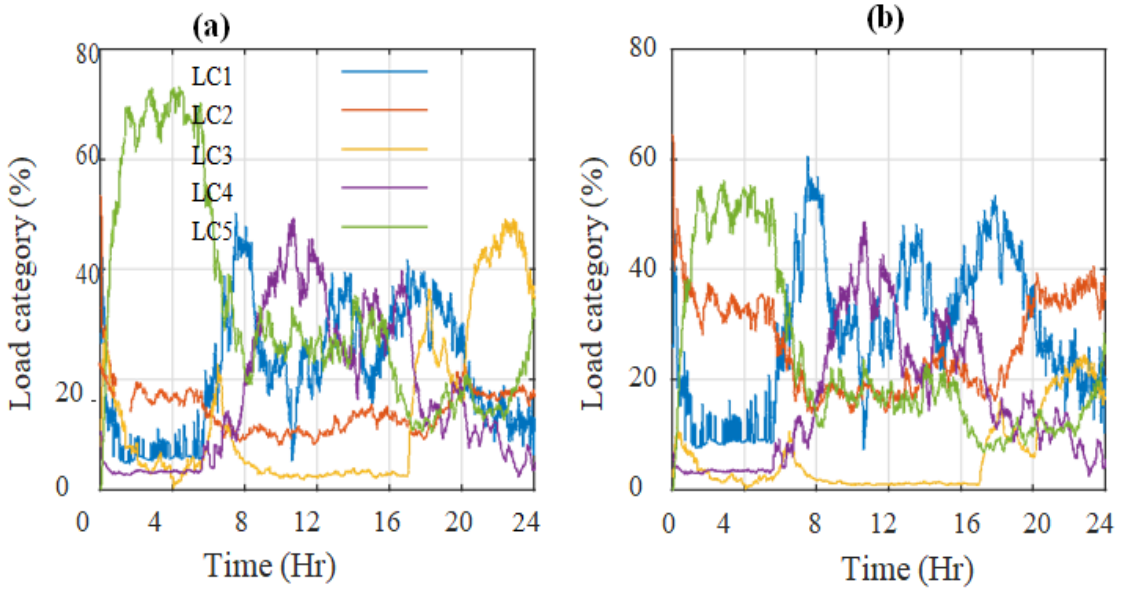

Figure 5.3: Individual load category's percentage share (a) before to scaling (b) Following scaling

discrepancies in particular for SMPS-type loads (lc2) in the late evening. Figure 5.3(b) shows the distribution of error, which, aside from lc2, indicates that it is primarily contained within ten percent.

5.2.3 Random Rated Demand

In actuality, the rated demand at the BSP for each load category would be unidentified. As a result, the uncertainty surrounding the quantity of loads connected and the accompanying voltages would need to be handled by the load disaggregation. Consequently, a huge amount of data containing all conceivable combinations of p, q, and v should be used to thoroughly train the ANN using the technique covered in section 5.1.3. In this way, the trained ANN would be able to infer load sharing values under the given operational circumstances.

The weighting variables and number of random voltage samples applied to train the ANN are n_w=40 and n_v=40, respectively. 17 static-motor type load combinations must be taken into account because the crest demand pro le indicates that the share of "motor-type load" (lc4 and lc5) varies from 5 - 85 percent (and static-type load from 95 percent - 15 percent). As a consequence, 27200 (=40 40 17) data sets were produced for training. The trained neural network receives the set of p, q, and v values from the base case, which yields the disaggregated load profiles depicted in Figure 5.4 (d). Except for lc3 and lc4, the mistake in load disaggregation (revealed in figure 5.4(b)) is mainly restricted to fifteen %. It is not surprising that load disaggregation with random rated demand performs less accurately than with known or scaled rated demand. The reserve estimation, which also takes into account the voltage sensitivity of every load category along with profile of the voltage across the feeders, does not, however, explicitly account for this degree of uncertainty.

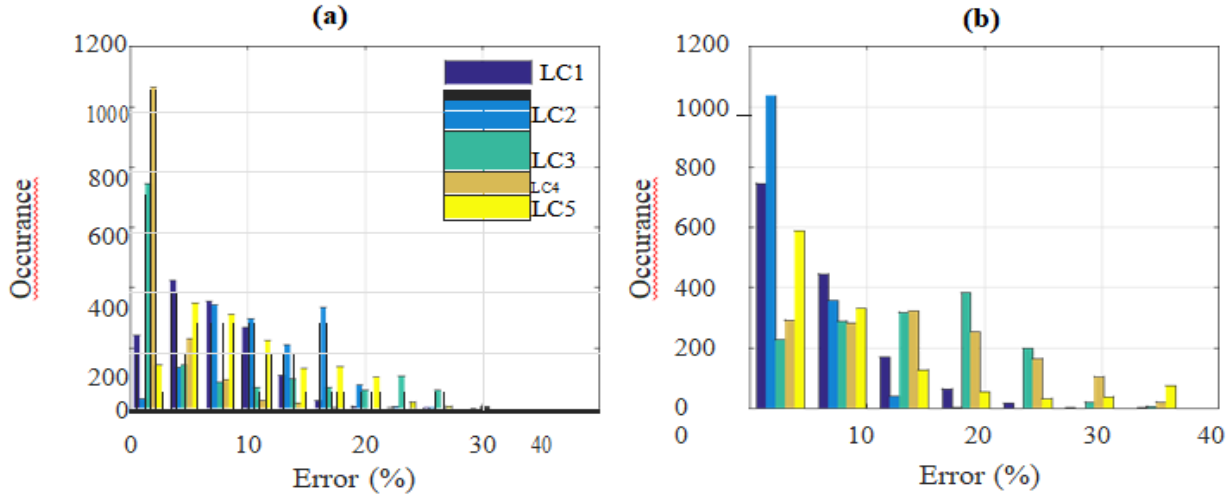

Figure 5.4: Error distribution in load disaggregation on the basis of (a) Scaled rated demand (b) Random rated demand

As stated in section 5.4., a validation could be carried out with either known les like crest or random data that is comparable to the training process. An indicator of the quality of the ANN training is provided in both scenarios by the error among the output matrix (otst) & target matrix (ttst). To provide an understanding of the range of most likely errors, error for every lcpe (load category) is shown as histogram plots in fig. 6.10. The validation with random dataset having the most probable error for every load category being under 5% is shown in Figure 5.5(b). For a few load categories, the mistakes are more evenly distributed, with more than 15 percent, in Figure 5.5(a) (validation using Crest Pro Le). The findings highlight the possibility of optimistic outcomes from validation using a random dataset.

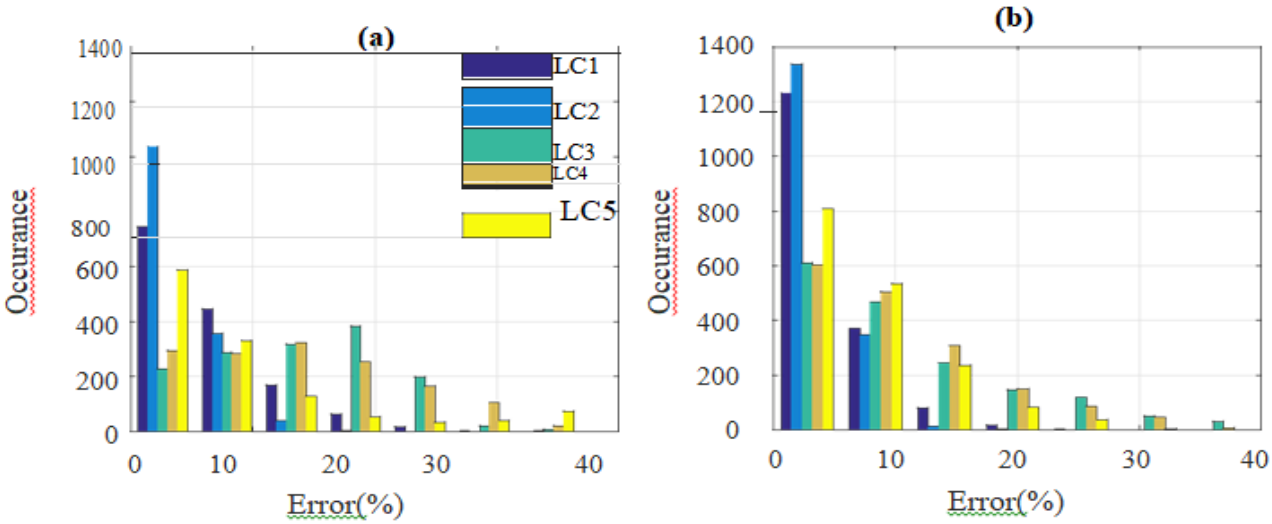

Figure 5.5: ANN validation with (a) known pro le from crest b) Random pro less similar to process of training

5.3 Case Study on Reserve Estimation

The aggregate reserve estimate technique is presented in this part and is validated in Section 6.2 after being used in a real-world case study in the domestic sector of Great Britain. Furthermore, a conventional IEEE distribution network with real voltage profiles is used to validate the confidence boundaries on the estimated reserve.

5.3.1 & 5.4 Reserves at the BSP for Domestic Sector & Conclusion

For the purpose of constructing load profiles for 200 homes, Crest's stochastic higher resolution domestic electricity demand model [87] is utilized. These load profiles are then integrated in order to create the active along with the reactive power profiles at the base station point. Using a known share from each load type and a resolution of one minute, this is done independently for each month of the year, taking into account both weekdays and weekends (presented in table 5.1). Fig. 5.11 demonstrates the reserve at BSP, which is calculated utilizing the procedures described in section 5.1.7. In Figure 5.11, the load share from Ann is represented by pre x \es", and the actual reserve from known share of each load category is marked with pre x \ac". With the 90 percent upper/lower confidence boundaries (ub/lb), Figure 5.11(a) displays the most likely (mp) reserve available on secondary substation. Around 6 p.m., when the system reaches its highest reserve

Chapter 6

Results & Analysis

The figure 6.1 shows the result of creating a microgrid scenario with 3 inverter-based generators, 2 loads, and the suggested pqvi controller to illustrate how effective it is. Connection switches are located at each load's input, each inverter's output, and the connection point with the main grid. There is a dedicated lqr-ort controller and auxiliary control loops for every inverter.

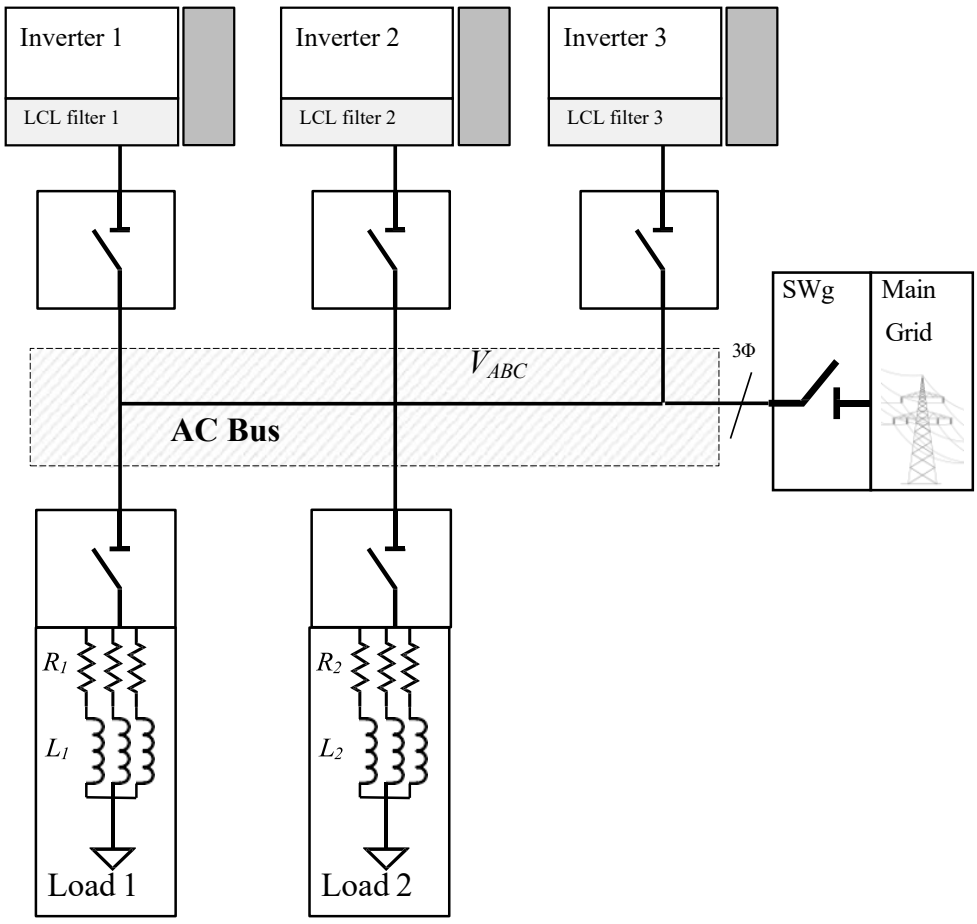

Fig. 6.1. Complete Islanded Microgrid scheme with RL loads

6.1 Microgrid Model

In table 3 we can see a summary of the experimental parameters. All inverters had their component values input into (66) to get the microgrid model in grid-connected mode. The shannon sampling theory [90] established a sampling frequency of 10 khz. The 17-th order equivalent to 1,020 hz may be controlled by this controller with this option. Through the use of

integrators, the three models were discretized (73). One model was generated for each inverter, leading to a total of three separate models. Quantitative worth. With grid-connected mode, each model is revealed in appendix b.1. Appendix c.1 contains the matlab

parameter	symbol	value
grid frequency	$f\ (\omega_c)$	$60Hz$ (376.99 rad/s)
dc bus voltage	V_{dc}	$350V$
grid voltage	V	$120V_{RMS}$
output inductance	L_o1, L_o2, L_o3	$1.8mH$, $1.8mH$, $3.6mH$
input inductance	L_i1, L_i2, L_i3	$1.8mH$, $5.4mH$, $3.6mH$
filter capacitance	C_1, C_2, C_3	$8.8\mu F$
pwm frequency	f_{PWM}	$10kHz$
sampling period	T_s	$100\mu s$
load 1	R_1, L_1	85.7ω, $0.46H$
load 2	R_1, L_1	171.43ω, $0.53H$
error weighting matrix	Q_p1, Q_p2, Q_p3	$\{5, 4.9, 4.8\} \times 10^3 \times I_{2\times2}$
input weighting matrix	R_p1, R_p2, R_p3	$\{0.2, 0.15, 0.18\} \times I_{2\times2}$
inner integrator gain	K_i1, K_i2, K_i3	1
outer integrator gain	K_s1, K_s2, K_s3	5
sogi gain	K_{SG}	0.7
pll proportional gain	K_{pP}	0.28307
pll integral gain	K_{iP}	7.5102
frequency restoration gain	K_f	100
power rating	S_1, S_2, S_3	500, 1000, 1500 VA
voltage restoration gain (active)	K_p1, K_p2, K_p3	1000, 2000, 3000
voltage restoration gain (reactive)	K_q1, K_q2, K_q3	$-1000, -2000, -3000$

Table 6.1 Specifications of parameter for the lqr-ort controller

By combining the grid-connected models and applying equations (76) & (77), the full microgrid model in island-mode was derived. With 3 generators sharing a similar rl load, the resultant model for 1 phase of islanded microgrid is shown in (100). Using the formula in appendix a, this model was converted to the dq frame [83]. The model was discretized after evaluating the values of component from table 3. Adding to the discretized model was the final stage. Employing integrators. A state-space system having 6 inputs, 6 outputs, & twenty-four states was the end result.

Appendix b.2 contains the numerical values for the generated islanded microgrid model

6.2 Stability & Robustness Analysis for the Proposed Model

The grid-connected along with the islanded models žg(s) and () from section 3.2 were subjected to the stability and robustness evaluations given in section 3.2 in equations (79) and (80), respectively. The LCL filter components were considered to be doubtful in these studies since they varied uniformly by 30 percent about the nominal parameter values revealed in table 3. Research on stability analysis for v-i or main control often involves tweaking a single parameter at the time and tracking how the placement of the eigenvalues changes [28], [31], [55], [91]-[93]. The more conservative idea of robustness and stability is obtained by analyzing random fluctuations in components all at once. As a result, using modifications in the parameters, 20 examples of each µg() and () were generated. The results of the load and component variations are shown in table 4. Appendix c.2 provides the matlab algorithms used in the stability and robustness investigation.

#											
unit										°	
nom	8.8	1.8	1.8	8.8	5.4	1.8	8.8	3.6	3.6	85.7	0.46
1	10.46	1.29	2.29	9.62	3.97	1.30	6.36	2.89	3.06	100.04	0.44
2	10.94	2.06	2.25	6.35	5.99	1.87	10.83	3.36	3.15	81.76	0.35
3	6.83	1.80	1.32	10.64	3.92	2.21	10.98	4.32	3.85	64.66	0.49
4	10.98	1.78	2.06	11.09	4.01	1.98	10.36	4.26	3.09	73.69	0.45
5	9.50	2.24	1.55	9.74	5.47	1.47	6.68	2.65	4.30	67.89	0.51
6	6.68	1.92	1.72	10.16	4.09	1.66	7.54	3.38	4.64	74.44	0.52
7	7.63	1.93	1.85	10.08	6.43	1.76	7.93	3.66	4.10	82.62	0.50
8	9.05	2.19	2.28	8.23	6.43	2.32	9.75	3.42	3.26	87.10	0.33
9	11.22	2.13	1.71	9.62	6.12	1.43	6.88	3.94	3.78	83.51	0.34
10	11.25	1.88	2.32	7.06	4.27	2.18	9.97	3.88	2.75	105.00	0.41
11	6.99	1.46	1.59	9.89	5.92	1.96	6.72	3.15	4.48	86.63	0.47
12	11.28	1.52	2.02	6.33	5.46	1.67	9.61	3.45	4.42	108.51	0.50
13	11.21	2.22	1.98	7.62	6.93	1.47	8.77	2.55	4.29	92.78	0.43
14	8.72	1.29	1.84	6.40	5.88	1.72	10.27	4.65	3.08	109.23	0.55
15	10.39	1.79	2.01	6.67	6.37	1.78	9.94	2.88	3.80	72.37	0.52
16	6.91	1.44	1.98	10.51	5.25	1.39	10.93	2.75	2.57	94.76	0.59
17	8.39	2.32	1.45	9.83	5.18	1.90	10.86	3.32	3.44	74.85	0.47
18	11.00	2.03	1.40	7.83	6.45	1.50	7.92	2.95	3.20	94.53	0.41
19	10.34	1.80	2.34	11.18	4.05	1.68	9.85	3.58	2.87	95.73	0.35
20	11.23	1.77	1.44	6.34	4.21	1.89	7.20	3.25	2.91	63.49	0.49

Table 6.2. Variations in components for examination of stability and robustness

6.2.1 Grid Connected Models

The open-loop eigenvalues of the nominal 1( ), 2( ), and 3( ) are shown in figure 6.2, along with their variations. Every single inverter is stable when operating in grid-connected mode without the need for a controller. This is due to the fact that the eigenvalues remains in the unit circle, as can be seen in the magnified image. But none of an open-loop models that used unit feedback were found to be closed-loop stable after looking at stability margins.

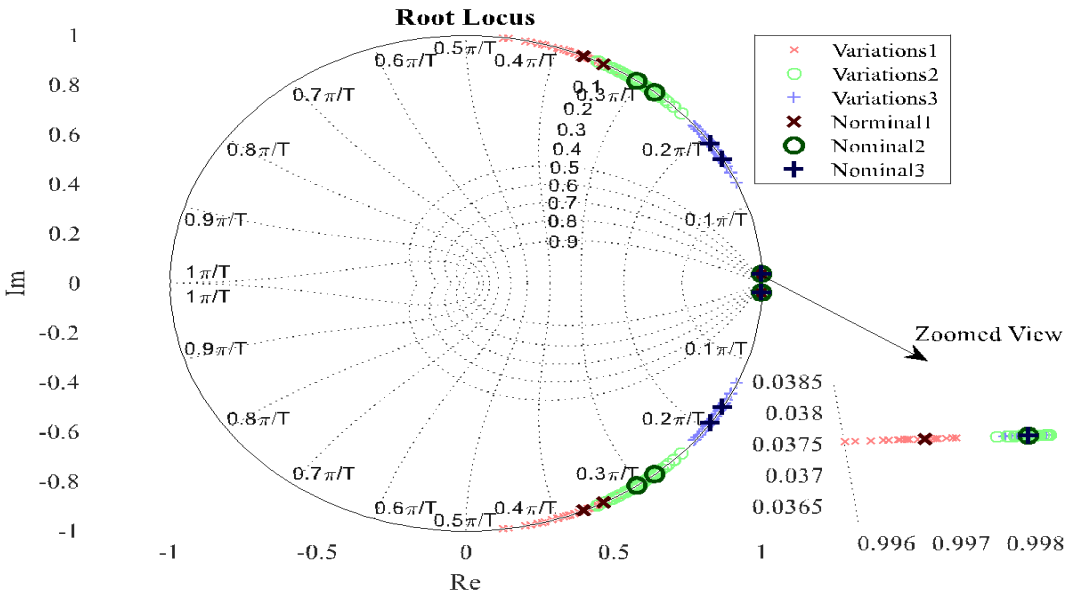

Fig. 6.2. Eigenvalues of nominal transfer function Model and their variations

One-shot calculus figure 6.3 displays the nominals 1( ), 2( ), and 3( ) together with their variants. These schematics show that inverters 2 and 3 have comparable frequency responses, differing only in the range of frequencies at which they resonate and crossover. There are three inverters; inverter 1 having the quickest dynamics, inverters 2 & 3, in that order

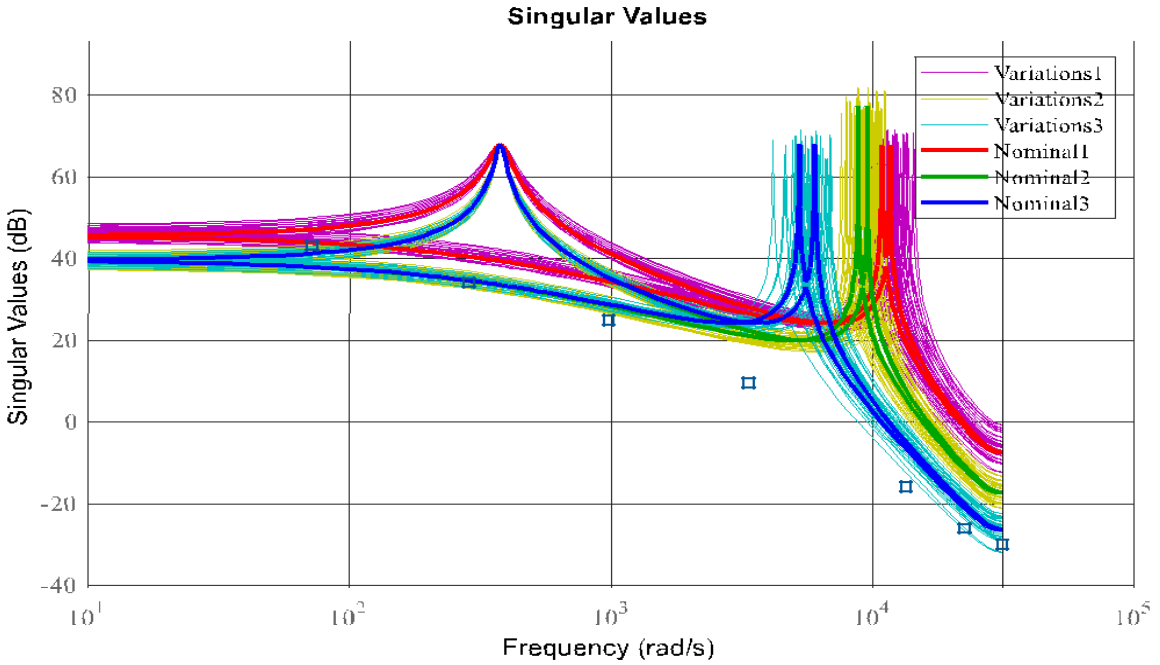

Fig. 6.3. Singular values diagram for state Space model and **their variations**

6.2.2 Islanded Microgrid Model

The figure 6.4 displays the “open-loop eigenvalues” of the function and its variants. If an open-loop microgrid is operating in grid-connected mode without the controller, then the fact that all of the eigen-values remain into the unit circle is evidence of the microgrid's stability. Nevertheless, not a single one of the open-loop models is stable in a closed-loop setting with unit feedback after taking stability margins into consideration. This brings us to the conclusion that Fig. 6.4 displays singular value diagrams that reflect the nominal and its variations. When compared to fig. 6.5, these diagrams reveal comparable behavior. A response associated with the rl load, however, exists below 0 db.

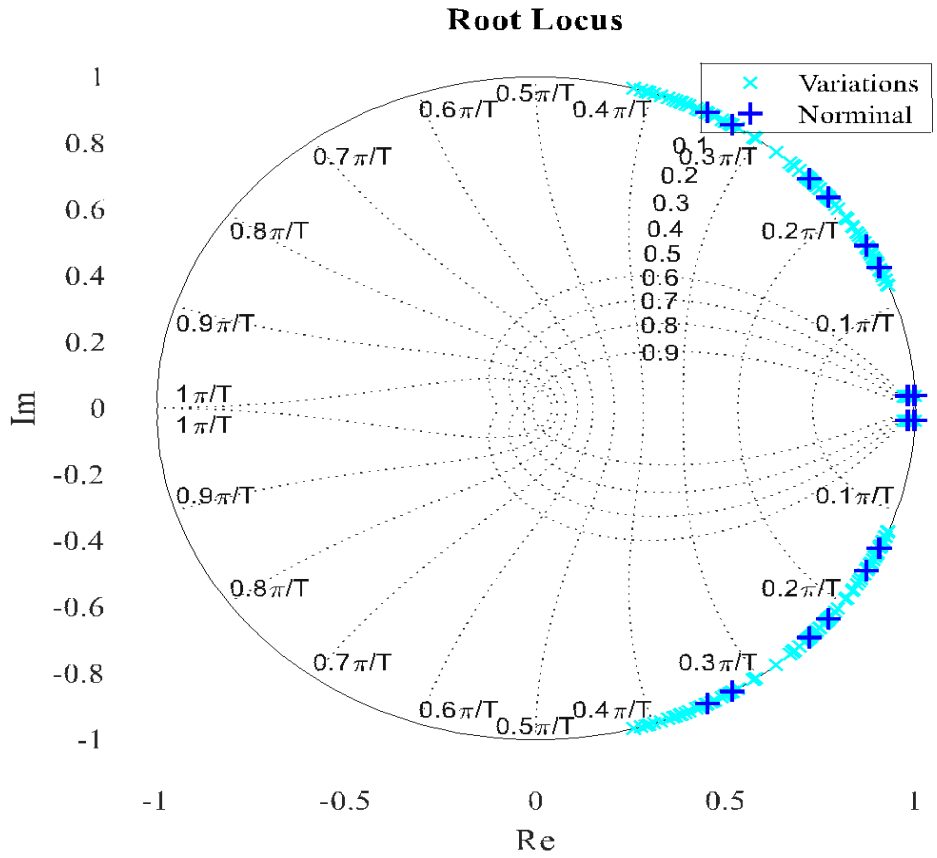

Fig. 6.4 Eigenvalues of nominal transfer function and its variations

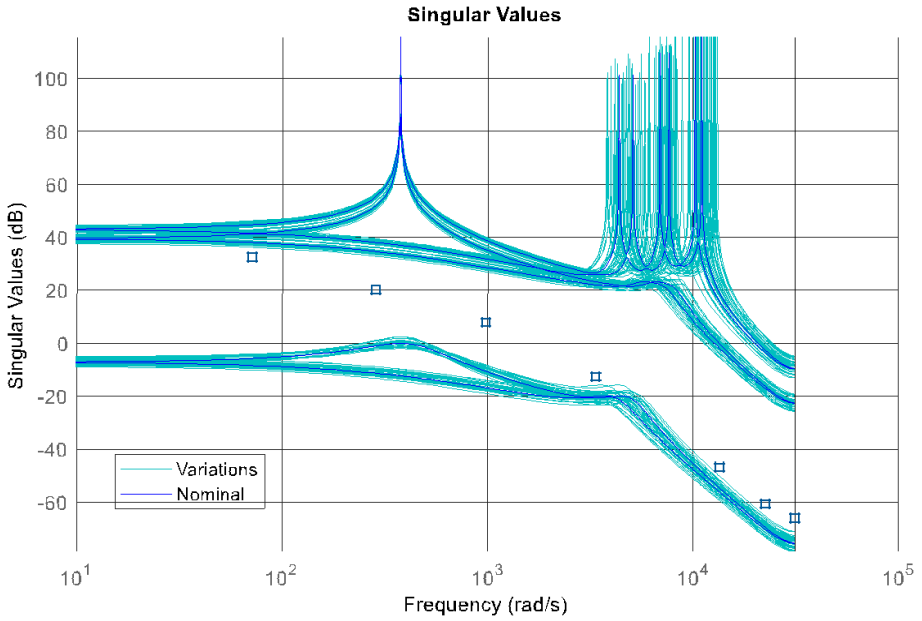

Fig. 6.5. Diagram of singular values for G(s) and its variations

6.3 Open-Loop Models Validation

In grid-connected as well as island modes, the models were verified. Under the identical input signal, the responses of each mathematical model's equivalent circuit were compared to those of the state vectors and output power of models. Lastly, to measure the disparity between the "mathematical" model and the equivalent circuit, the nrmse, as specified in equation (81) was calculated for every model.

6.3.1 Grid-Connected Inverter Model

In order to evaluate the "mode in grid-connected mode, the circuit depicted in figure 6.6 has been simulated with the help of the artemis library for the power electronics devices that is offered by opal-rt technologies TM [2].This library's mathematical solver performs precise simulations of the power electronics components, like the igbt transistors found in 3-phase inverters. The values of the inverter 1 LCL component have been utilised to evaluate the mathematical model (66). Following the validation of the inverter 1 model, it was believed that (66) would enough to describe the dynamics of any grid-connected inverter, including inverters 2 or 3.

Starting with the identical nominal amplitude and phase, the main grid voltage as well as inverter output voltage are both used in this experiment. After reaching a high of 240√2 at = 0.025 s, the inverter o/p amplitude has been reset to its previous value at = 0.035 s. The values of reactive & active power for the mathematical model & circuit are shown in fig. 6.7. Waveforms of the state vectors in both the dq & abc frames are shown in figure 6.7. Figure 6.5 shows, from a zoomed perspective, that the dynamics of active along with the reactive power in the mathematical model as well as circuit are identical. But the circuit's power goes through little oscillations at high frequencies. The 10 khz switching frequency of the igbt transistors is responsible for generating these oscillations. Current switching oscillations in the input inductor may also be seen in zomed views in fig. Nonetheless, both the steady-state and transient-response states of state vector dynamics exhibit comparable behavior.

We also looked at the shared power & state vector's nrmse value in dq frame. With the exception of the input inductor current, which has a fitting value of around 78% on the d component, all other state variables have fitting values over 95% (fig. 48). This is because the pwm signal contains switching noise at 10 kHz. Which is not considered in the suggested model. The predicted model for grid-connected inverters is proven correct by these outcomes.

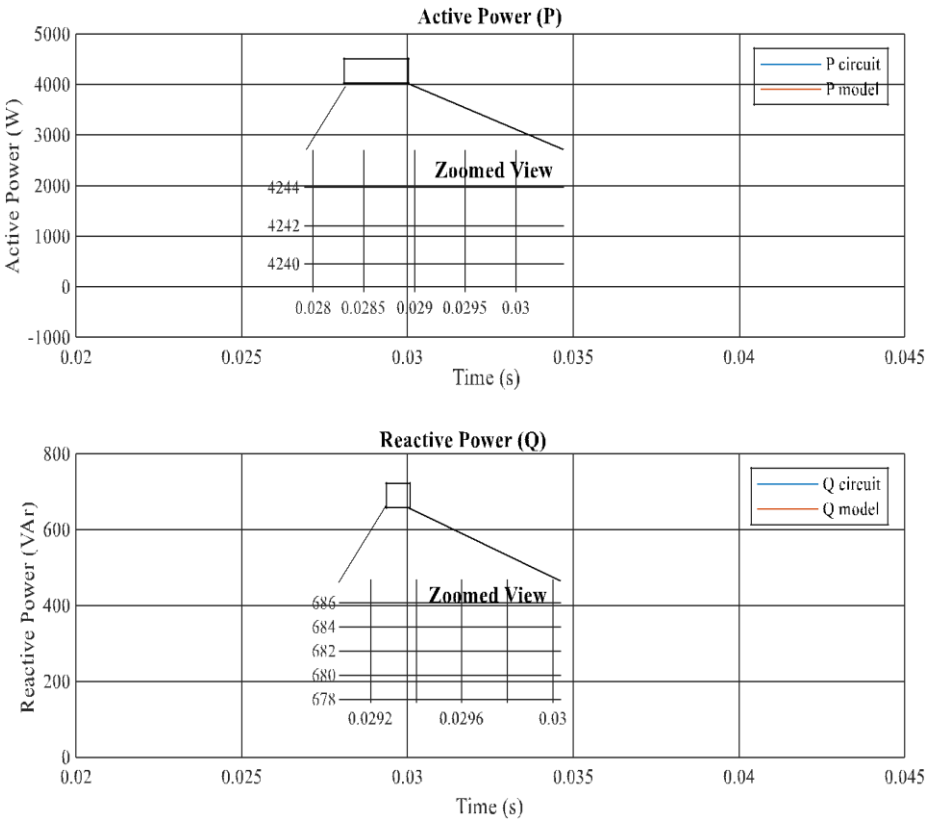

Fig. 6.6. Power wave forms for the mathematical model and circuit in grid connected Mode Top: active power. Bottom: Reactive power

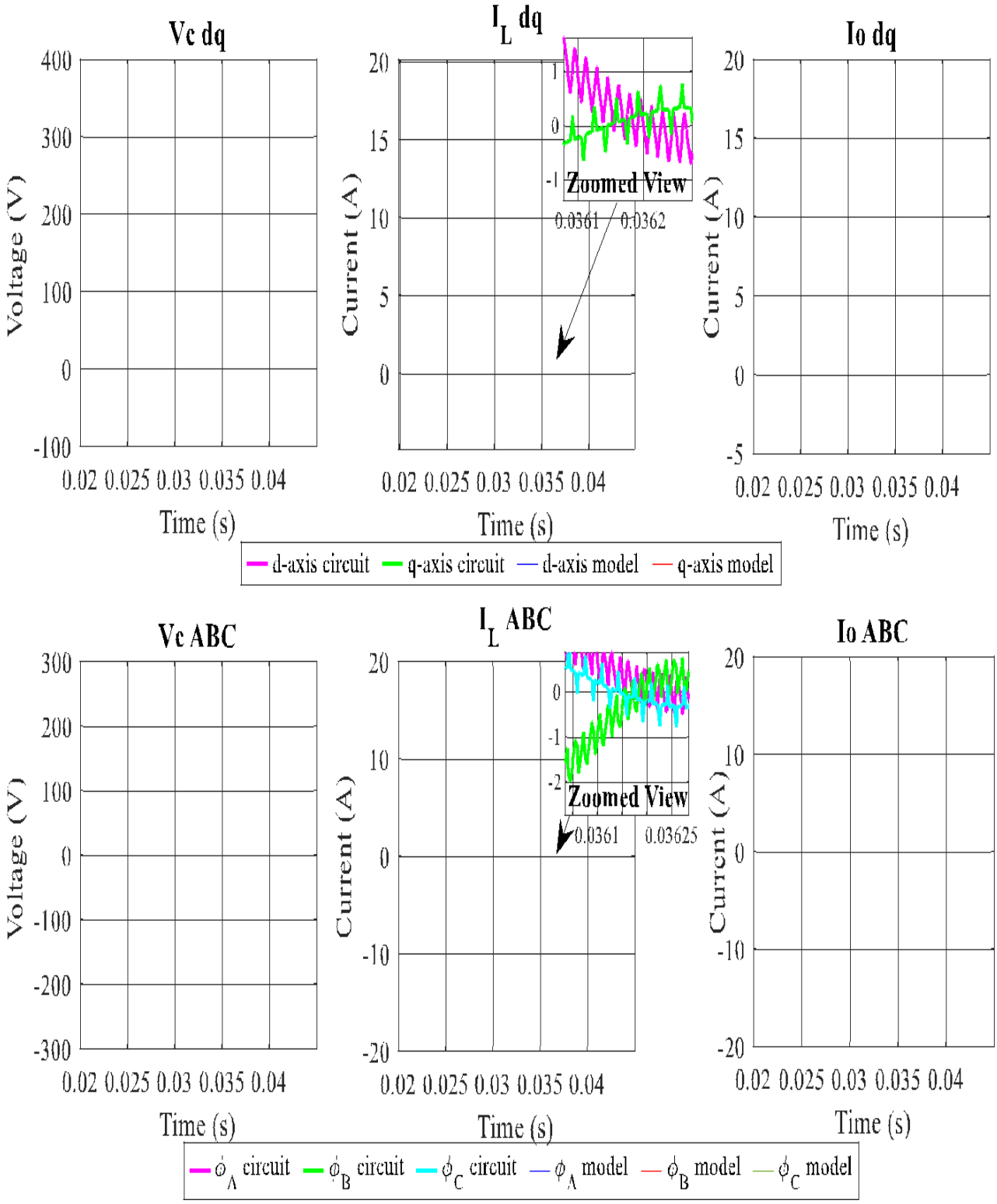

Fig. 6.7. State-vector waveforms for the mathematical model and circuit in grid-connected mode. Top: *dq* frame. Bottom: *abc* frame

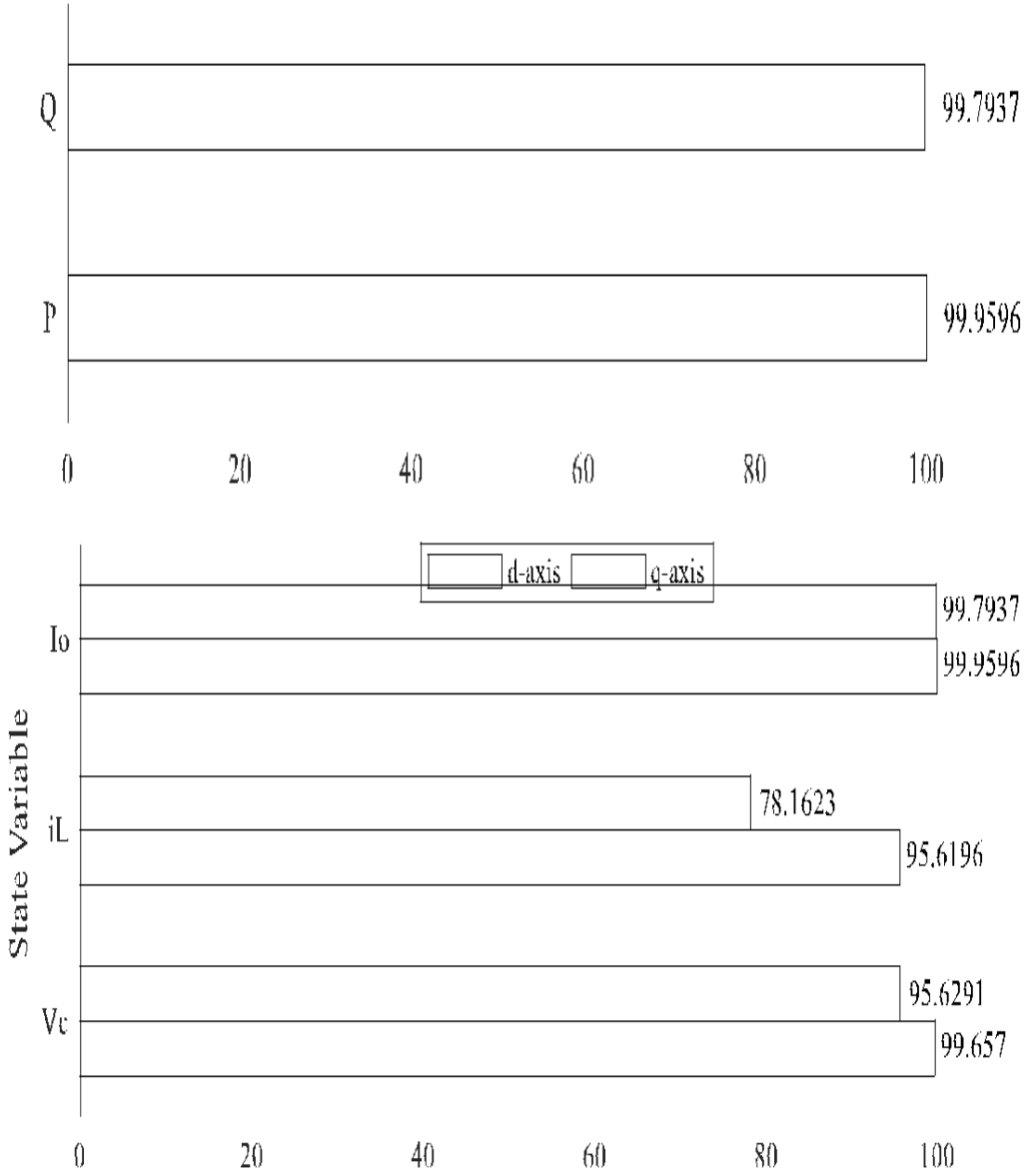

Fig. 6.8. NRMSE for the state vector and shared power.
Top: state variables. Bottom: active and reactive power

6.3.2 Islanded Microgrid Model

The artemis library for “power electronics devices” was used to simulate the circuit seen in Figure 6.9 for islanded mode [2]. The values of the LCL components in Table 3 were utilised to confirm the mathematical model (77). The 3 inverters' output voltages and the main grid's initial nominal phase and amplitude were the same for this experiment. The output amplitude of the inverter was duplicated at = 0.025 s, reaching a peak value of the 240√2, and then it reverted to its initial value at t=0.035 s. The mathematical model and circuit's reactive and active power

waveforms are displayed in Fig. 6.10. Fig. 6.11 displays state vector waveforms in dq frame, while Figure 6.12 displays them in abc frame. Both the mathematical model and the circuit's reactive and active power dynamics are similar. Zoomed images provide more clarity on the switching oscillations seen in input inductor currents. The 10 kHz frequency at which the igbt transistors switch is what's causing these oscillations. State vector dynamics, however, exhibit comparable behavior in both steady state along with transient response conditions.

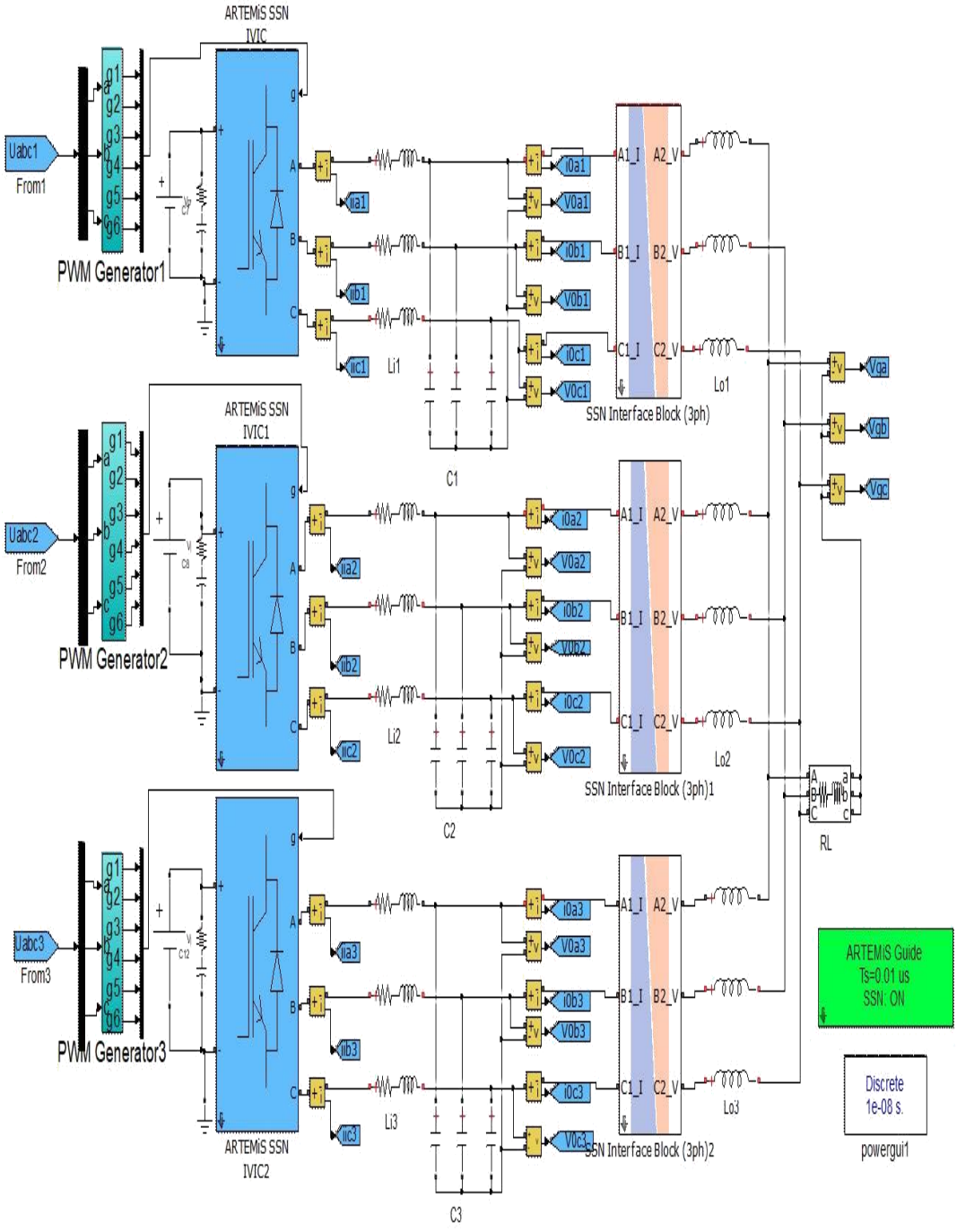

Fig. 6.9. Circuit diagram for islanded mode model validation

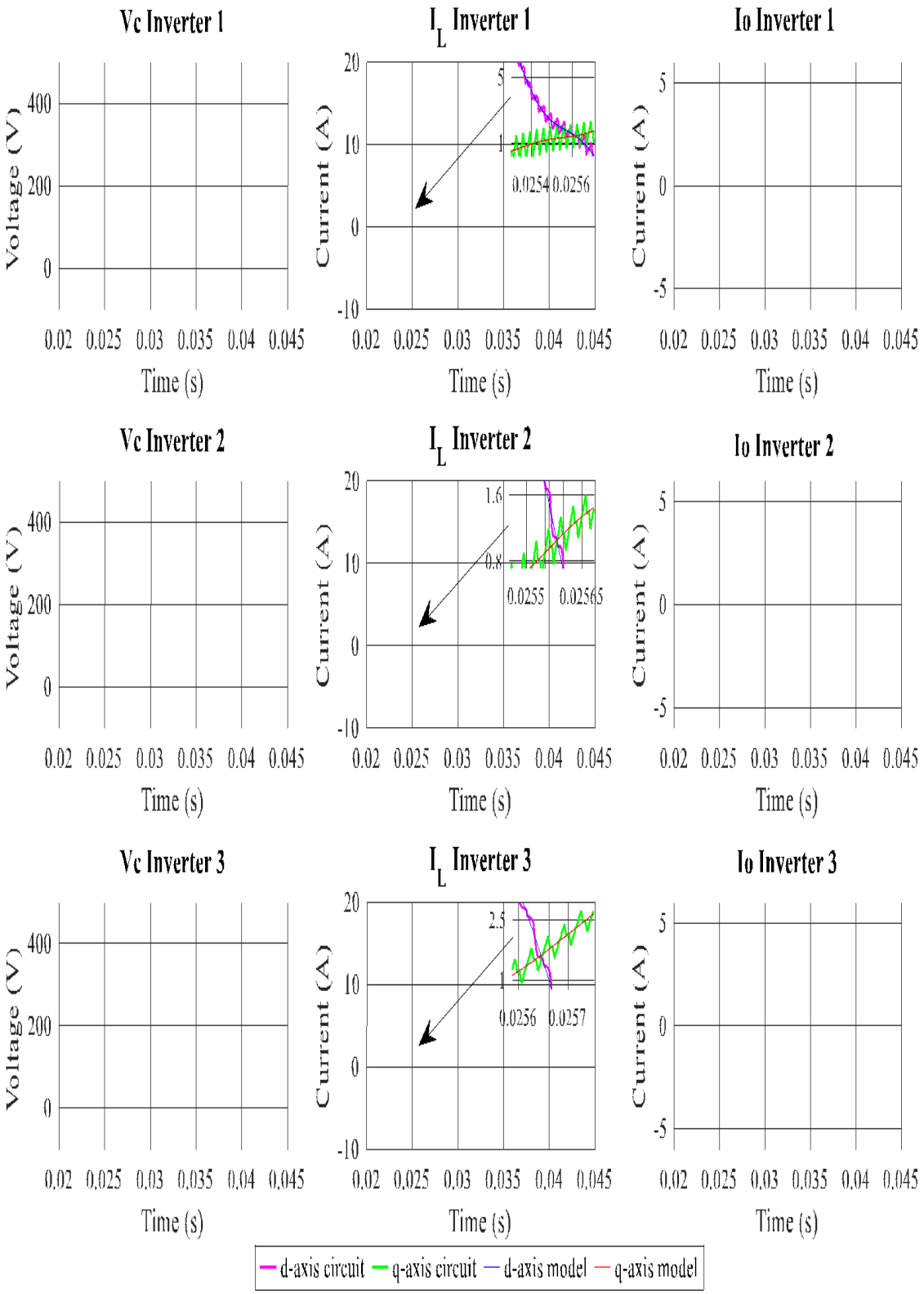

Fig. 6.10. Power waveforms for the mathematical model and circuit in islanded mode. Top: inverter1. Middle: inverter 2. Bottom: inverter 3

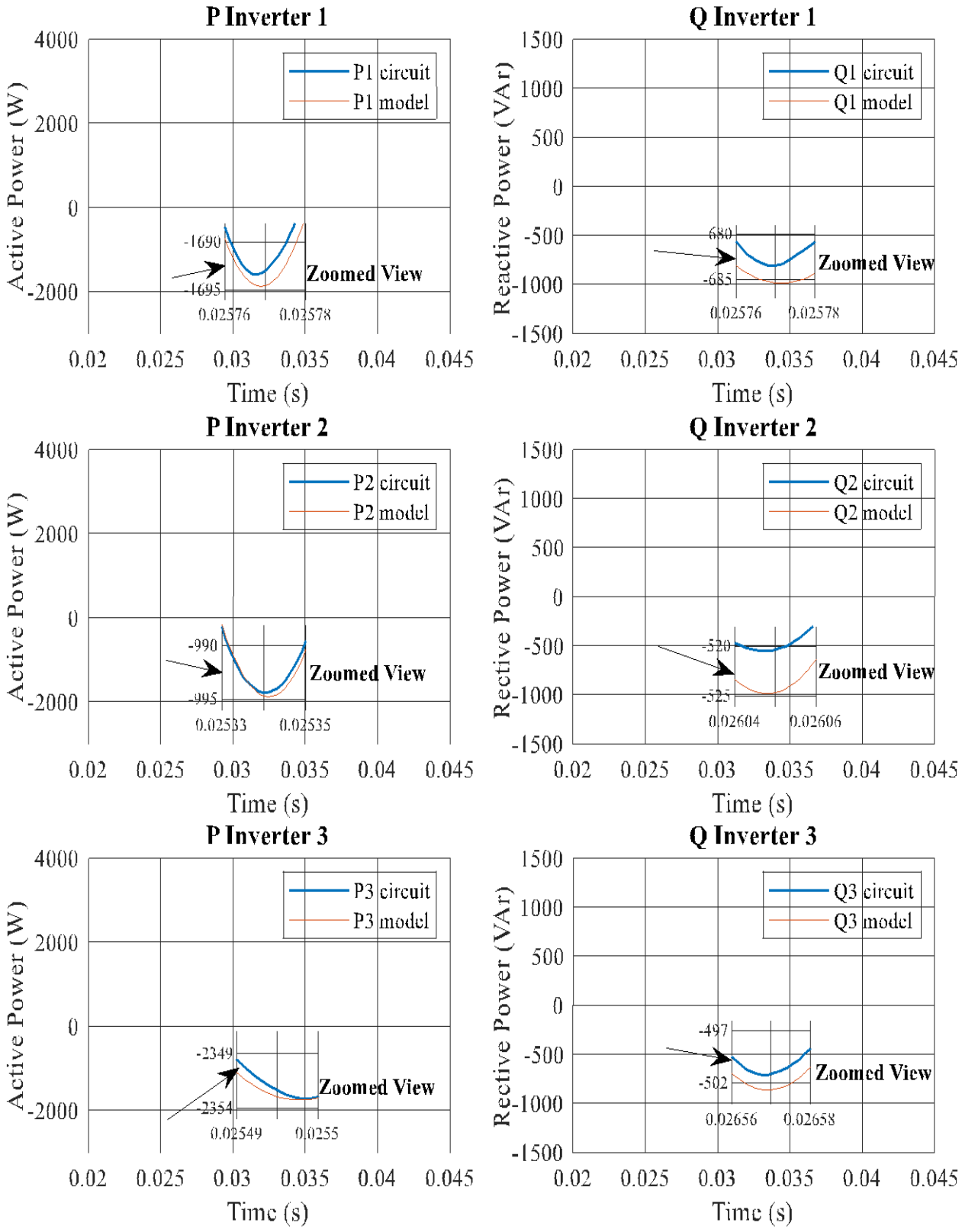

Fig. 6.11. State-vector waveforms for the mathematical model and circuit in islanded mode in the *dq* frame. Top: inverter 1. Middle:inverter 2 bottom: inverter 3

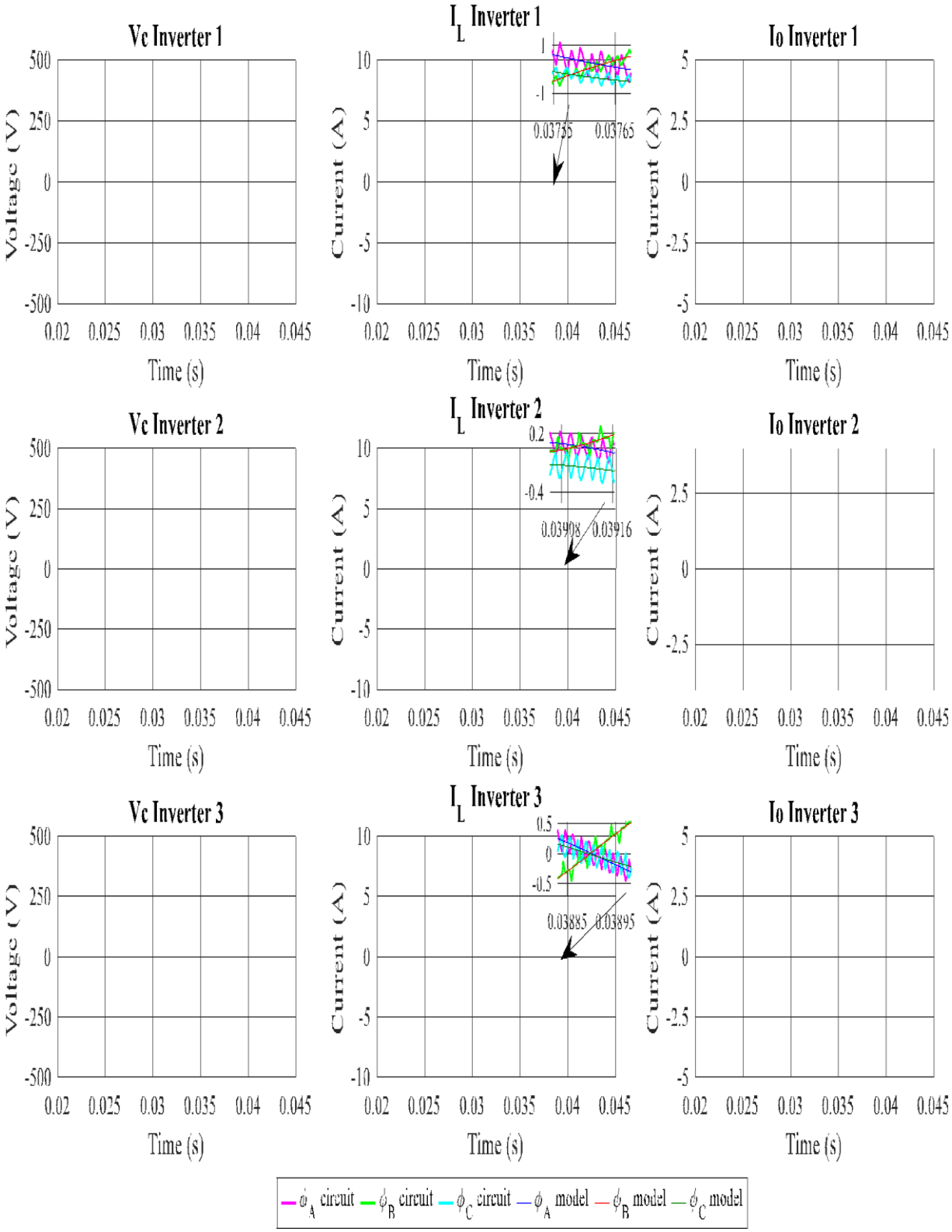

Fig. 6.12. State-vector waveforms in the *ABC* frame for the circuit in islanded mode and the mathematical model. Top: Inverter 1. Middle: Inverter 2 Bottom: Inverter 3

We also looked at the state vector's as well as shared power nrmse value in the dq frame. Figure 6.13 indicates that, with the exception of input inductor currents, all state variables have fitting values greater than 98%. Which are reduced since 10 kHz pwm switching is present. This is not considered in the suggested model. These findings confirm that the island microgrid concept is correct.

We also looked at the shared power as well as state vector's nrmse value in the dq frame. With the exception of the input inductor current, which has a fitting value of around 78% on the d component, all other state variables have fitting values over 95% (fig. 48). This is because the pwm signal contains switching noise at 10khz. This is not considered in the suggested model. The predicted model for grid-connected inverters is proven correct by these outcomes.

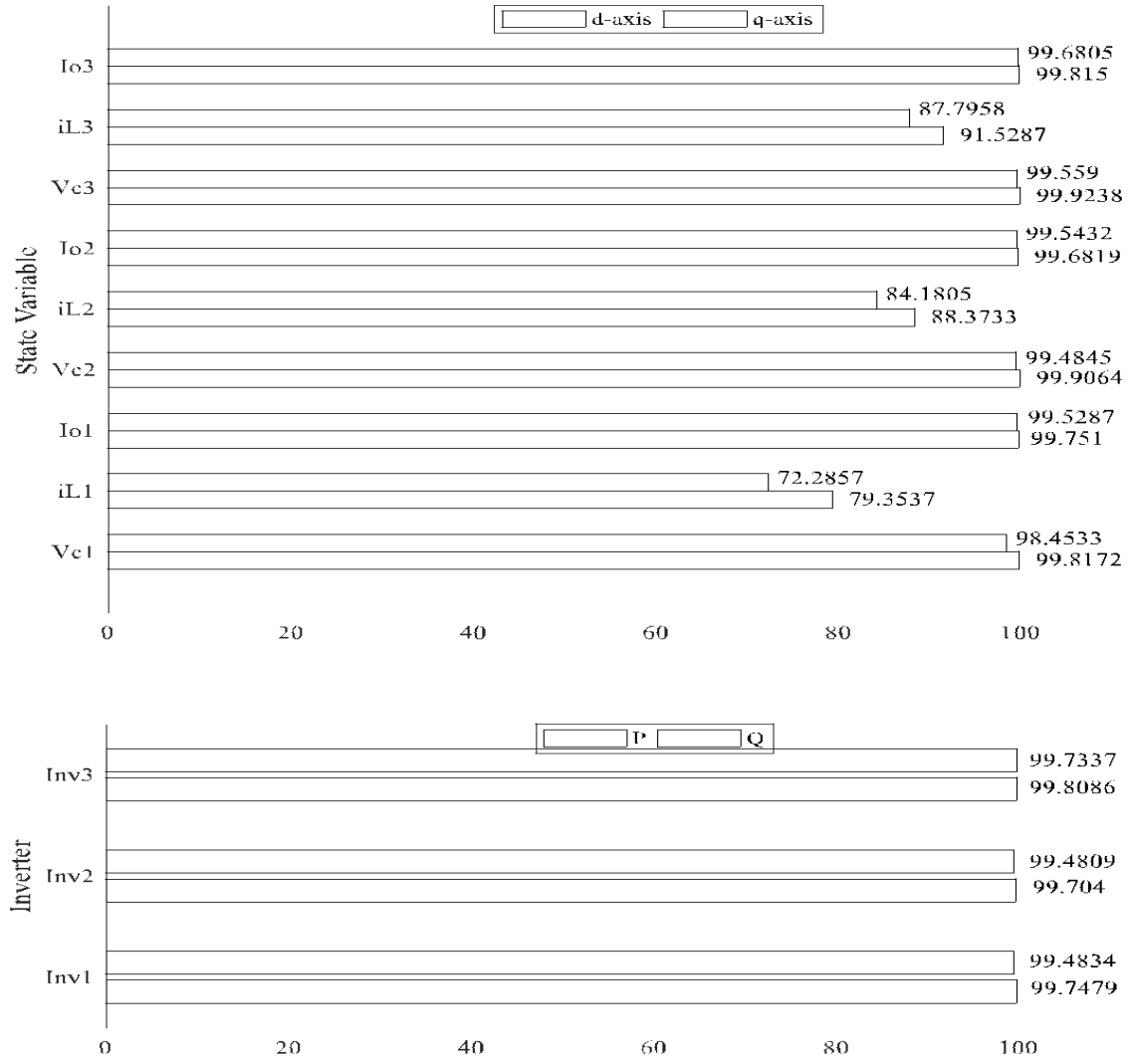

Fig. 6.13. NRMSE for the shared power and state vector.
Top: State Variables. Bottom: Active and Reactive Power

6.4 Controller Implementation & Validation

The lqr-ort controller was obtained by selecting the weighting matrices from table 3. The design requirements may be found in section 3.5, which informed the selection of the weighting matrix values. A damped response free of oscillations and a settling time under half a second were also necessary. Matrixes 1, 2, and 3 representing control feedback were calculated using equations (85) and (86). First, two, and three matrices were generated byon every inverter, which is 88. In appendix b, you can see the numerical values of the control matrices.1. Appendix c.1.2 has the matlab scripts used to compute controllers. Appendix d contains the simulink block presentations for grid-connected and the islanded mode control. Table 3 displays further loop gains. A modest enough outer integrator gain was chosen so that it would not impact stability margins or transient responsiveness. To achieve steady state in under 0.3s, modified pll-sogi improvements were necessary. Reason being, whether connected to the grid or not, inverters must remain in sync with the ac bus at all times. Therefore, it typicallyto zero, while in island mode, the frequency consistently approaches 60 hz.each inverter's power rating informed the selection of voltage restoration improvements. Keep in mind that inverters 1, 2, and 3 have powers of 500 1000 & 1500va, respectively. Thus, in order to provide proportional power sharing, 2 must replicate 1, and 3 must triple 1. Also, the ac bus voltage has to be restored in under three-hundredths of a second.

6.5 Stability & Robustness Analysis of the Suggested LQR-ORT Controller

The controlled grid-connected along with the islanded models λ ( ) and λμg( ), displayed in section 3.5, were subjected to the robustness and stability assessments described in section 3.2. Table 3 shows the components in LCL filters that have been designated as uncertain elements for these studies. These components had a consistent fluctuation of 30 percent about nominal parameter values. Consequently, based on parameter modifications, 20 instances of each λμg( ) and λ ( ) were generated. Appendix C.2 contains the Matlab routines for the stability and robustness analysis.

6.5.1 Grid Connected Inverters

Figure 6.14 displays the closed-loop eigenvalues of nominal λ1( ), λ2( ), and λ3( ) together with their variations. The closed-loop inverters stability all running in grid-connected mode is suggested by the fact that all eigenvalues remain inside the unit circle.

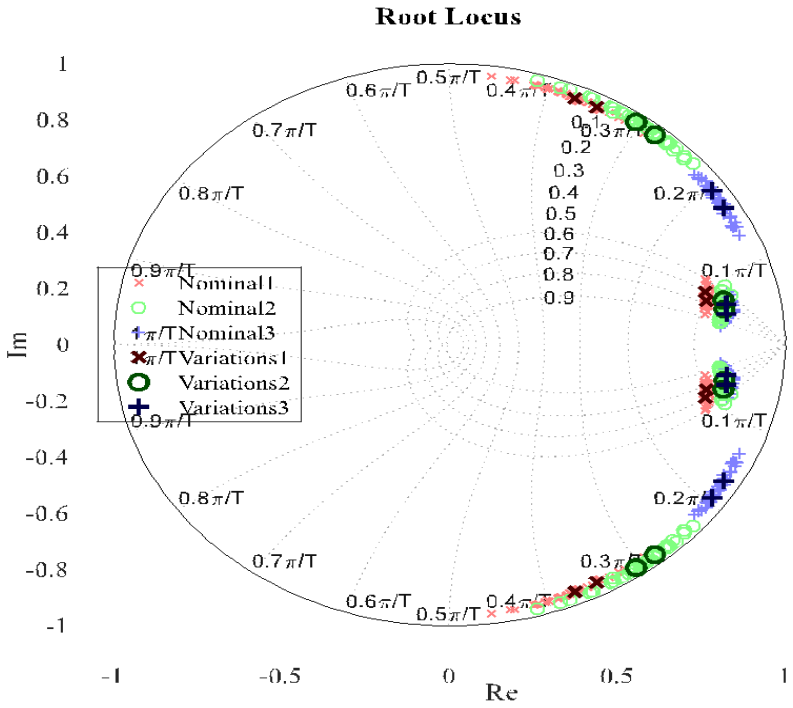

Fig. 6.14. Eigenvalues of nominal g1(s), g2(s), and g3(s)
And their variations

Table 5 displays the stability margins. These margins show that grid-connected closed-loop inverters in the nominal scenario are resilient up to disturbances of 12.21 db & 50.24°, and in the worst case, up to 10.63 db & 39.36°. As a result, the lqr-ort controller ensures that the closed loop inverters maintain stability even when the parameters are varied

stability margin	inv1	inv2	inv3
nominal gm	12.21db	14.40db	14.03db
nominal pm	52.43°	54.29°	50.24°
min uncertain gm	10.99db	12.17db	10.63 db
min uncertain pm	45.92°	46.29°	39.36°

Table 6.3. Stability margins of nominal state model and their variations

Fig. 6.15 shows the nominal λ1( ), λ2( ), and λ3( ) as well as their variations in singular value diagrams. The robust performance of the lqr-ort controller with established boundaries is confirmed through the results of singular value plots.

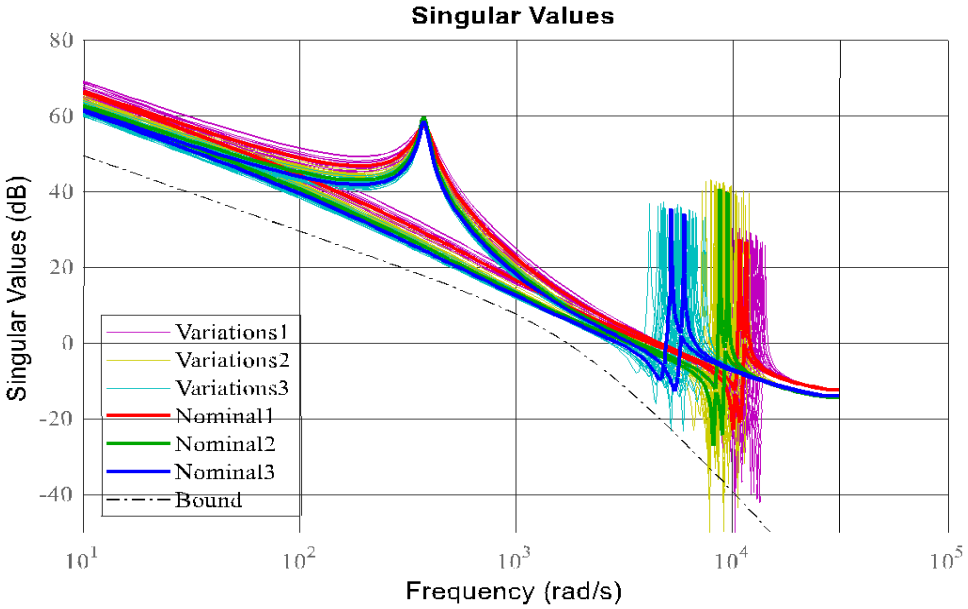

Fig. 6.15. Singular values diagram for λ1( ), λ2( ), **and** λ 3( ) **And their variations**

6.5.2 Islanded Microgrid

The eigenvalues and variations of the nominal function λ () are revealed in fig 6.16. The islanded microgrid is stable because every eigenvalue remains inside the unit circle. It utilises each inverter's lqr-ort controller. The gain margin along with the phase margin of the hypothetical islanded microgrid are 12.10 db and 42.68˚, respectively. Incorporating uncertainty regarding the load and components results in a minimum phase margin of 34.45^ and a min gain margin of 9.25 db for the microgrid. These findings show that the isolated microgrid is stable and resilient to variations in load and component composition. The eigenvalues and variations of the nominal function λ () are revealed in Fig. 56. The stable state of the islanded microgrid is achieved by all of the eigenvalues remaining within the unit circle. For every inverter, it utilises the lqr-ort controller. The phase margin along with the gain margin of the hypothetical islanded microgrid are 12.10 db and 42.68˚, respectively. Incorporating uncertainty regarding the load and components results in a min phase margin of 34.45^ and a minimum gain margin of 9.25 db for

the microgrid. These findings show that the isolated microgrid is stable and resilient to variations in load and component composition.

Lastly, fig. 6.17 displays the diagrams of singular value for the nominal λ ( ) and its modifications. The islanded microgrid's lqr-ort controller's performance robustness is confirmed by the results of the singular value plots.

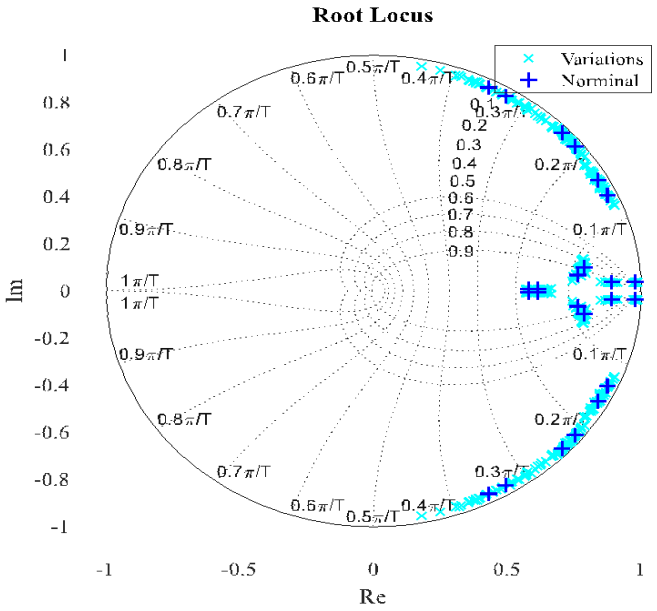

Fig. 6.16. Eigenvalues of nominal ( ) and its variations

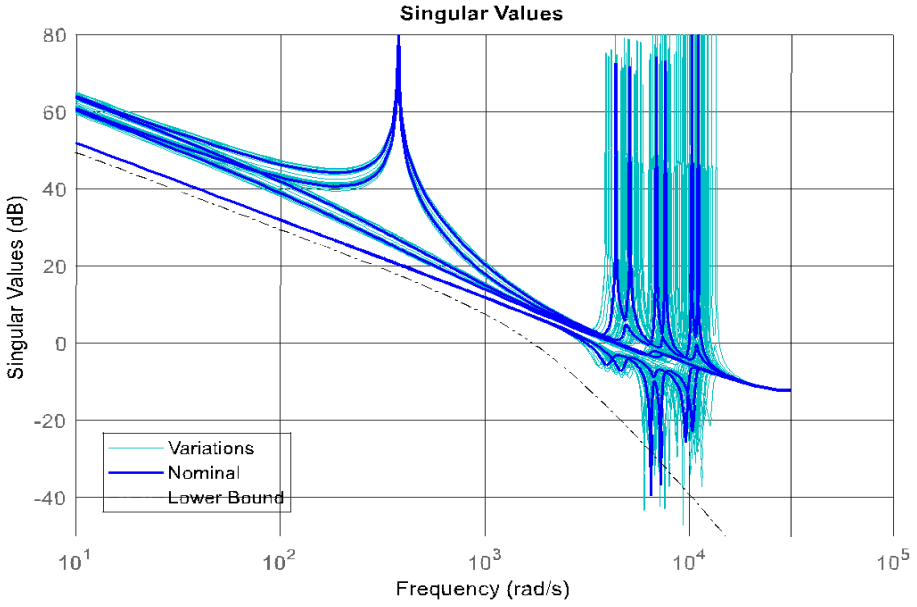

Fig. 6.17. Singular values diagram for ( ) and its variations with performance bound

6.6 Islanded Mode

The plan depicted in figure 38 served as the basis for both the physical and virtual experimentation for the islanded mode. The entire experiment was completed in 7 seconds. At first, the microgrid was linked to the main grid. The microgrid then began operating in islanded mode along with load 1 connected when the main grid switch was opened. Load 2 is linked at last.

6.6.1 Simulation Results

The circuit depicted in Fig. 6.18 was constructed in Matlab/Simulink by utilising the opal-rt Artemis libraries in order to acquire simulation results. Nominal values for the main grid amplitude and frequency were used. The microgrid frequency, the RMS voltage on ac bus, and the simulated output power of each inverter at various time intervals are displayed in Fig. 6.20.

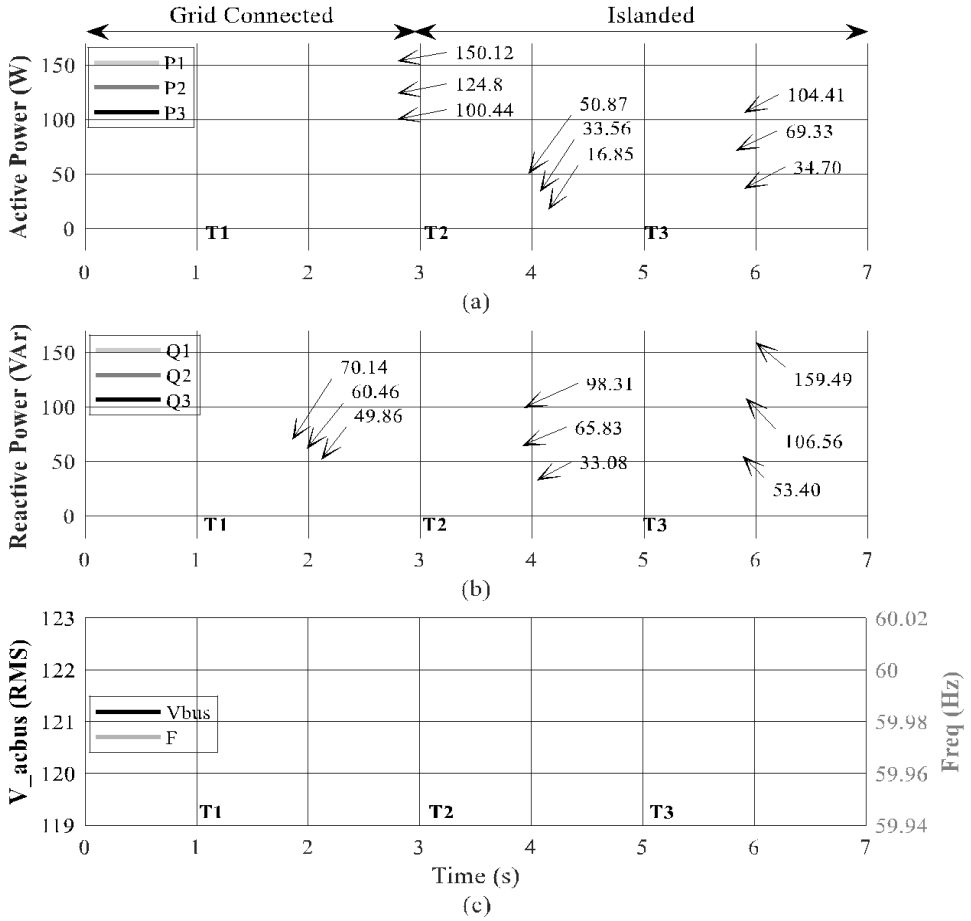

Fig. 6.18. Simulation results reactive power, active power, voltage in the AC bus and Frequency of the Microgrid

For inverters 1, 2, and 3, an active power reference of 100 watts, 125 watts, and 150 watts has been established at $_1$ = 1. It is evident that the 3 inverters exhibit a damped response, with a steady-state inaccuracy of less than 0.2 percent and a settling time of roughly 0.4 s.

The microgrid enters islanded mode with load 1 connected at $_2$ = 3 s, when the main grid is unplugged. At this point, the ac voltage of bus's and frequency recover in 0.05 and 0.1 seconds, respectively. The steady-state times for reactive and active powers are 0.5 and 0.3 seconds, respectively. Also, since load 2 is linked at 3 = 5, generated power is distributed proportionately among the 3 inverters based on their rated power capacities. There are disturbances of approximately 0.8 v and 0.01 hz in the microgrid frequency & 0.05 s in the ac bus voltage, respectively, followed by 0.1 s in the recovery time. Furthermore, there is an about 0.3 s settling period for both reactive and active power. Lastly, since simulation outcomes validate the performance of the suggested controller in a computational context, active and reactive power are still distributed proportionately across the three inverters.

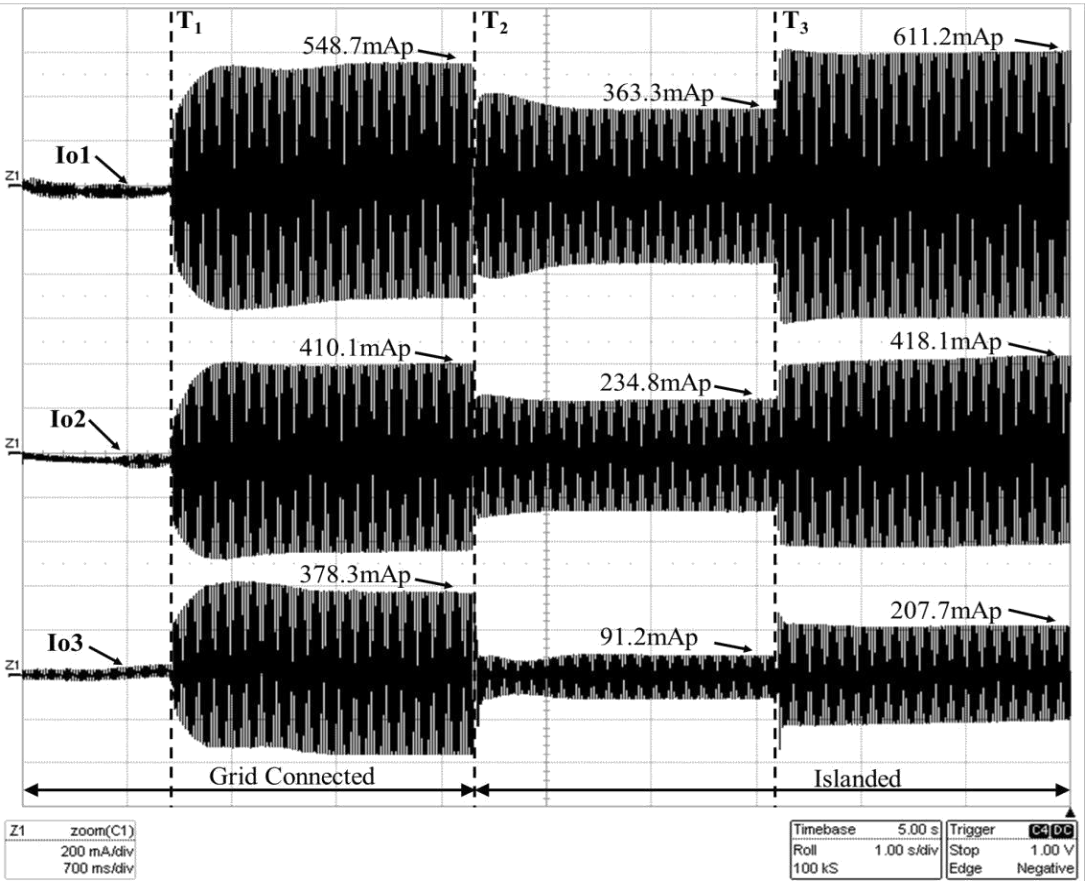

Fig. 6.19. output currents during experiment. = , = , = .
vgrid=200ma/div, hgrid=700ms/div

At 1 = 1, inverters 1, 2, and 3 were each assigned an active power reference of 100w, 125w, and 150w, respectively. Inverters 1, 2, and 3 each have their own reactive power reference, with values of 50var, 60var, and 70var, for example. Figure 63 shows the power and figure 64 depict the output currents of the 3 inverters; each exhibit a settling time of around 0.4 s, damped response, as well as steady-state error below 0.3%

The microgrid enters isolated mode with load 1 connected when the main grid is unplugged, which occurs at 2 = 3 s. In other words, the inverters recover voltage and frequency independently of one another and function as grid-forming generators to provide the electricity required by load 1. Here, 0.8s & 0.2 s, respectively, are required to restore the ac bus's frequency and voltage. After 0.8 s and half a second, respectively, the active and reactive powers have stabilized.

6.7 Controller Comparison

At 1 = 1, inverters 1, 2, and 3 were each assigned an active power reference of 100w, 125w, and 150w, respectively. Inverters 1, 2, and 3 each have their own reactive power reference, with values of 50var, 60var, and 70var, for example. Figure 63 shows the power and figure 64 shows the output currents of the 3 inverters; each exhibit a settling time of around 0.4 s, damped response, and a ‘steady-state error’ below 0.3%. The controller performance has been assessed in both the grid-connected and island mode. Taking into account transient responsiveness, quadratic cost values, and power coupling, the lqr-ort controller was compared in grid-connected mode. Islanded mode was used to investigate the lqr-ort as well as the voltage and frequency restoration loops. This investigation took into account the transient response, proportional power output, and voltage along with the frequency restoration.

Mode 6.7.1: Grid-Connected

1. Section 4.6.1's findings indicate that, while operating in grid-connected mode, the lqr-ort controller outperforms the traditional droop controller from [36] in terms of enhancing power coupling and transient responsiveness. There are number of benefits to this method that set it apart from a others in the literature, including: improved transient response, less tracking error,

as well as fewer power losses during transient responses are all benefits of this method over the standard droop controller, which results in a lower cost function.

2. As shown in [15], the utilization of a lqr controller has appropriate robustness characteristics with respect to phase margins & gain. Reduced active-reactive power coupling is a third benefit of the controller. Reason being, unlike traditional droop control, which relies on amplitude and frequency modifications, LQR-ORT power sharing control does not.to better estimate the closed loop inverter stability in grid-connected mode under component uncertainties, the suggested model for calculating the lqr-ort controller permits the use of robustness analysis methodologies.
3 unlike the standard droop control; this method does not include resonant filters, which might impact sensitivity and robustness when dealing with fluctuations in parameters.

6.7.2 Self-Contained Mode

Power sharing accuracy, settling time, voltage and frequency restoration, and other metrics were used to compare the findings for the islanded mode (section 4.6.2) to literature.

The precision of power sharing (4.7.2.1) in isolated mode, the lqr-ort controller restores the ac bus voltage amplitude utilizing a voltage restoration loop that includes an integrator. Distributing power production across inverters based on their rated power capabilities is another possible usage of this restoration loop. To contrast the lqr-ort controller's power sharing accuracy with the data presented in [51]. A droop controller having an additional control loop to improve the accuracy of power sharing was compared to a standard droop controller in this study. According to the findings, the control loop that was recommended by the authors was able to reach a sharing ratio of 1:2.02, whereas the traditional droop obtained a ratio of 1:1.867 for power sharing among 2 inverters that had a rated power capacity ratio of 1:2 [51]. The lqr-ort controller, when paired by utilizing the recommended voltage restoration loop, is able to reach a power sharing ratio of around 1:2.006. This is demonstrated in section 3.4.2. When contrasted with the findings presented in [51], this one is more outstanding.

Restoring Voltage and Frequency (4.7.2.2)

Methods from references [7], [36], [66], [91], and [94] were contrasted with islanded mode's voltage and frequency restoration. When operating in either grid-connected or island mode, the lqr-ort controller synchronizes each inverter with the ac bus by implementing a sogi-pll gaving a new frequency restoration loop. According to (70), this synchronization enhances power sharing decoupling and enables the elimination of the q component of ac bus voltage.

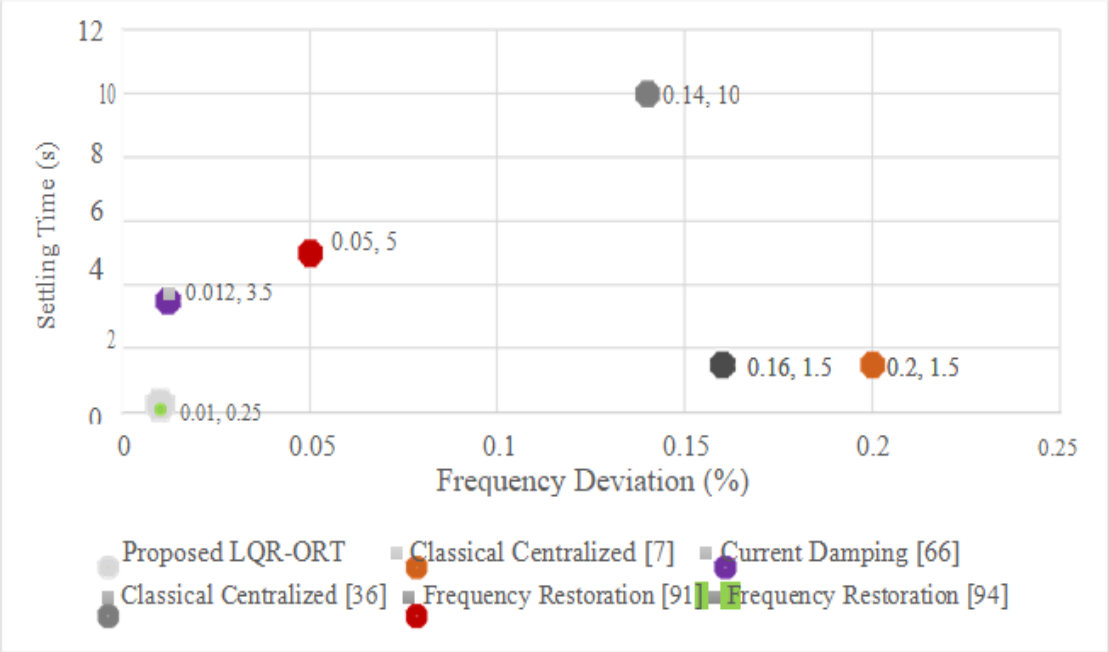

Fig. 6.20. Comparison between Frequency Restoration Approaches

Chapter 7

Concluding Remarks & Future Work

In this study, we provide a new model and controller that combine the dynamics of v-i and power sharing into one state-space model. The model may be adjusted to work in either grid-connected or island-mode implementations. Islanded mode is a mathematical approach that might be applied for current stability and robustness analysis; it can combine any number of loads and generators into a single open-loop model. An open-loop state-space model is necessary for the implementation of numerical optimization techniques in modern control methods like lqr, ∐, or -syn-thesis. These approaches seek for an appropriate controller based on a specified control target. Utilizing the superposition principle and the suggested integrated model in dq frame (66), state-of-the-art control techniques may be applied to inverter-based generators, enhancing their transient responsiveness and resilience while also including v-i and power sharing dynamics. The suggested model and controller also make use of inverter-based generators' low-inertia properties. Optimal methods for converting dc to ac have not been identified in the literature; ap-proaches instead mimic the operation of a mechanical synchronous machine.

The suggested lqr-ort controller enhances transient responsiveness, power sharing accuracy, voltage as well as frequency restoration, and grid-connected and island microgrids. It will be reported that communication-free voltage and frequency restores provide microgrid resilience against abnormal situations. The lqr-ort controller demonstrates stable performance and resilience in the face of component and multiplicative uncertainty, according to stability and robustness study. In heavy-duty applications, where component specifications might be affected over time by external factors, resilience against component variations is crucial. The provided method has been validated by experimental findings, which show that it is superior to previous literature work. Other kinds of contemporary control systems described in the literature may be implemented using the same methodology as the pqvi controller given in this study.

The following list of future projects could significantly enhance the quality of the work that has already been presented: to investigate whether this control mechanism may be used to create a dc Microgrid

Appendix A: numerical values for the suggested simulation

We provide state-space models of the whole microgrid in island mode as well as each inverter that is linked to the main grid. Models in the discrete state space have been shown in the dq frame. The shannon sampling theory [90] established a sample frequency of 10 khz. The 17-th order, or $h17$ = 1,020hz, harmonics may be controlled using this controller. Only discrete-time is used to display computed controllers

1. Grid-Connected Inverters

Assuming a main grid voltage= $[120\sqrt{2} - 0]$ the following output matrix is de-fined for all the inverters

$$C = \begin{bmatrix} 0 & 0 & 0 & 0 & 254.5584 & 0 & 0 & 0 \\ 0 & 0 & 0 & 0 & 0 & -254.5584 & 0 & 0 \end{bmatrix} \quad (107)$$

Inverter 1

1.1.1 State-Space Model

$\bar{A}_{dq1=}$

$$\begin{bmatrix} 0.4321 & 0.0163 & 9.1123 & 0.3437 & -9.1123 & -0.3437 & 0.2837 & 0.0070 \\ -0.0163 & 0.4321 & -0.3437 & 9.1123 & 0.3437 & -9.1123 & -0.0070 & 0.2837 \\ -0.0445 & -0.0017 & 0.7157 & 0.0270 & 0.2836 & 0.0107 & 0.0501 & 0.0009 \\ 0.0017 & -0.0445 & -0.0270 & 0.7157 & -0.0107 & 0.2836 & -0.0009 & 0.0501 \\ 0.0445 & 0.0017 & 0.2836 & 0.0107 & 0.7157 & 0.0270 & 0.0055 & 0.0002 \\ -0.0017 & 0.0445 & -0.0107 & 0.2836 & -0.0270 & 0.7157 & -0.00002 & 0.0055 \\ 0 & 0 & 0 & 0 & 0 & 0 & 1 & 0 \\ 0 & 0 & 0 & 0 & 0 & 0 & 0 & 1 \end{bmatrix}$$

$\bar{B}_{1dq1=}$

$$\begin{bmatrix} 0 & 0 \\ 0 & 0 \\ 0 & 0 \\ 0 & 0 \\ 0 & 0 \\ 0 & 0 \\ 0.0001 & 0 \\ 0 & 0.0001 \end{bmatrix}$$

1.1.2 Controller

$\bar{K}_{d1=}$

$$\begin{matrix} -1218.41 & -62.37 & 6383.08 & 1232.97 & 23441.32 & 2106.23 & 5236.10 & 73.16 \\ 62.37 & -1218.41 & -1232.97 & 6383.08 & -2106.23 & 23441.32 & -73.16 & 5236.10 \end{matrix}$$

$[P_{v1}\ Q_{v1}]^T =$ $\begin{bmatrix} 117.3282 & 11.5299 \\ 11.5299 & -117.3282 \end{bmatrix}$

$\begin{bmatrix} -5746.130 \\ -549.409 \end{bmatrix}$

Inverter 2

1.2.1 state-space model

$\bar{A}_{dq2=}$

$$\begin{bmatrix} 0.6074 & 0.0229 & 9.8282 & 0.3707 & -9.8282 & -0.3707 & 0.0980 & 0.0024 \\ -0.0229 & 0.6074 & -0.3707 & 9.8282 & 0.3707 & -9.8282 & -0.0024 & 0.0980 \\ -0.0160 & -0.0006 & 0.9013 & 0.0340 & 0.0980 & 0.0037 & 0.0179 & 0.0003 \\ 0.0006 & -0.0160 & -0.0340 & 0.9013 & -0.0037 & 0.0980 & -0.0003 & 0.0179 \\ 0.0480 & 0.0018 & 0.2939 & 0.111 & 0.7054 & 0.0266 & 0.0019 & 0.0001 \\ -0.0018 & 0.0480 & -0.0111 & 0.2939 & -0.0266 & 0.7054 & -0.0001 & 0.0019 \\ 0 & 0 & 0 & 0 & 0 & 0 & 1 & 0 \\ 0 & 0 & 0 & 0 & 0 & 0 & 0 & 1 \end{bmatrix}$$

$\bar{B}_{1dq2=}$

$$\begin{bmatrix} 0 & 0 \\ 0 & 0 \\ 0 & 0 \\ 0 & 0 \\ 0 & 0 \\ 0 & 0 \\ 0.0001 & 0 \\ 0 & 0.0001 \end{bmatrix}$$

1.2.2 Controller

$\bar{K}_{d2=}$

$$\begin{matrix} -1730.34 & -87.67 & 12833.16 & 2941.53 & 19023.82 & 1727.68 & 3716.85 & 54.99 \\ 87.67 & -1730.34 & -2941.53 & 12833.16 & -1727.68 & 19023.82 & -54.99 & 3716.85 \end{matrix}$$

$[P_{v2}\ Q_{v2}]^T =$ $\begin{bmatrix} 125.3842 & 16.6365 \\ 16.6365 & -125.3842 \end{bmatrix}$

$\begin{bmatrix} -2635.126 \\ -247.277 \end{bmatrix}$

Inverter 3

1.3.1 state-space model

$\bar{A}_{dq2=}$

$$\begin{matrix} 0.7001 & 0.0264 & 10.1979 & 0.3846 & -10.1979 & -0.3846 & 0.1496 & 0.0037 \\ -0.0264 & 0.7001 & -0.3846 & 10.1979 & 0.3846 & -10.1979 & -0.0037 & 0.1496 \\ -0.0249 & -0.0009 & 0.8497 & 0.0320 & 0.1496 & 0.0056 & 0.0264 & 0.0005 \\ 0.0009 & -0.0249 & -0.0320 & 0.8497 & -0.0056 & 0.1496 & -0.0005 & 0.0264 \\ 0.0249 & 0.0009 & 0.1496 & 0.0056 & 0.8497 & 0.0320 & 0.0014 & 0.0000 \\ -0.0009 & 0.0249 & -0.0056 & 0.149 & -0.0320 & 0.8497 & 0.0000 & 0.0014 \\ 0 & 0 & 0 & 0 & 0 & 0 & 1 & 0 \\ 0 & 0 & 0 & 0 & 0 & 0 & 0 & 1 \end{matrix}$$

$\bar{B}_{1dq3=}$

$$\begin{bmatrix} 0 & 0 \\ 0 & 0 \\ 0 & 0 \\ 0 & 0 \\ 0 & 0 \\ 0 & 0 \\ 0.0001 & 0 \\ 0 & 0.0001 \end{bmatrix}$$

1.3.2 Controller

$\bar{K}_{d3=}$

$$\begin{matrix} -1057.25 & -58.51 & 11441.44 & 2028.32 & 19604.84 & 2480.08 & 3805.98 & 55.47 \\ 58.51 & -1057.25 & -2028.32 & 11441.44 & -2480.08 & 19604.84 & -55.47 & 3805.98 \end{matrix}$$

$[P_{v3}\ Q_{v3}]^T =$ $\begin{bmatrix} 125.3842 & 16.6365 \\ 16.6365 & -125.3842 \end{bmatrix}$

$$\begin{bmatrix} -2635.126 \\ -247.277 \end{bmatrix}$$

Appendix B: Simulink Block Diagrams

1. Microgrid model for simulation

Figure D.1displays the block diagram for the microgrid simulation. This block diagram has been utilised for grid-connected mode simulations as well as islanded mode simulations. Figure 45 depicts the block diagram for every inverter that is equipped with the LCL filter. This primary grid block has been comprised of a continuous 3-phase generator that is fitted by utilizing the voltage along with the current measuring equipment.

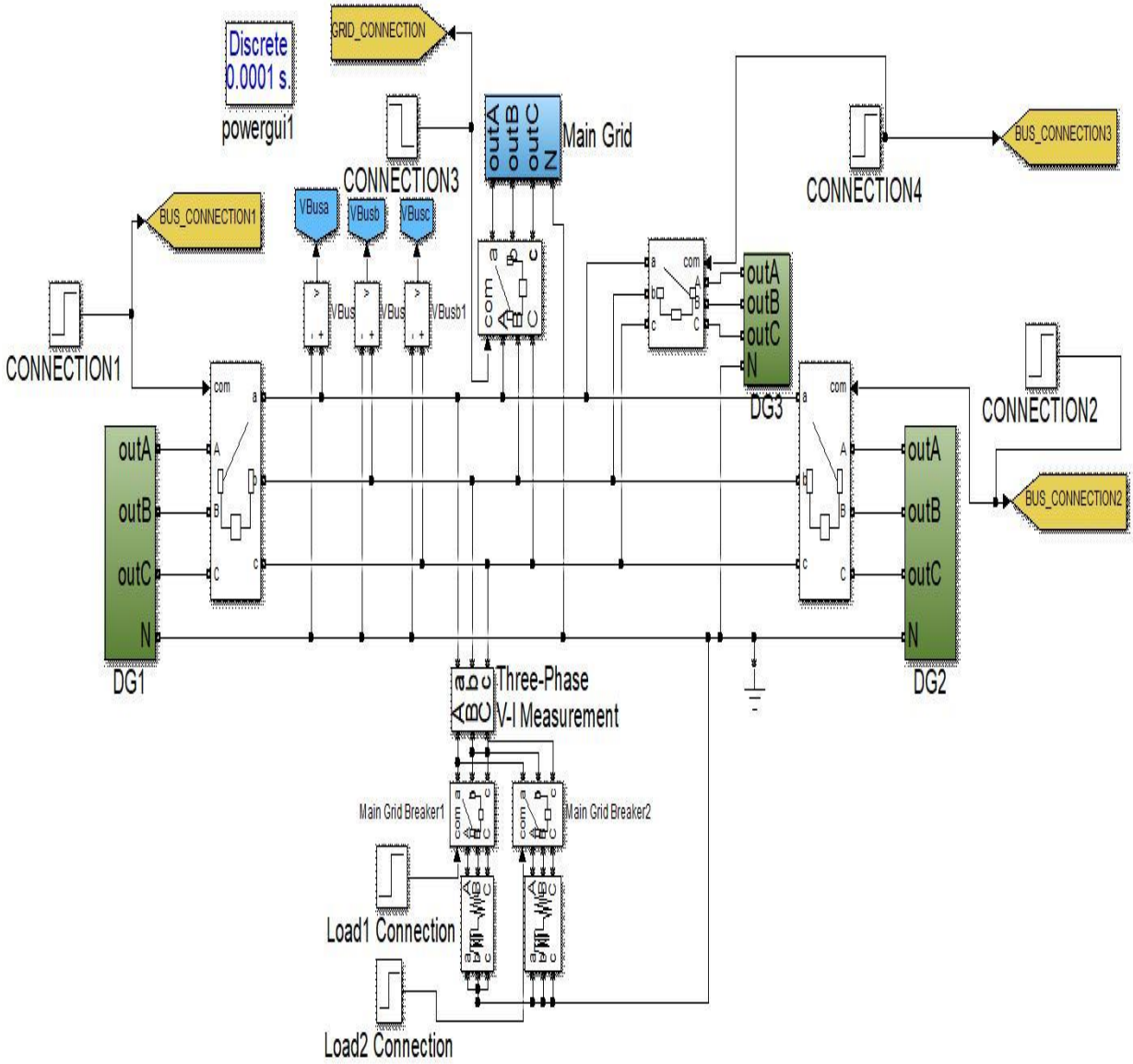

Fig. B.1. Block in Simulink for the modeling of microgrids and the validation of controllers

2. Circuit measurement and *dq* transformation

The *dq* transformation utilized in the experimental and simulation findings reported in section 4.6 was carried out using the block diagram displayed in fig. D.2.

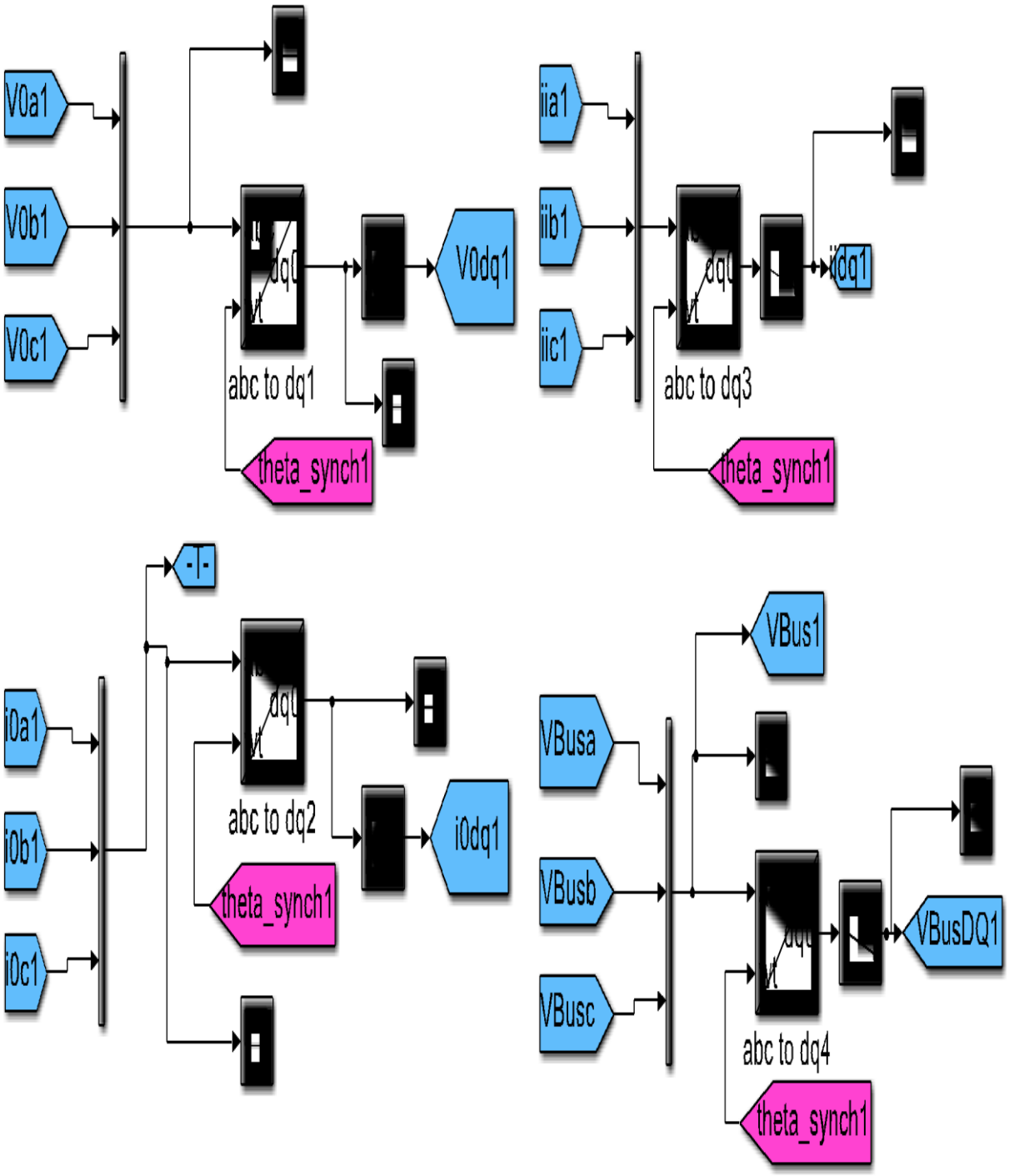

Fig. B.2. Measurement and dq transformation performed on A circuit using a block diagram with Simulink

3. Controller Model Implemented In the Dspace 1006

Using the dspace 1006, the block diagram depicted in figure D.3 has been programmed to produce the experimental and simulation findings reported in section 4.6. Both grid-connected as well as islanded modes were implemented using the block diagram.

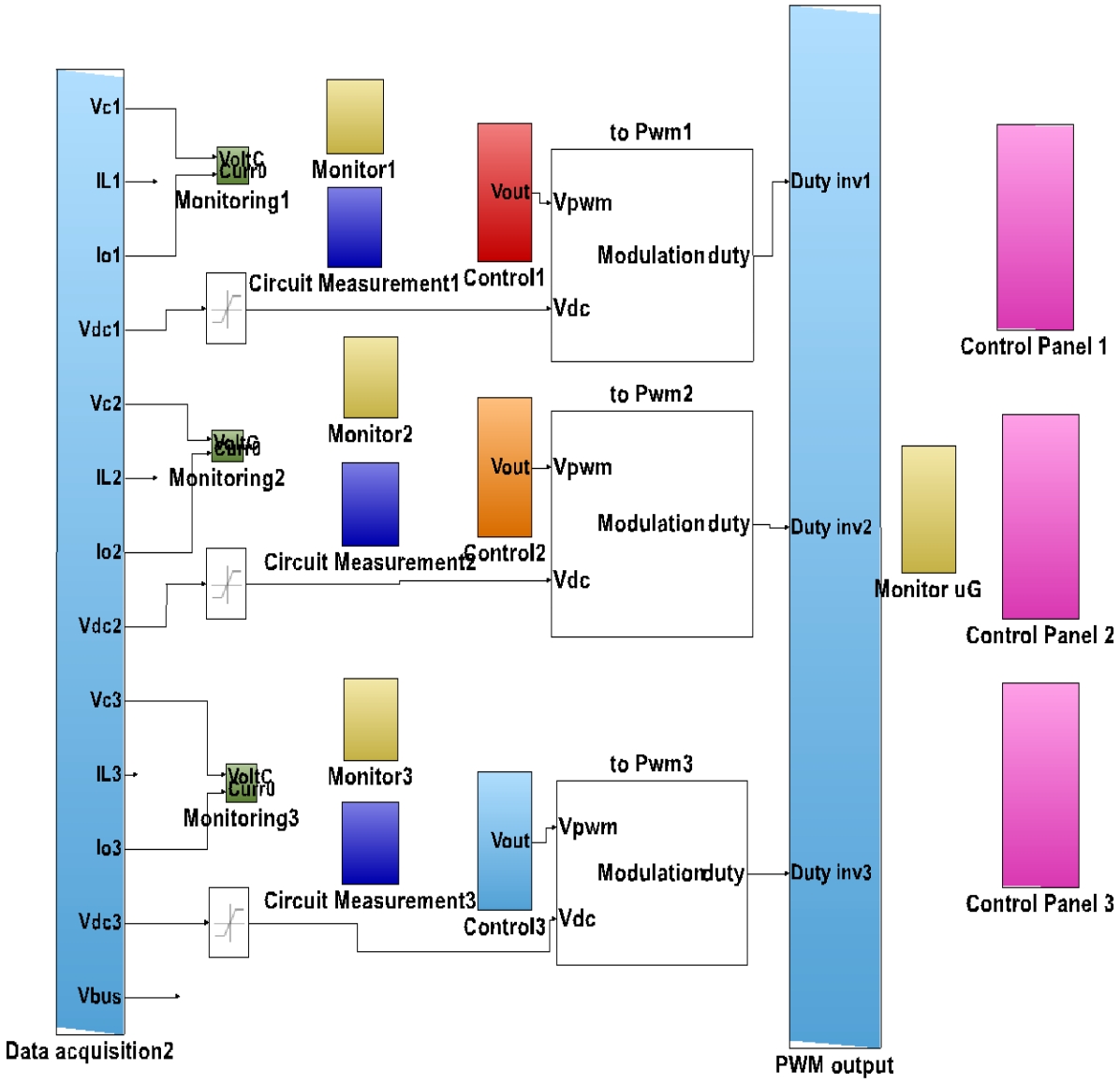

Fig. B.3.Diagram of the Controller's Implementation Using the Simulink Block Diagram on the dSPACE 1006

3.1 Integrated P_{qvi} Controller Block Diagram Created Using Simulink

The integrated p_{qvi} controller utilised for the grid-connected & islanded mode is depicted in the block diagram in Figure D.4. Blocks "control 1," "control 2," and "control 3" from Figure D.1 contain this block diagram. The integrated PQVI controller's simulink block diagram is seen in Figure D.1.The reference for reactive and active power is signals. The grid connection flag, or signal, is what activates frequency and voltage restoration loops. The error in the nominal value of ac bus voltage has been integrated by the voltage restoration loop. The block $\hbar$ 1 contains the implementation of the frequency restoration loop. The block contains the implementation of the lqr-ort controller.

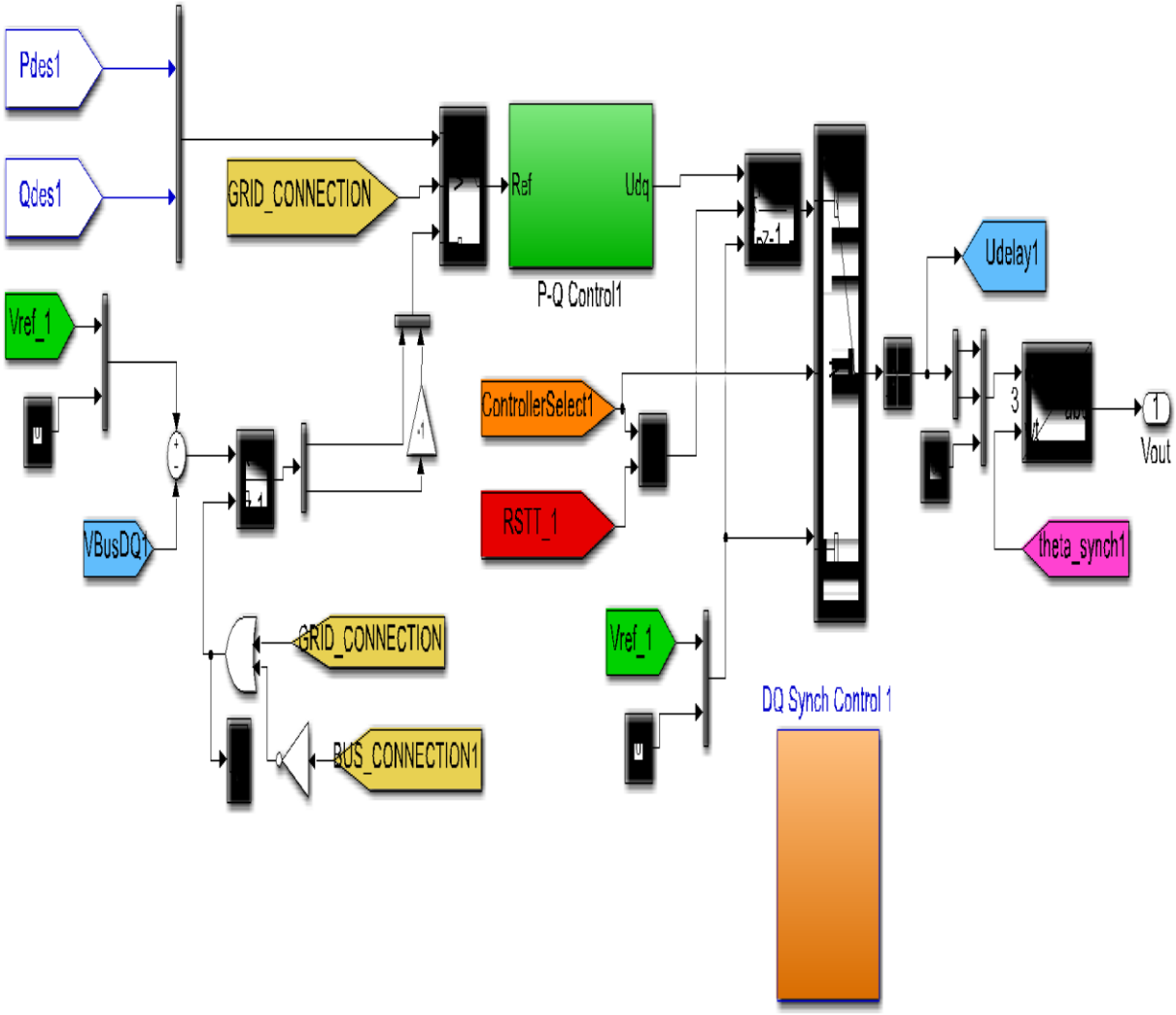

Fig. B.4. Block diagram of the integrated Pqvi controller in Simulink

3.2 Simulink Block Diagram for the Lqr-Ort Controller

Figure D.5 displays the block diagram of the lqr-ort controller, which is utilized in islanded as well as grid-connected modes. For steady-state error control, this block includes the best tracking and feedback matrices along with a low-gain integrator.

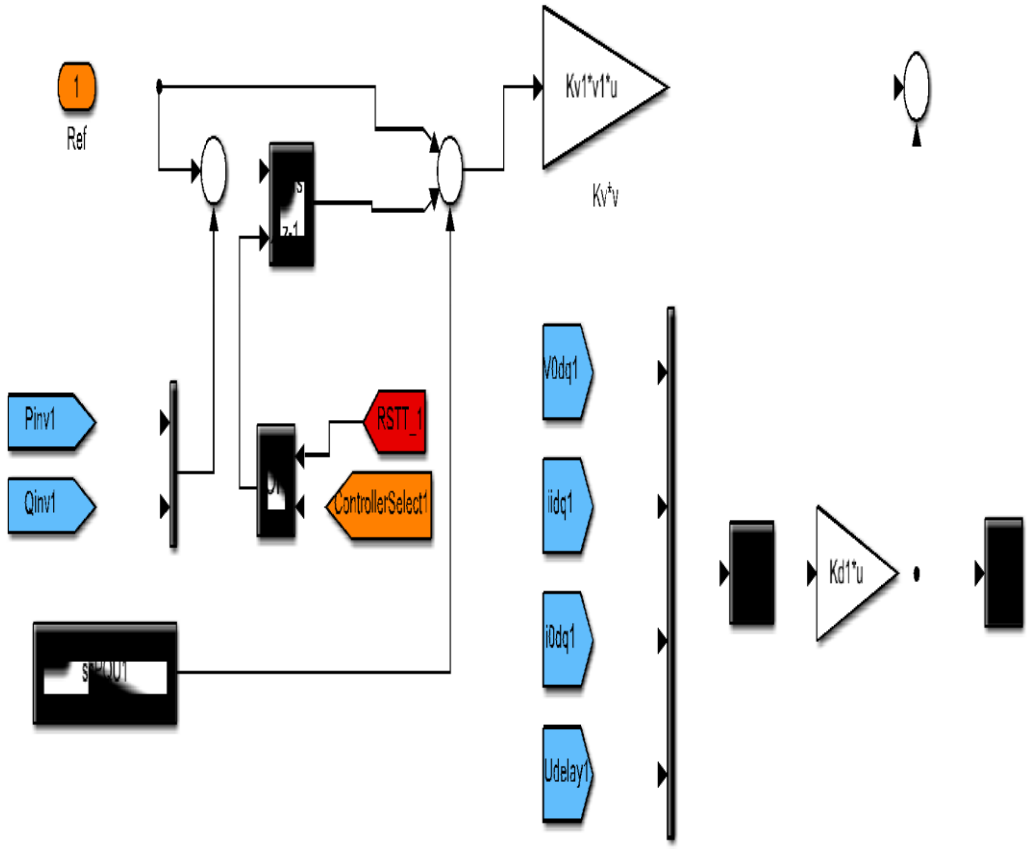

Fig. B.5. Simulink block diagram for the lqr-ort controller

3.3 Simulink Block Diagram for the PLL-SOGI with the Frequency Restoration Loops

The sogi-pll with the frequency restoration loop utilised for grid-connected along with the islanded mode is depicted in block diagram in Figure D.6. The park transformation specified in must be used to receive the sogi-pll input in the frame (3).

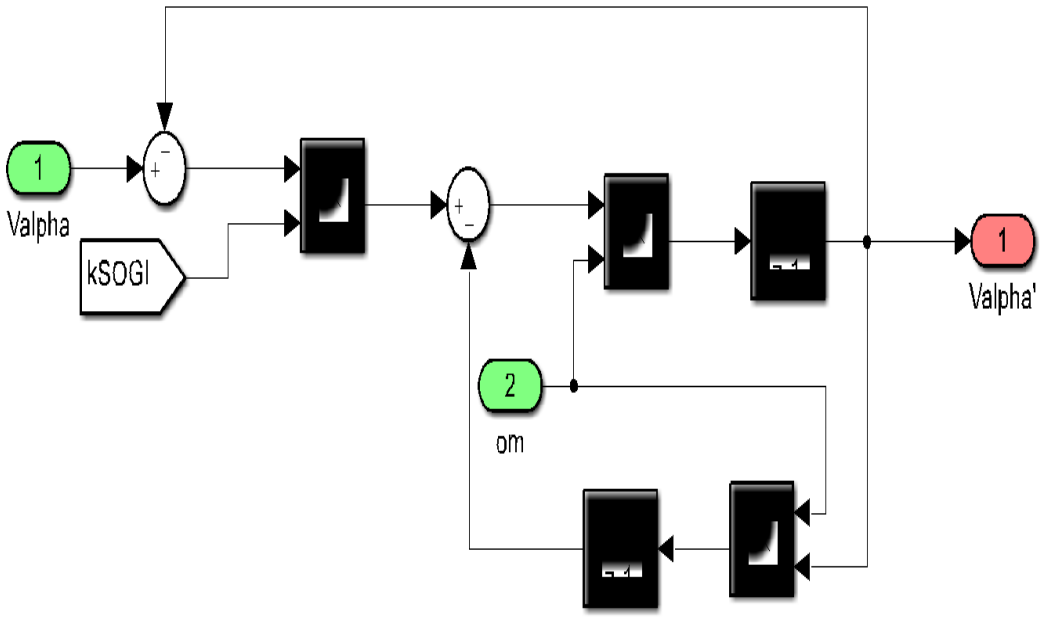

Fig. B.6. Block schematic in Simulink "for the Sogi-Pll including the Frequency Restoration loop. Top: pll synchronizer with frequency
Restoration loop. Bottom: sogi component for" component.

Bibliography

[1] Research navigant, “microgrid deployment tracker 2q18.” [online]. Available: https://www.navigantresearch.com/reports/microgrid-deployment-tracker-2q18. [accessed: 18-oct-2018].

[2] Opal-rt technologies, “opal-rt solution for micro-grid applications real time simulation opal-rt technologies,” 2018.

[3] National instruments, “control and monitor microgrids an ni industrial iot lab Demonstration.” [online]. Available: http://download.ni.com/pub/iot/iiot_lab_control_and_monitor_microgrids.pdf. [accessed: 18-oct-2018].

[4] Dspace systems, “online catalog,” 2018. [online]. Available: https://www.dspace.com/en/pub/home/medien/product_info/catalog_contents.cfm.

[5] D. T. Ton and m. A. Smith, “the u.s. Department of energy’s microgrid initiative,” *Electr. J.*, vol. 25, no. 8, pp. 84–94, 2012.

[6] R. H. Lasseter, “microgrids,” *2002 ieee power eng. Soc. Winter meet. Conf. Proc. (cat. No.02ch37309)*, vol. 1, pp. 305–308, 2002.

[7] J. M. Guerrero, j. C. Vasquez, j. Matas, l. G. De vicuña, and m. Castilla, “hierarchical control of droop-controlled ac and dc microgrids - a general approach toward standardization,” *ieee trans. Ind. Electron.*, vol. 58, no. 1, pp. 158–172, 2011.

[8] S. Bernet, “recent developments of high power converters for industry and traction applications,” *ieee trans. Power electron.*, vol. 15, no. 6, pp. 1102–1117, 2000.

[9] H. Athari, m. Niroomand, and m. Ataei, “review and classification of control systems in grid-tied inverters,” *renew. Sustain. Energy rev.*, vol. 72, no. February, pp. 1167–1176, 2017.

[10] R. Teodorescu, m. Liserre, and p. Rodríguez, *grid converters for photovoltaic and wind power systems*. Chichester, uk: john wiley & sons, ltd, 2011.

[11] F. Blaabjerg, r. Teodorescu, m. Liserre, and a. V. Timbus, “overview of control and grid synchronization for distributed power generation systems,” *ieee trans. Ind. Electron.*, vol. 53, no. 5, pp. 1398–1409, 2006.

[12] W. Group, *ieee application guide for ieee std 1547, ieee standard for interconnecting distributed resources with electric power systems*, no. April. 2008.

[13] Kiam heong ang, g. Chong, and yun li, “pid control system analysis, design, and technology,” *ieee trans. Control syst. Technol.*, vol. 13, no. 4, pp. 559–576, jul. 2005.

[14] F. B. Blaabjerg, k. Z. Zhou, d. W. Wang, and y. Y. Yang, *periodic control of power electronic converters*. Institution of engineering and technology, 2016.

[15] F. L. Lewis, d. L. Vrabie, and v. L. Syrmos, *optimal control*. Hoboken, nj, usa: john wiley & sons, inc., 2012.

[16] J. Kennedy and r. Eberhart, "particle swarm optimization," in *proceedings of icnn'95 - international conference on neural networks*, 1994, vol. 4, no. 10, pp. 1942–1948.

[17] R. L. Williams and d. A. Lawrence, *linear state-space control systems*. Hoboken, nj, usa: john wiley & sons, inc., 2007.

[18] J. . Maciejowski, *multivariable feedback design*, vol. 1, no. 1. Addison wesley, 1989.

[19] L. Qiu, "essentials of robust control," *automatica*, vol. 38, no. 5, pp. 910–912, 2002.

[20] Fang zheng peng and jih-sheng lai, "generalized instantaneous reactive power theory for three-phase power systems," *ieee trans. Instrum. Meas.*, vol. 45, no. 1, pp. 293–297, 1996.

[21] J. L. Afonso, m. J. S. Freitas, and j. S. Martins, "p-q theory power components calculations," in *2003 ieee international symposium on industrial electronics (cat. No.03th8692)*, 2003, vol. 1, pp. 385–390.

[22] A. Bidram and a. Davoudi, "hierarchical structure of microgrids control system," *ieee trans. Smart grid*, vol. 3, no. 4, pp. 1963–1976, 2012.

[23] T. Iwade, s. Komiyama, y. Tanimura, m. Yamanaka, m. Sakane, and k. Hirachi, "a novel small-scale ups using a parallel redundant operation system," *25th int. Telecommun. Energy*
Conf. 2003. Intelec '03., pp. 480–484, 2003.

[24] J. C. Yeong and k. K. S. Eng, "a novel communication strategy for decentralized control of paralleled multi-inverter systems," *ieee trans. Power electron.*, vol. 21, no. 1, pp. 148– 156, 2006.

[25] X. Sun, y. S. Lee, and d. Xu, "modeling, analysis, and implementation of parallel multi-inverter systems with instantaneous average-current-sharing scheme," *ieee trans. Power electron.*, vol. 18, no. 3, pp. 844–856, 2003.

[26] X. Sun, l. K. Wong, y. S. Lee, and d. Xu, "design and analysis of an optimal controller for parallel multi-inverter systems," *ieee trans. Circuits syst. Ii express briefs*, vol. 53, no. 1, pp. 56–61, 2006.

[27] Wu tsai-fu and y. K. Chen, "3c strategy for inverters in parallel operation achieving an equal current distribution," *ieee trans. Ind. Electron.*, vol. 47, no. 2, pp. 273–281, 2000.

[28] H. Han, x. Hou, j. Yang, j. Wu, m. Su, and j. M. Guerrero, "review of power sharing control strategies for islanding operation of ac microgrids," *ieee trans. Smart grid*, vol. 7, no. 1, pp. 200–215, jan. 2016.

[29] J. Uudrill, “dynamic stability calculations for an arbitrary number of interconnected synchronous machines,” *ieee trans. Power appar. Syst.*, vol. Pas-87, no. 3, pp. 835–844, mar. 1968.

[30] A. R. Bergen and v. Vittal, “power systems analaysis,” *department of electrical engineering*.
pp. 103–127, 2007.

[31] E. A. A. Coelho, p. C. Cortizo, and p. F. D. Garcia, “small-signal stability for parallel-connected inverters in stand-alone ac supply systems,” *ieee trans. Ind. Appl.*, vol. 38, no. 2, pp. 533–542, 2002.

[32] C. K. Sao and p. W. Lehn, “autonomous load sharing of voltage source converters,” *Ieee trans. Power deliv.*, vol. 20, no. 2, pp. 1009–1016, 2005.

[33] C. K. Sao and p. W. Lehn, “control and power management of converter fed microgrids,” *ieee trans. Power syst.*, vol. 23, no. 3, pp. 1088–1098, 2008.

[34] E. Rokrok and m. E. H. Golshan, “adaptive voltage droop scheme for voltage source converters in an islanded multibus microgrid,” *iet gener. Transm. Distrib.*, vol. 4, no. 5, p. 562, 2010.

[35] U. Borup, f. Blaabjerg, and p. N. Enjeti, “sharing of nonlinear load in parallel-connected three-phase converters,” *ieee trans. Ind. Appl.*, vol. 37, no. 6, pp. 1817–1823, 2001.

[36] J. C. Vasquez, j. M. Guerrero, m. Savaghebi, j. Eloy-garcia, and r. Teodorescu, “modeling, analysis, and design of stationary-reference-frame droop-controlled parallel three-phase voltage source inverters,” *ieee trans. Ind. Electron.*, vol. 60, no. 4, pp. 1271– 1280, 2013.

[37] Q. Shafiee, j. M. Guerrero, and j. C. Vasquez, “distributed secondary control for Islanded microgrids - a novel approach,” *ieee trans. Power electr.*, vol. 29, no. 2, pp. 1018–1031, 2014.

[38] M. Hao and x. Zhen, “a control strategy for voltage source inverter adapted to multi - mode operation in microgrid,” *chinese control conf. Ccc*, pp. 9163–9168, 2017.

[39] A. Tuladhar, h. Jin, t. Unger, and k. Mauch, “parallel operation of single phase inverter modules with no control interconnections,” in *proceedings of apec 97 - applied power electronics conference*, 1997, vol. 1, pp. 94–100.

[40] E. A. A. Coelho, p. C. Cortizo, and p. F. D. Garcia, “small signal stability for single phase inverter connected to stiff ac system,” *conf. Rec. 1999 ieee ind. Appl. Conf. Thirty-forth ias annu. Meet. (cat. No.99ch36370)*, vol. 4, pp. 2180–2187, 1999.

[41] N. Pogaku, m. Prodanović, and t. C. Green, “modeling, analysis and testing of autonomous operation of an inverter-based microgrid,” *ieee trans. Power electron.*, vol. 22, no. 2, pp. 613–625, 2007.

[42] W. Xiao, p. Kanjiya, j. L. Kirtley, n. H. Kan'an, h. H. Zeineldin, and v. Khadkikar, "a modified control topology to improve stability margins in micro-grids with droop controlled ibdg," in *3rd renewable power generation conference (rpg 2014)*, 2014, pp. 5.2.2-5.2.2.

[43] J. Dannehl, f. W. Fuchs, and p. B. Thøgersen, "pi state space current control of grid-connected pwm converters with LCL filters," *ieee trans. Power electron.*, vol. 25, no. 9, pp. 2320–2330, 2010.

[44] C. A. Busada, s. Gomez jorge, a. E. Leon, and j. A. Solsona, "current controller based on reduced order generalized integrators for distributed generation systems," *ieee trans. Ind. Electron.*, vol. 59, no. 7, pp. 2898–2909, 2012.

[45] S. K. Singh and s. Ghatak choudhuri, "a conflict in control strategy of voltage and current controllers in multi-modular single-phase ups inverters system," *2017 10th int. Symp. Adv. Top. Electr. Eng. Atee 2017*, pp. 631–636, 2017.

[46] M. N. Marwali and a. Keyhani, "control of distributed generation systems - part i: voltages and currents control," *ieee trans. Power electron.*, vol. 19, no. 6, pp. 1541–1550, 2004.

[47] S. Eren, a. Bakhshai, and p. Jain, "control of three-phase voltage source inverter for renewable energy applications," *2011 ieee 33rd int. Telecommun. Energy conf.*, pp. 1–4, 2011.

[48] S. Eren, a. Bakhshai, and p. Jain, "control of grid-connected voltage source inverter with
LCL filter," *2012 twenty-seventh annu. Ieee appl. Power electron. Conf. Expo.*, pp. 1516– 1520, 2012.

[49] C. Dirscherl, j. Fessler, c. M. Hackl, and h. Ipach, "state-feedback controller and observer design for grid-connected voltage source power converters with LCL-filter," *2015 ieee conf. Control appl. Cca 2015 - proc.*, pp. 215–222, 2015.

[50] F. Huerta, d. Pizarro, s. Cóbreces, f. J. Rodríguez, c. Girón, and a. Rodríguez, "lqg servo controller for the current control of LCL grid-connected voltage-source converters," *ieee trans. Ind. Electron.*, vol. 59, no. 11, pp. 4272–4284, 2012.

[51] R. Majumder, b. Chaudhuri, a. Ghosh, r. Majumder, g. Ledwich, and f. Zare, "improvement of stability and load sharing in an autonomous microgrid using supplementary droop control loop," *ieee trans. Power syst.*, vol. 25, no. 2, pp. 796–808, 2010.

[52] S. A. Khajehoddin, m. Karimi-ghartemani, and m. Ebrahimi, "optimal and systematic Design of current controller for grid-connected inverters," *ieee j. Emerg. Sel. Top. Power electron.*, vol. 6, no. 2, pp. 1–1, 2018.

[53] A. Hasanzadeh, c. S. Edrington, b. Maghsoudlou, and h. Mokhtari, "optimal lqr-based multi-loop linear control strategy for ups inverter applications using resonant controller," *proc. Ieee conf. Decis. Control*, pp. 3080–3085, 2011.

[54] M. Babaei, t. Qunais, and s. Abdelwahed, “a linear quadratic tracking based voltage Controller for vsi; mvdc shipboard power system application,” *ieee power energy soc. Gen. Meet.*, vol. 2018-janua, pp. 1–5, 2018.

[55] X. Quan, z. Wu, x. Dou, m. Hu, and a. Q. Huang, “load current decoupling based lq control for three-phase inverter,” *ieee trans. Power electron.*, vol. 33, no. 6, pp. 5476–5491, 2018.

[56] S. Yang, q. Lei, f. Z. Peng, and z. Qian, “a robust control scheme for grid-connected voltage-source inverters,” *ieee trans. Ind. Electron.*, vol. 58, no. 1, pp. 202–212, 2011.

[57] Mathworks, “robust control toolbox.” 2018.

[58] M. Jr *et al.*, “robust hinf control for grid connected pwm inverters with LCL filters,” *Ind. Appl. (induscon), 2012 10th ieee/ias int. Conf.*, pp. 1–6, 2012.

[59] J. Daafouz and j. Bernussou, “poly-quadratic stability and hinf performance for Discrete systems with time varying uncertainties,” *proc. Ieee int. Conf. Decis. Control*, no. December, pp. 267–272, 2001.

[60] T. S. Lee, k. S. Tzeng, and m. S. Chong, “robust controller design for a single-phase Ups inverter using μ-synthesis,” *ieee proc. - electr. Power appl.*, vol. 151, no. 3, p. 334, 2004.

[61] G. J. Balas, j. C. Doyle, k. Glover, a. Packard, and r. Smith, “computation visualization programming for use with matlab ® μ-analysis and synthesis toolbox user’s guide,” 1984.

[62] N. A. Ashtinai, s. M. Azizi, and s. A. Khajehoddin, “control design in μ-synthesis framework for grid-connected inverters with higher order filters,” *ecce 2016 - ieee energy convers. Congr. Expo. Proc.*, pp. 1–6, 2016.

[63] L. A. Maccari *et al.*, “lmi-based control for grid-connected converters with LCL Filters under uncertain parameters,” *ieee trans. Power electron.*, vol. 29, no. 7, pp. 3776– 3785, jul. 2014.

[64] J. Daafouz and j. Bernussou, “parameter dependent lyapunov functions for discrete time systems with time-varying parametric uncertainties,” *syst. Control lett.*, vol. 43, no. 5, pp. 355–359, 2001.

[65] Y. A. R. I. Mohamed, h. H. Zeineldin, m. M. A. Salama, and r. Seethapathy, “seamless formation and robust control of distributed generation microgrids via direct voltage control and optimized dynamic power sharing,” *ieee trans. Power electron.*, vol. 27, no. 3, pp. 1283–1294, 2012.

[66] Y. Han, p. Shen, x. Zhao, and j. M. Guerrero, “control strategies for islanded microgrid Using enhanced hierarchical control structure with multiple current-loop damping schemes,” *ieee trans. Smart grid*, vol. 8, no. 3, pp. 1139–1153, may 2017.

[67] M. Kabalan and p. Singh, “optimizing a virtual impedance droop controller for parallel inverters,” *ieee power energy soc. Gen. Meet.*, vol. 2015-septe, 2015.

[68] Y. Han, h. Li, p. Shen, e. A. A. Coelho, and j. M. Guerrero, “review of active and reactive power sharing strategies in hierarchical controlled microgrids,” *ieee trans. Power electron.*, vol. 32, no. 3, pp. 2427–2451, 2017.

[69] J. M. Guerrero, l. Hang, and j. Uceda, “control of distributed uninterruptible power supply systems,” *ieee trans. Ind. Electron.*, vol. 55, no. 8, pp. 2845–2859, 2008.

[70] H. Akagi, y. Kanazawa, and a. Nabae, “instantaneous reactive power compensators comprising switching devices without energy storage components,” *ieee trans. Ind. Appl.*, vol. Ia-20, no. 3, pp. 625–630, 1984.

[71] M. N. Marwali, j.-w. Jung, and a. Keyhani, “control of distributed generation Systems— part ii: load sharing control,” *ieee trans. Power electron.*, vol. 19, no. 6, pp. 1551–1561, 2004.

[72] R. Majumder, “some aspects of stability in microgrids,” *ieee trans. Power syst.*, vol. 28, no. 3, pp. 3243–3252, 2013.

[73] F. Andrade, j. Cusido, and l. Romeral, “transient stability analysis of inverter-interfaced distributed generators in a microgrid system,” *proc. 2011 14th eur. Conf. Power electron. Appl.*, no. June 2015, pp. 1–10, 2011.

[74] X. Guo, z. Lu, b. Wang, x. Sun, l. Wang, and ..., “dynamic phasors-based modeling and stability analysis of droop-controlled inverters for microgrid applications.,” *ieee trans. Smart grid*, vol. 5, no. 6, pp. 2980–2987, 2014.

[75] H. J. Avelar, w. A. Parreira, j. B. Vieira, l. C. G. De freitas, and e. A. A. Coelho, “a state equation model of a single-phase grid-connected inverter using a droop control scheme with extra phase shift control action,” *ieee trans. Ind. Electron.*, vol. 59, no. 3, pp. 1527–1537, 2012.

[76] J. M. Guerrero, l. Garciadevicuna, j. Matas, m. Castilla, and j. Miret, “a wireless controller to enhance dynamic performance of parallel inverters in distributed generation systems,” *ieee trans. Power electron.*, vol. 19, no. 5, pp. 1205–1213, sep. 2004.

[77] H. Xin, l. Zhang, z. Wang, d. Gan, and k. P. Wong, “control of island ac microgrids using a fully distributed approach,” *ieee trans. Smart grid*, vol. 6, no. 2, pp. 943–945, 2015.

[78] J. M. Guerrero, l. Garciadevicuna, j. Matas, m. Castilla, and j. Miret, “output impedance
Design of parallel-connected ups inverters with wireless load-sharing control,” *ieee trans. Ind. Electron.*, vol. 52, no. 4, pp. 1126–1135, aug. 2005.

[79] Z. Zeng, h. Yi, h. Zhai, z. Wang, s. Shi, and f. Zhuo, “a new control scheme for harmonic power sharing and pcc voltage harmonics compensation based on controlling the equivalent harmonic impedance of dgs in islanded microgrids,” *2017 19th eur. Conf. Power electron. Appl. Epe 2017 ecce eur.*, vol. 2017-janua, pp. 1–7, 2017.

[80] Q. C. Zhong, “robust droop controller for accurate proportional load sharing among inverters operated in parallel,” *ieee trans. Ind. Electron.*, vol. 60, no. 4, pp. 1281–1290, 2013.

[81] J. Zhang, j. Chen, x. Chen, and c. Gong, “modelling, analysis and design of droop-controlled parallel three phase voltage source inverter using dynamic phasors method,” *Ieee transp. Electrif. Conf. Expo, itec asia-pacific 2014 - conf. Proc.*, pp. 1–6, 2014.

[82] E. A. A. Coelho, p. C. Cortizo, and p. F. D. Garcia, “small-signal stability for parallel-connected inverters in stand-alone ac supply systems,” *ieee trans. Ind. Appl.*, vol. 38, no. 2, pp. 533–542, 2002.

[83] J. Pou, “modulation and control of three-phase pwm converters,” ph.d dissertation, dept. Elect. Eng., univ. Politècnica de catalunya, terrassa, spain, 2002.

[84] D. J. Zahniser and j. F. Brenner, “signals and systems, by a.v. Oppenheim, a.s. Willsky, and i.t. Young. Prentice-hall, englewood cliffs, new jersey, 1983, 796 pages, hardbound, $37.95,” *cytometry*, vol. 6, no. 4, pp. 392–392, jul. 1985.

[85] M. Lu, x. Wang, p. C. Loh, f. Blaabjerg, and t. Dragicevic, “graphical evaluation of Time-delay compensation techniques for digitally controlled converters,” *ieee trans. Power electron.*, vol. 33, no. 3, pp. 2601–2614, 2018.

[86] J. D. Blight, r. Lane dailey, and d. Gangsaas, “practical control law design for aircraft using multivariable techniques,” *int. J. Control*, vol. 59, no. 1, pp. 93–137, 1994.

[87] M. V. Shcherbakov, a. Brebels, n. L. Shcherbakova, a. P. Tyukov, t. A. Janovsky, and V. A. Evich kamaev, “a survey of forecast error measures,” *world appl. Sci. J.*, vol. 24, no. 24, pp. 171–176, 2013.

[88] J. F. Patarroyo-montenegro, m. Castellà, f. Andrade, k. Kampouropoulos, l. Romeral, and j. Vasquez-plaza, “an optimal tracking power sharing controller for inverter-based generators in grid-connected mode,” in *iecon proceedings (industrial electronics conference)*, 2019.

[89] Ieee standard association, *ieee std. 1547-2018. Standard for interconnection and interoperability of distributed energy resources with associated electric power systems interfaces* . 2018.

[90] C. E. Shannon, “communication in the presence of noise,” *proc. Ire*, vol. 37, no. 1, pp. 10–21, jan. 1949.

[91] J. M. Rey, p. Marti, m. Velasco, j. Miret, and m. Castilla, “secondary switched control with no communications for islanded microgrids,” *ieee trans. Ind. Electron.*, vol. 64, no. 11, pp. 8534–8545, 2017.

[92] J. Kukkola, m. Hinkkanen, and k. Zenger, “observer-based state-space current controller for a grid converter equipped with an LCL filter: analytical method for direct discrete-time design,” *ieee trans. Ind. Appl.*, vol. 51, no. 5, pp. 4079–4090, 2015.

[93] J. Kukkola and m. Hinkkanen, “observer-based state-space current control for a three-phase grid-connected converter equipped with an LCL filter,” *ieee trans. Ind. Appl.*, vol. 50, no. 4, pp. 2700–2709, 2014.

[94] J. M. Rey, c. X. Rosero, m. Velasco, p. Marti, j. Miret, and m. Castilla, “local frequency restoration for droop-controlled parallel inverters in islanded microgrids,” *ieee trans. Energy convers.*, vol. 34, no. 3, pp. 1232–1241, 2018.

[95] J. F. Patarroyo-montenegro, j. E. Salazar-duque, s. I. Alzate-drada, j. D. Vasquez-plaza, and f. Andrade, “an ac microgrid testbed for power electronics courses in the University of puerto rico at mayagüez,” in *2018 ieee andescon, andescon 2018 - conference proceedings*, 2018.